THE MODULATION OF ATMOSPHERIC RIVERS BY CIRCULATION REGIMES IN THE ECMWF COUPLED MODEL: FIDELITY AND RESOLUTION DEPENDENCE

by

Mary Korendyke

A Thesis
Submitted to the
Graduate Faculty
of
George Mason University
in Partial Fulfillment of
The Requirements for the Degree
of
Master of Science
Atmospheric, Oceanic and Earth Sciences

Committee:

_____	Dr. David Straus, Thesis Chair
_____	Dr. Jagadish Shukla, Committee Member
_____	Dr. Cristiana Stan, Committee Member
_____	Dr. Mark Uhen, Department Chairperson
_____	Dr. Donna M. Fox, Associate Dean, Office of Student Affairs & Special Programs, College of Science
_____	Dr. Fernando Miralles-Wilhelm, Dean, College of Science
Date: _____	Fall Semester 2021 George Mason University Fairfax, VA

The Modulation of Atmospheric Rivers by Circulation Regimes in the ECMWF Coupled Model: Fidelity and Resolution Dependence

A Thesis submitted in partial fulfillment of the requirements for the degree of Master of Science at George Mason University

by

Mary Korendyke
Bachelor of Science
St. Mary's College of Maryland, 2019

Director: David Straus, Professor
Department of Atmospheric, Oceanic and Earth Sciences

Fall Semester 2021
George Mason University
Fairfax, VA

TABLE OF CONTENTS

LIST OF TABLES

LIST OF FIGURES

ABSTRACT

THE MODULATION OF ATMOSPHERIC RIVERS BY CIRCULATION REGIMES IN THE ECMWF COUPLED MODEL: FIDELITY AND RESOLUTION DEPENDENCE

Mary Korendyke

George Mason University, 2021

Thesis Director: Dr. David Straus

The large scale circulation of the atmosphere, as characterized by circulation regimes, has a significant influence on storminess and precipitation extremes. One type of structure known to be related to precipitation is atmospheric rivers, regions of intense poleward moisture flux. This raises the question of what spatial resolution is required to accurately simulate the circulation dependence of atmospheric rivers. This paper investigates the impact of enhanced resolution on the simulation of circulation regimes over the Pacific North American region during boreal winter, and the regime dependence of atmospheric river patterns. In particular we examine the realism of ensemble forecasts made with the ECMWF model at three different resolutions (100km, 31km, 16km). The regimes are determined from the k-means clustering method; our results focus on two choices for the number of clusters: 4 and 5. We create regime composites of z500 and u250 anomalies, then calculate spatial correlation, differences in regime persistence

distribution, and annual maximum episode persistence to compare reanalysis with model simulations. Composites for regime-associated atmospheric rivers were also computed, and spatial correlations calculated. We find that regimes are better simulated in going from low to medium resolution, but that does not apply in going from the medium to high resolution. `We find that generally regime persistence is well represented, with some exceptions. We also find that atmospheric rivers typically show good spatial correlation with their assigned regimes, and that the correlation is somewhat improved in going from the low to medium resolution despite a consistent undercounting of rivers in the model. Future work is needed to determine if the model loses moisture as the forecast length increases.

INTRODUCTION

Modern forecast models simulate a number of important measures relating to storms on sub-seasonal and intra-seasonal timescales. These include the location and intensities of atmospheric rivers (long narrow bands of intense poleward moisture flux). Since this measure has a dependence on planetary-scale circulation patterns (also called circulation regimes), it follows that this dependence must be accurately captured for this forecast storminess measure to be useful. This raises the question of what spatial resolution is required to accurately simulate the circulation dependence of atmospheric rivers. Existing research has focused on the effect of enhanced resolution on the simulation of either small-scale weather events (Feng et al. 2019), or regimes (Strommen et al. 2019). However, the impact of enhanced resolution on the regime dependence of atmospheric rivers has yet to be investigated.

The importance of model resolution in forecasting and simulations is evident in the literature. Kinter et al. 2013 discuss the results of Project Athena, which was an internationally collaborative response to the recommendations for enhanced model resolution from the World Modeling Summit for Climate Change Prediction in 2008. This recommendation was based on the assertion that increased resolution in models more accurately resolves regional phenomena that are not well represented on coarser grids, thus improving seasonal climate predictions. Regarding this assertion, Project Athena's results indicate that dramatically increased resolution demonstrates a significant impact on how models represent large scale blocking, as in the North Atlantic, among

other important aspects of climate. In the same vein as Athena, Climate Sphinx (Davini et al. 2017) performed a comprehensive set of simulations to investigate the impact of resolution and stochastic physics on climate predictions. This project also demonstrated the importance of enhanced resolution on climate simulations in general, but specifically notes an improvement in the simulation of Euro-Atlantic blocking patterns.

The effects of increasing model resolution on regimes seem to have only been investigated for those in the Euro-Atlantic region. Dawson et al. 2012 uses a global atmospheric model developed by the European Centre for Medium-Range Weather Forecasts (ECMWF) to examine the impact of two different resolutions (high resolution of 16km, as in numerical weather prediction, and the more typical climate model low resolution of 125km) on the climatology of quasi-persistent Euro-Atlantic regimes, which were determined using the k-means clustering method (Straus et al. 2007). They show that the low resolution model is incapable of simulating the statistically significant regimes seen in the reanalysis, while the high resolution model captures the regimes well. Dawson and Palmer 2015 investigate the impact of a stochastic physics scheme on this resolution dependence. For this scheme, the outputs of the parameterizations for unresolved processes include a stochastic component (Berner et al. 2017). Dawson and Palmer find that the simulation of regimes can be significantly improved at all resolutions when applying a stochastic physics scheme. The more recent Strommen et al. 2019 paper builds on these results by examining how robust resolution dependence is across different models (without stochastic parameterization), again for the Euro-Atlantic regimes. Using three models (including that used in the Sphinx project) with low and medium

resolutions, this paper shows that the improvement in regime structure due to enhanced resolution is robust for multiple models with multiple ensembles. While the robustness of the regimes in general and the persistence statistics of the blocking regime in particular are improved with increased resolution, the persistence pattern of the other regimes and the spatial patterns for all regimes were not systematically improved.

Circulation regimes are preferred, persistent planetary scale flow structures defined over large regions, like the extended Pacific North America region or the Euro-Atlantic region. They exist on both inter-seasonal and inter-annual time scales in reanalyses and general circulation models (Straus et al. 2007, Dawson and Palmer 2014, Molteni and Tibaldi 1990). They are preferred in that they occur more often than expected by chance, and persistent in that they have a longer timescale than synoptic events (Straus et al 2017). The frequency of occurrence of weather statistics is influenced by the changes to the planetary scale patterns (Wise et al. 2015) such that patterns of storminess might be directly linked to the circulation regimes, as in Amini and Straus 2019. Through such links, the potential predictability of regimes beyond the 10 day limit might be translated to weather statistics.

Atmospheric rivers have been thoroughly examined in the literature. Ralph et al. 2004 defines atmospheric rivers as long, narrow regions of strong poleward moisture flux associated with polar cold fronts. There is some contention as to the origin of atmospheric rivers. Dacre et al. 2015 state that despite their name and how they are typically discussed in the literature, atmospheric rivers do not get their high water vapor content from the tropics that they then transport to the extratropics, but instead come

from water vapor exported from cyclones as they travel poleward. Still, Ralph et al. 2004 note that atmospheric rivers form a strong link between the weather and planetary scales, in that these rivers influence not only seasonal climate anomalies via cumulative effects, but also short-term weather prediction. They are linked to extreme precipitation events and flooding, especially when they make landfall (DeFlorio et al 2018, Hagos et al. 2015, Ralph et al. 2004). This was seen recently by the extreme atmospheric rivers and related heavy flooding in California in October of this year.

Atmospheric rivers are identified as groups of points with a certain length and breadth, and surpassing threshold variables for column-integrated precipitable water, horizontal wind velocity, and latitude (Amini and Straus 2019, Ralph et al. 2004, Swenson et al. 2018). Other measurements for atmospheric rivers are the integrated vapor transport (Lavers et al 2012, Zhu and Newell 1997) and the peak daily moisture flux, which is a more direct measurement (Payne and Magnusdottir 2014). Amini and Straus 2019 find the total river frequency, and characterize regimes in the Pacific – North American region in ERA-Interim reanalysis (Dee et al., 2011) using the regime specific anomalous frequency of atmospheric rivers. Swenson et al. 2018, using an aquaplanet model at three different resolutions, show that total atmospheric river frequency and characteristic narrowness increases with enhanced resolution.

We used existing forecasts made with the coupled model of the European Centre for Medium-Range Weather Forecasts (ECMWF) at three different resolutions (see Table 1) to examine the planetary wave regimes and corresponding shifts in atmospheric rivers during boreal winter in the Pacific North America (PacNA) region. The corresponding

verification was done using the ERA5 reanalysis (Hersbach et al. 2020). In this paper, we address the following questions using a coupled model with stochastic physics parameterization. How well are the circulation regimes captured by the model? Is this accuracy resolution dependent? How realistic is the modeled climatology of atmospheric rivers, and is this resolution dependent? How realistic is the modeled regime dependence of atmospheric rivers? Is this resolution dependent? In particular, is high resolution needed to accurately capture the changes in storminess between regimes?

Table 1 ECMWF Reforecast Reforecasts for 30 years: 1986 – 2015. Four times daily upper-air and surface data available.

IFS Atmosphere [horizontal resolution]	NEMO Ocean resolution	Start Dates	Forecast Length (months)	Ens. Size
METIS199 [100 km]	1.0° → 1/3° tropics	1 Nov, 1 Dec, 1 Jan, 1 Feb	7,2,2,2	25
METIS639 [31 km]	0.25°	1 Nov, 1 Dec, 1 Jan, 1 Feb	7,2,2,2	25
METIS1279 [16 km]	0.25	1 Nov	2	15

In the Data section, we describe the data sets used, and methodology is described in the Methods section. The section Regimes for 4 Clusters in Results gives a thorough description of the results regarding circulation regimes and their properties,, while the section Atmospheric Rivers in Results details selected atmospheric river results. The results are thoroughly discussed in the Discussion. Finally, conclusions are drawn and future work is detailed in the Conclusion section. The Appendix contains further results for atmospheric rivers.

DATA

Reanalysis Data

ERA5 is the latest reanalysis from the European Centre for Medium-Range Forecasts (Hersbach et al., 2020). It is based on the Integrated Forecasting System (IFS) including observed data assimilation. Its data are hourly estimates of a large number of climate variables relating to the atmosphere, land, and ocean. The native resolution is 30 km, with 137 model levels. We used the final reanalysis product for horizontal winds, geopotential height, and specific humidity at 37 pressure levels on a 0.25^0 grid.

We also utilized the 6-hourly upper air fields of geopotential height and zonal wind from the ERA-Interim reanalysis, (Dee et al., 2011), hereafter ERAI, which is based on an older version of the IFS with native resolution of 80 km with 60 model levels. The reanalysis data we accessed were available on a (512 x 256) (lon x lat) Gaussian grid at 37 pressure levels.

Metis Model Runs

The Metis model is a coupled Earth system model with stochastic parameterizations. It uses the IFS coupled atmosphere-ocean model (cycle 43R1) developed by ECMWF (Vitart et al., 2019), with 6-hourly output of a large number of climate variables for 14 atmospheric levels. The ocean model used is NEMO (Madec et al. 2016), which models the ocean thermodynamics and solves the primitive equations. Metis was run at three different resolutions for a number of different ensembles and

forecast lengths, as indicated in Table 1. The three resolutions are appropriately referred to as Metis199, Metis639, and Metis1279 in this paper.

METHODS

In this section we briefly go over the methods of obtaining circulation regimes and atmospheric rivers.

Circulation Regimes

To investigate the circulation regime dependency on resolution, first we determined the circulation regimes using twice daily 500hPa geopotential height (Z500) and 250hPa zonal wind (U250) data (similar to Amini and Straus 2019) from ERA5 and the Metis reforecasts at three different resolutions (see Table 1). Z500 and U250 data were obtained for the period November through March 1986/87-2015/16 from ERA5 and from ERAI, and from Metis199 and Metis639, November initialization. Metis1279 data were obtained for the November initialization over the November through December period, 1986/87-2015/16. These data were interpolated from the local grids (as described in the Data section) to a 128 x 64 (lat x lon) Gaussian grid, and filtered with a low-pass 10-day filter to retain only periods longer than 10 days. Climatology was calculated by taking a running 5-day mean for each grid point, fitting the time series of each year to a parabola, and then averaging over all years (Straus 1983).

The climatological cycle was removed to create anomalies. A principal component analysis using the combined vector of scaled Z500 and U250 anomalies was carried out on the data associated with the particular time period in question (either November through March, or November through December) with the variates (principal components or PCs) providing the new coordinates. The number of modes (dimension of

the PC-space) was chosen so approximately 2/3 of the total variance was retained. In this case, the number of PCs used is 12. The variance retained for each dataset for the different periods is between 80-82% (see Table 2).

Table 2 Percentage of Variance Explained By the First 12 Principal Components for the Different Time Periods and Datasets

Datasets	November to March	November to December
ERA5	80.89%	81.54%
Metis199	81.38%	80.44%
Metis639	81.71%	81.26%
Metis1279	--------	80.17%

The k-means clustering analysis was then applied in the truncated PC-space to both the ERA5 and ERAI data sets. (The results were essentially identical, as expected.) The k-means method assigns each state uniquely to one of k clusters. The clusters are defined in PC-space, with the average PC coordinates of all states within a cluster defined as a single point termed the "centroid" of that cluster. Compositing any field (such as Z500 or U250) over all states belonging to a cluster yields maps of that field associated with the cluster. We refer to these as cluster maps.

Since the number of clusters (k) is specified a priori in this method, a framework for choosing k is needed. Both significance and reproducibility tests were applied to the ERAI clusters. The significance test measures the likelihood that the degree of clustering in the reduced space is due only to sampling error, as described in detail in Straus et al. (2017), whereas the reproducibility test measures the robustness of the geographical patterns represented by the clusters in half-length samples.

The significance test was conducted for k=2 to k=6 clusters using ERAI data. Global significance of the cluster partitions was found by comparing the variance ratio of the original data with those of 100 synthetic datasets. As seen in Table 3, as k increases, the significance tends to increase.

Table 3 Significance of the Cluster Partitions (k=2-6) for ERAI Data

Cluster Partition	November to March	November to December
2	92.0%	81.0%
3	98.0%	88.0%
4	100.0%	93.0%
5	99.0%	98.0%
6	99.0%	98.0%

The reproducibility of clusters was conducted on ERAI data for k=3 to k=6 clusters (see Figure 1 and Figure 2). 1000 half-length cluster samples were randomly-chosen, and correlated with full sample clusters. For each half-length sample, each cluster map was matched with one of the full sample cluster maps based on pattern correlation. Then, the average of the k-cluster correlations was recorded, one for each half-length sample, to create a probability density function for each cluster partition. In Figure 1, November to March k=3 (black) shows the most consistent matching, but k=3 clusters are less significant than k=4 or k=5 (see separate Table 3). All k>3 pdfs still show the bulk of the correlations above 0.90. In November to December (Figure 2), k=5 (green) shows the highest area for correlations above 0.90.

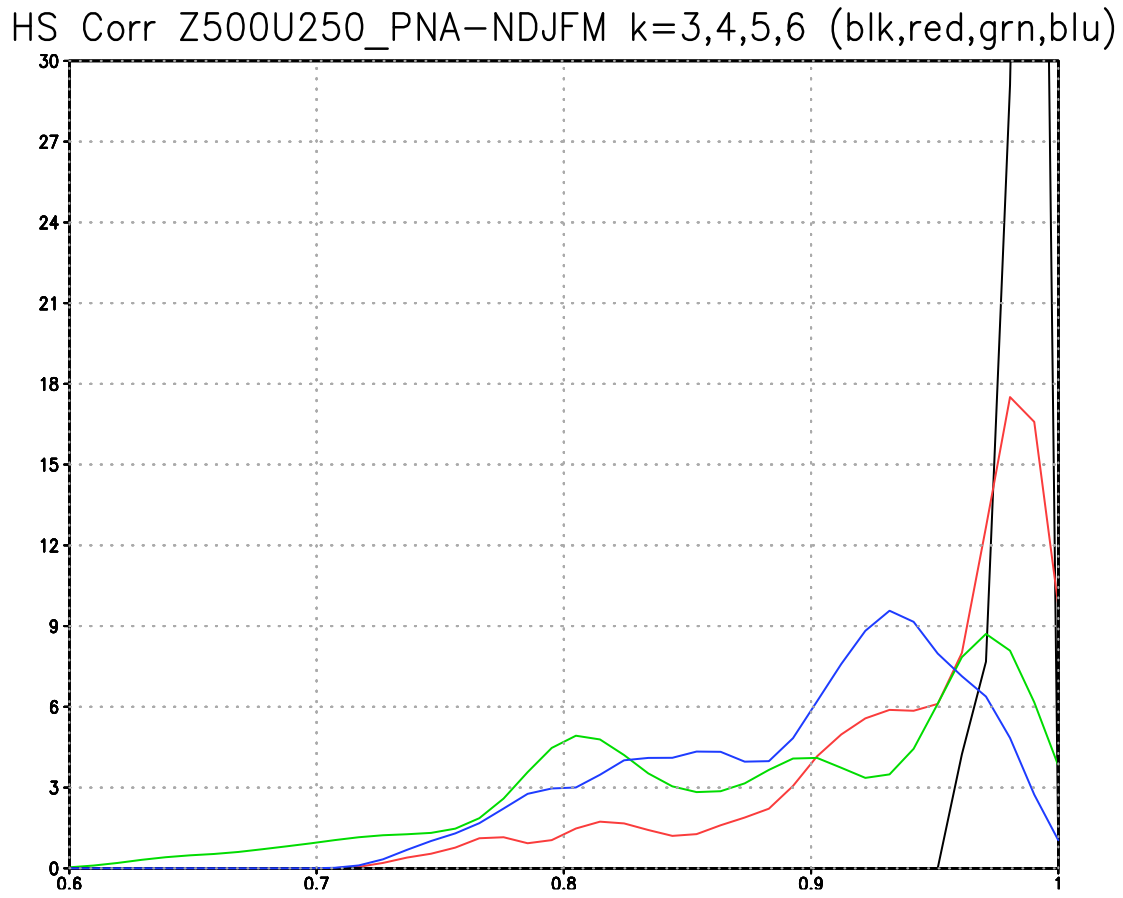

Figure 1 November to March ERAI Half-Length Sample Correlation Pattern for K=3-6 Cluster Partitions. The x-axis is the pattern correlation. The y-axis is relative probability: all pdfs have an area of 1.0.

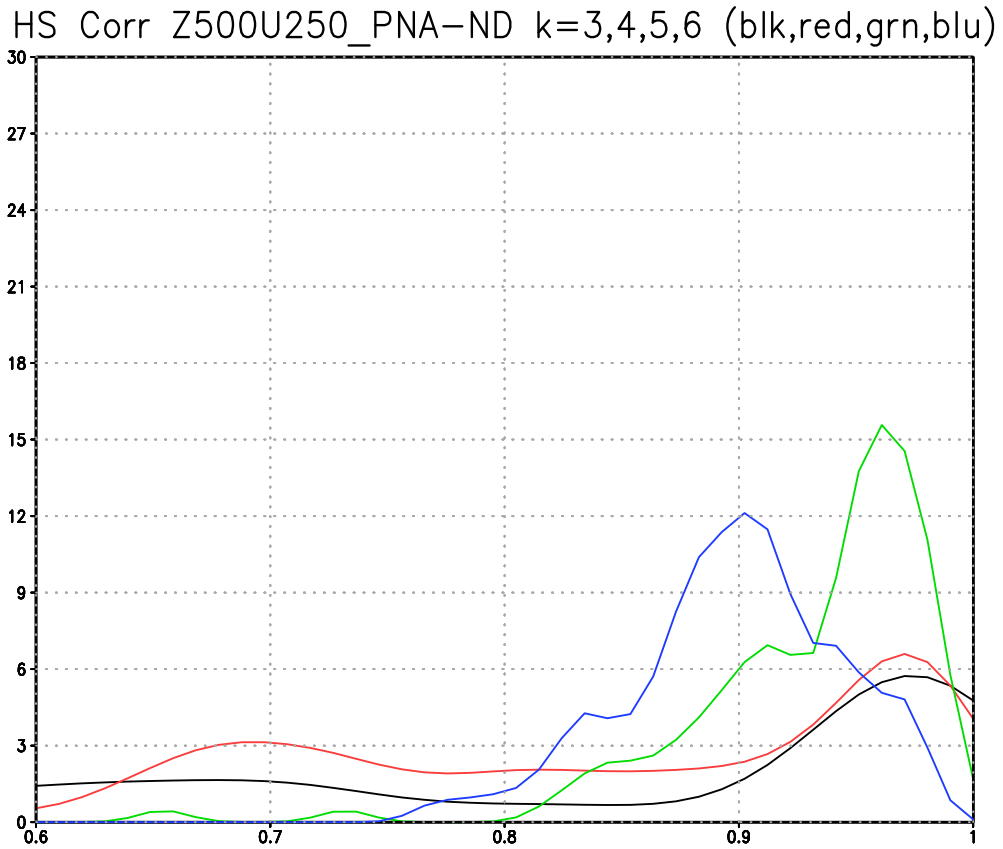

Figure 2 November to December ERAI Half-Length Sample Pattern Correlations for K=3-6 Cluster Partitions. The x-axis is the pattern correlation. The y-axis is relative probability: all pdfs have an area of 1.0.

So, as k increases, significance tends to increase while the reproducibility tends to decrease. Amini and Straus (2019) and Straus et al. (2007) found k=4 or k=5 to be a reasonable choice in the Pacific – North American and Euro-Atlantic regions, respectively. For the clusters obtained here, we also find k=4 and k=5 to be a reasonable compromise between reproducibility and significance vis-a-vis sampling error. For purposes of this work, the most relevant output of the cluster program is a time series of cluster indices, so that each day is characterized by being assigned to a particular cluster.

Atmospheric Rivers

Atmospheric rivers are long, narrow regions of poleward moisture flux. Here we present diagnostic methods for identifying atmospheric rivers. The data is for the same periods described for the circulation regimes (November through March or December, 1986/87-2015/16). These number of atmospheric rivers are composited for each regime. We identified atmospheric rivers using a modified Swenson et al. 2018 method.

This method is based on the method used by Hagos et al. (2015), which builds on the observationally based definition of atmospheric rivers of Ralph et al. 2004: atmospheric rivers are contiguous bands of moisture, with column-integrated precipitable water exceeding 2cm, that are greater than 2000km in length, less than 1000km in width, with a horizontal wind speed greater than 10m/s. In this method, the first step consists of identifying groups of points at which column-integrated precipitable water and horizontal wind speed averaged between 850hPa and 750hPa exceed a given threshold value. However, as the moisture flux is a more direct measurement of water transport, here we identified groups of points at which the magnitudes of column-integrated moisture flux, instead of the column-integrated precipitable water, exceed a given threshold value.

Column-integrated moisture flux has been used in the past to identify atmospheric rivers (Payne and Magnusdottir 2014, Lavers et al. 2012). For the ERA5 reanalysis, the column-integrated moisture flux was calculated from each level's horizontal wind multiplied by the level's specific humidity. We chose the threshold value to be 259kg/ms, the 90^{th} percentile of ERA5 column-integrated moisture flux magnitude values in the PacNA region in November through March, 1986/87-2015/16.

Once the groups of points with moisture flux above the threshold were identified, the moisture flux was then subsequently averaged over each group to check that the net direction of the transport was northward and eastward. Each group was fit to a rectangle to check whether its length and width were within the parameters for a riverine shape (as in Ralph et al 2004). Finally, we excluded any groups with mean latitudes less than 20N, thus focusing on atmospheric rivers associated with extratropical disturbances. (Dacre et al. 2015 suggest that atmospheric rivers are the water vapor footprints of poleward bound cyclones.)

Once atmospheric rivers were diagnosed, the winter climatology of their location and frequency, as well as their regime composites and corresponding anomalies, were calculated. The climatology of atmospheric river occurrences was calculated using the same parabolic method as that used for Z500/U250. Then, the anomalies were calculated to get maps of atmospheric river occurrence anomalies. The time series of cluster indices from computing the regimes was used to assign the maps to each cluster, and the composites generated from those results.

RESULTS

Here we show the results for k=4 clusters. In particular we show composites of the circulation regimes (the regime maps), the spatial correlation patterns of the Metis maps with those from ERA5, the persistence of regime episodes, the significance of difference in episode length, and frequency measurements. We also show composites of atmospheric rivers and related spatial correlations. The results for k=5 clusters, and the Metis composites for k=4, are in the Appendix.

Regimes for 4 Clusters

Composites and Correlations

The Metis maps of Z500 and U250 anomalies associated with the circulation regimes for k=4 clusters are compared to the ERA5 cluster maps in Figure 3 to Figure 7 for the NDJFM time period, and in Figure 9 to Figure 13 for the ND time period. In these maps, Z500 is given by contours, U250 is given by the shading. The frequency of regime occurrence is indicated in the parenthesis in the titles in each case.

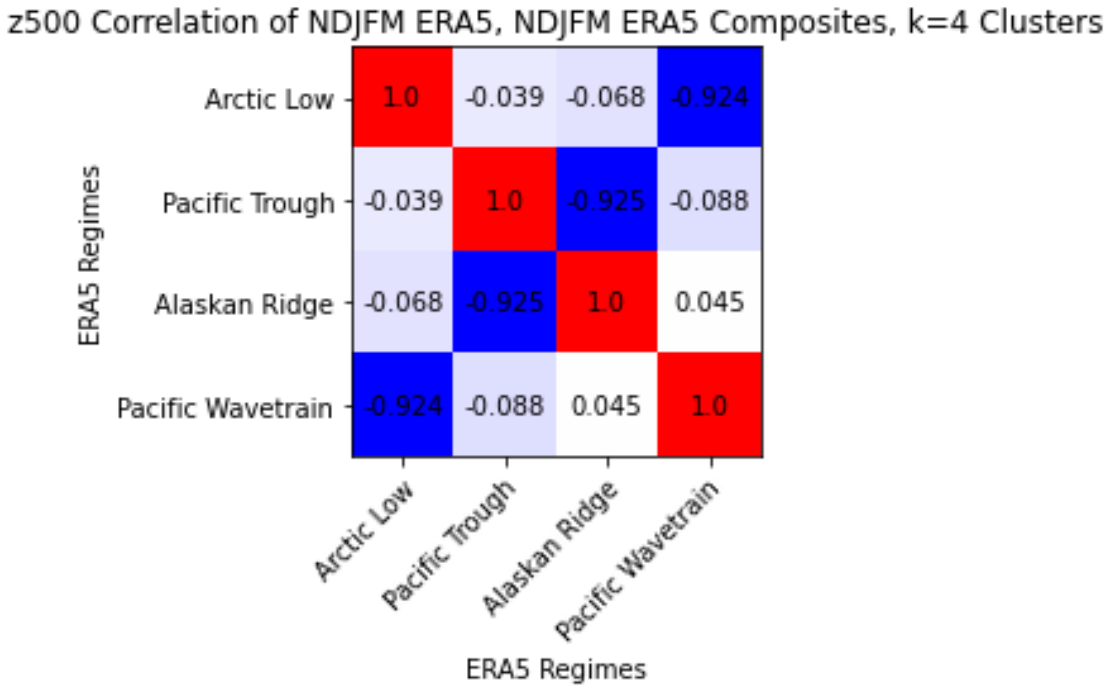

Figure 3 November to March k=4 ERA5 Z500 Composite Autocorrelation. ERA5 Regimes on x and y-axes. Red (blue) indicates strong positive (negative) correlation. White is weak correlation.

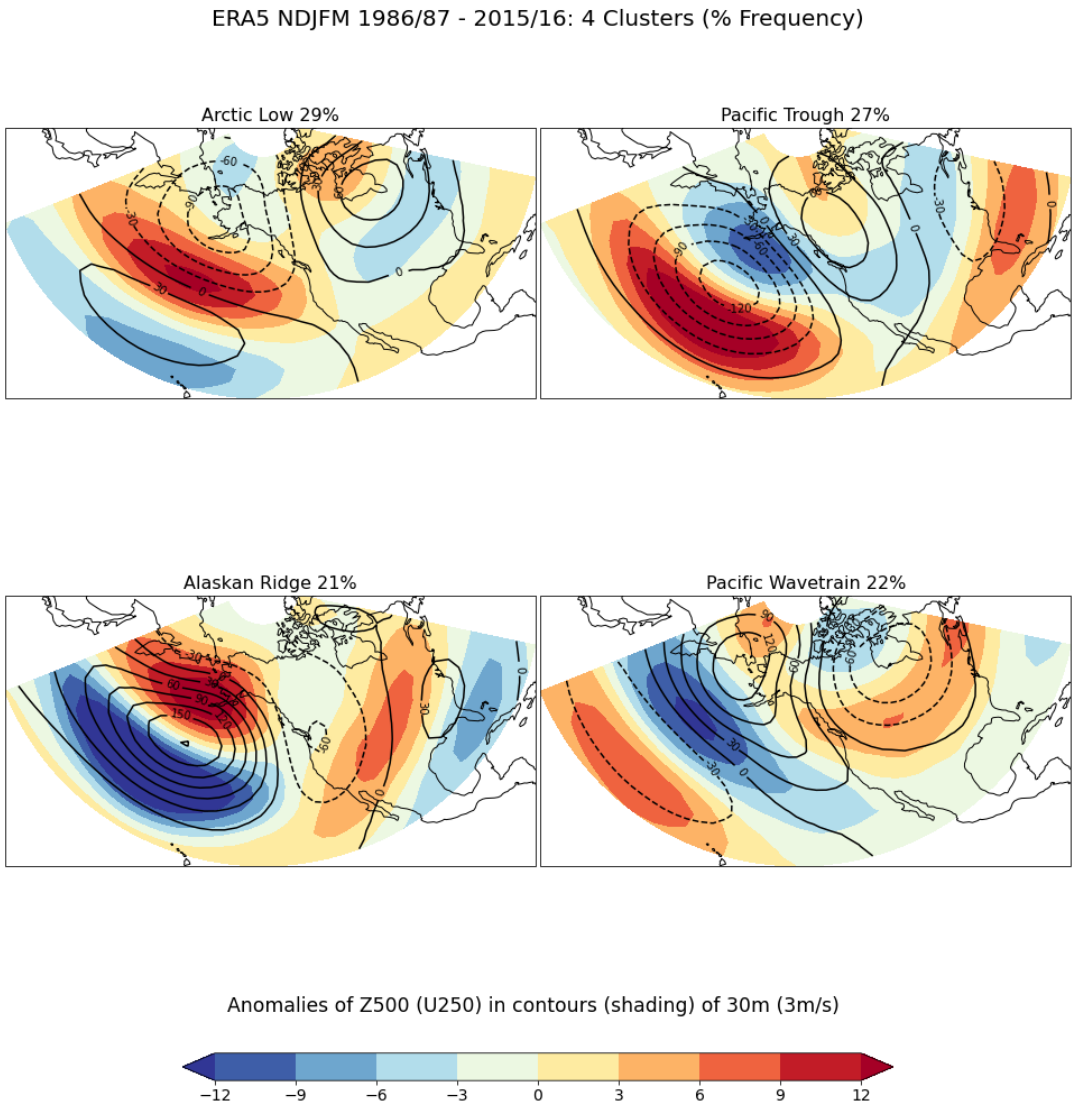

Figure 4 November to March k=4 ERA5 Z500(U250) Cluster Anomaly Composites. Z500 in contours, U250 in shading. Cluster frequency of occurrence given by the percentage. Regime names based on Z500 structures.

The ERA5 cluster maps are identified with a descriptive name by examination and comparison to the cluster maps found in Amini and Straus 2019. They are named in accordance with the large-scale structures in Z500, e.g. Pacific Trough demonstrates a large negative Z500 anomaly over the Pacific. The Metis cluster maps are identified by evaluating the pattern correlation between each Metis cluster and the ERA5 maps. Often

the Metis cluster map has a high pattern correlation (above 0.50) with only one ERA5 map, so that the identification of that Metis map is unambiguous. But this is not always the case, and some Metis cluster maps may have a high correlation with more than one ERA5 cluster, and such maps are considered to be hybrid.

In order to systematically compare one set of cluster maps (such as ERA5) with another (such as a Metis forecast), the pattern correlations are displayed on a grid, where the x-axis refers to the ERA5 clusters, and the y-axis are the clusters to be tested, ordered as displayed left to right, top to bottom in the composites. Positive correlations are shown in red, negative in blue, and very small correlations in white. Z500 and U250 correlations were calculated, and show the same patterns. As such, only Z500 correlations are presented in the body of this paper. The NDJFM Metis comparison grids are in Figure 5. The ND Metis comparison grids are in Figure 10. See Appendix for U250 correlations.

On the grids comparing the ERA5 cluster maps with the Metis cluster maps, the Metis maps are identified both with the title of the best corresponding ERA5 maps and with a number ranging from (0) to (3), which corresponds to the labeling on the y-axis of the correlation grids. The Metis maps are in the Appendix, as the correlation grids demonstrate the most important aspect of these results.

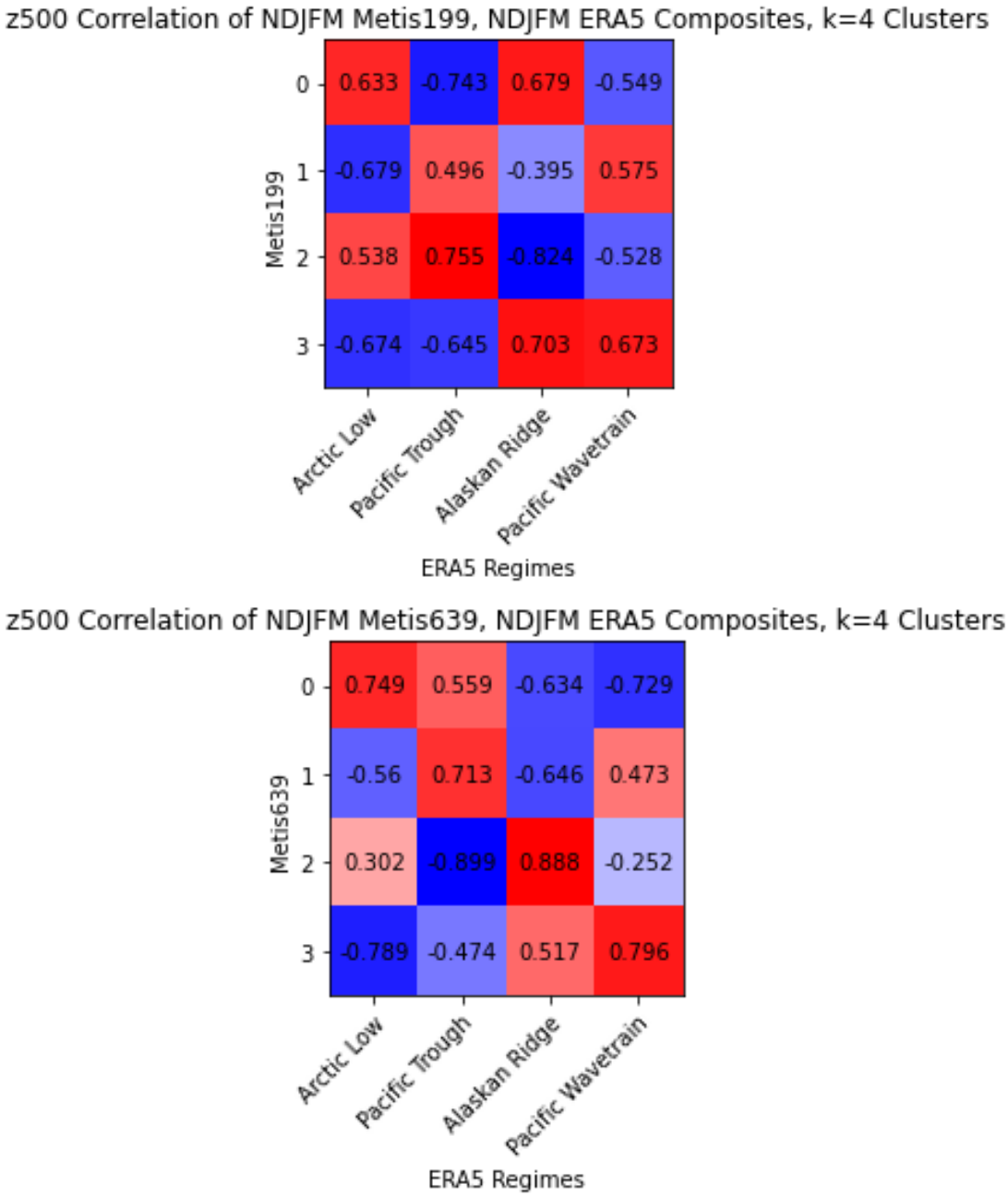

Figure 5 November to March, K=4 Metis Z500 Composite Correlations with ERA5 Regimes. Top to bottom: Metis199, Metis639. ERA5 regimes on x-axes, Metis regimes (unnamed) on y-axes. Strong positive (negative) correlation is red (blue), weak correlation is white. Hybrids: Metis199 0, 2, 3, Metis639 0, 3.

The first correlation grid does not compare ERA5 cluster maps with a Metis forecast, but inter-compares the ERA5 maps for the period NDJFM (see Figure 3). This

grid shows that the ERA5 cluster maps are approximately orthogonal in space, verifying that pattern correlation is a reasonable way to match cluster maps. To examine the impact of enhanced resolution on pattern correlation, we created a visual summary of the correlations in Figure 6 to Figure 7. For each base regime, the two highest correlations with the Metis regimes, and the average of the correlations excluding the maximum, are shown.

Based on the correlation summary, we can see how well the Metis199 and Metis639 match the ERA5 results. Metis199 has maximum correlations all over $\rho=.5$ while Metis639's maximum correlations are all around or greater than $\rho=.75$, indicating that generally Metis639 regimes match ERA5 better. Another measure we look at is the difference between the maximum and 2nd highest correlation, called distinguishability. This measure indicates how distinctive the Metis regimes are when matched with the ERA5 regimes. We see that Metis639 has higher distinguishability for all regimes except the Pacific Trough.

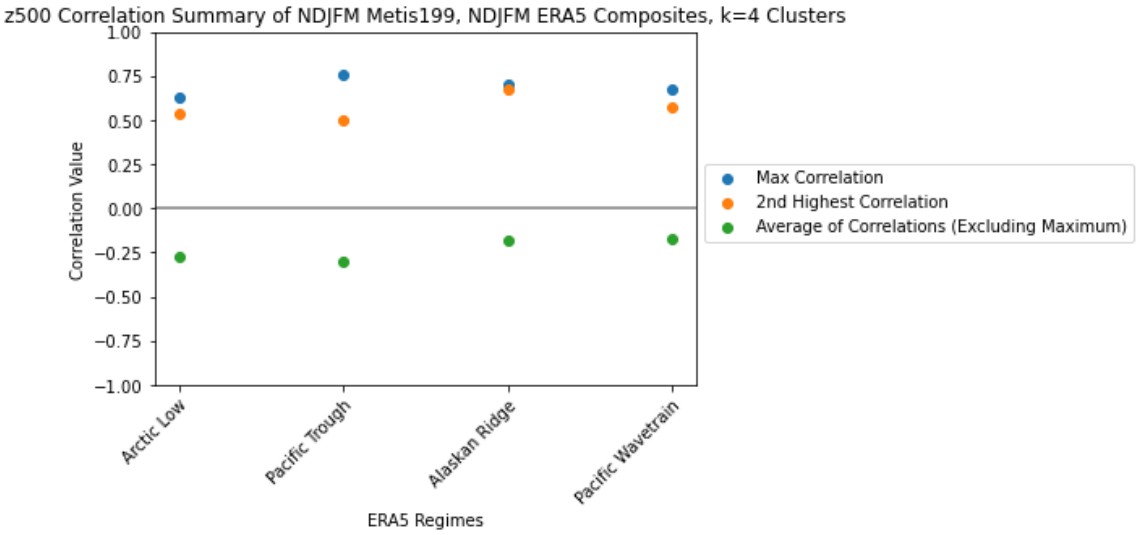

Figure 6 NDJFM 199, ERA5 November to March k=4, 1st and 2nd Composite Correlation Summary

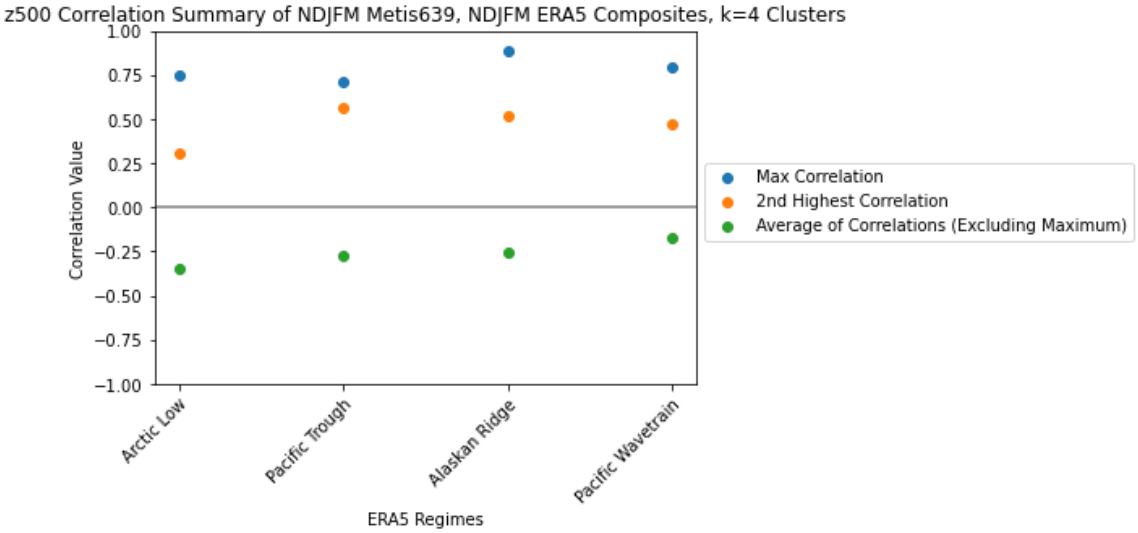

Figure 7 NDJFM 639, ERA5 November to March k=4, 1st and 2nd Composite Correlation Summary

Giving descriptive names to the ERA5 ND cluster maps requires matching the results for this shorter period with the ERA5 results of the longer NDJFM period. This is accomplished with the correlation grid shown in Figure 9 . It's important to note that

while most of the ERA5 ND correlations with ERA5 NDJFM are strong, the descriptive titles in ND don't mean exactly the same patterns as in NDJFM.

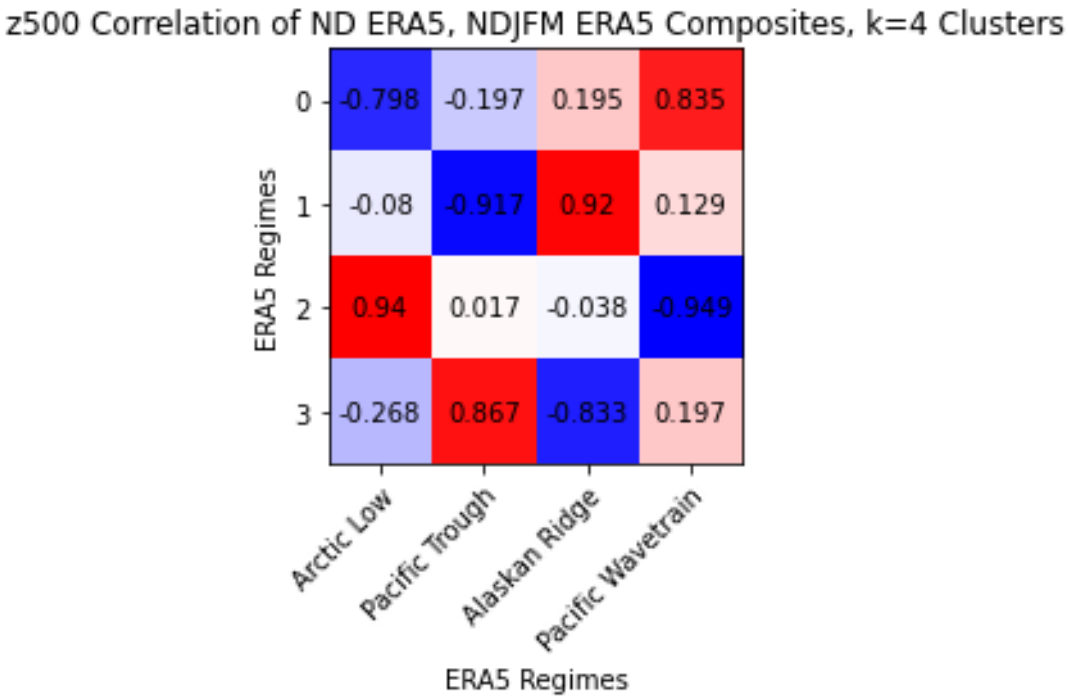

Figure 8 K=4 ERA5 Z500 Composite Correlation Between November to December and November to March periods. ERA5 NDJFM regimes on x-axis. ERA5 ND regimes on y-axis. Red indicates strong positive correlation, blue is strong negative correlation, white is weak correlation.

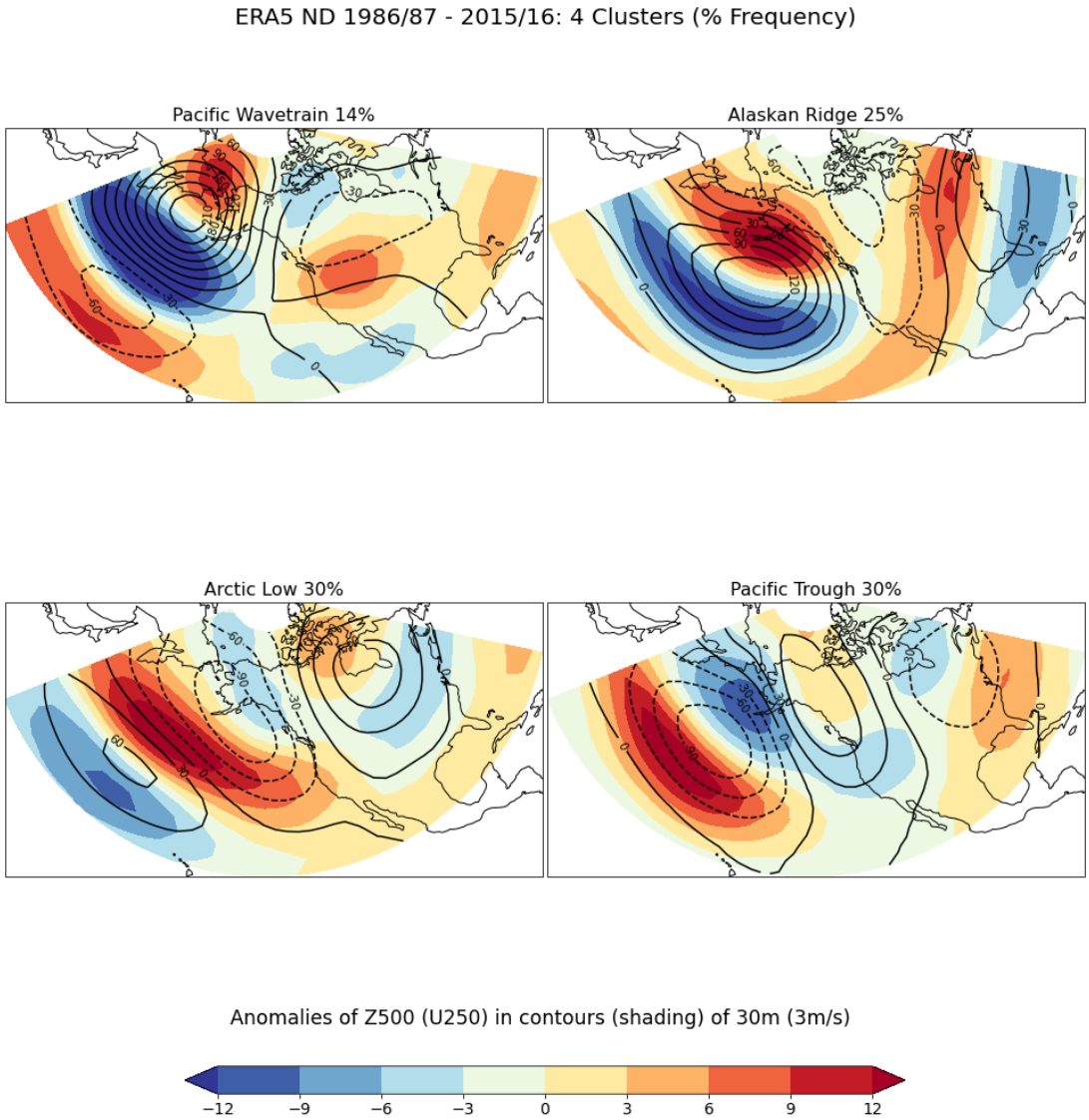

Figure 9 November to December K=4 ERA5 Z500(U250) Cluster Anomaly Composites. Z500 in contours, U250 in shading. Cluster frequency of occurrence given by the percentage. Regime names based on correlation in Z500 structures with NDJFM ERA5 structures.

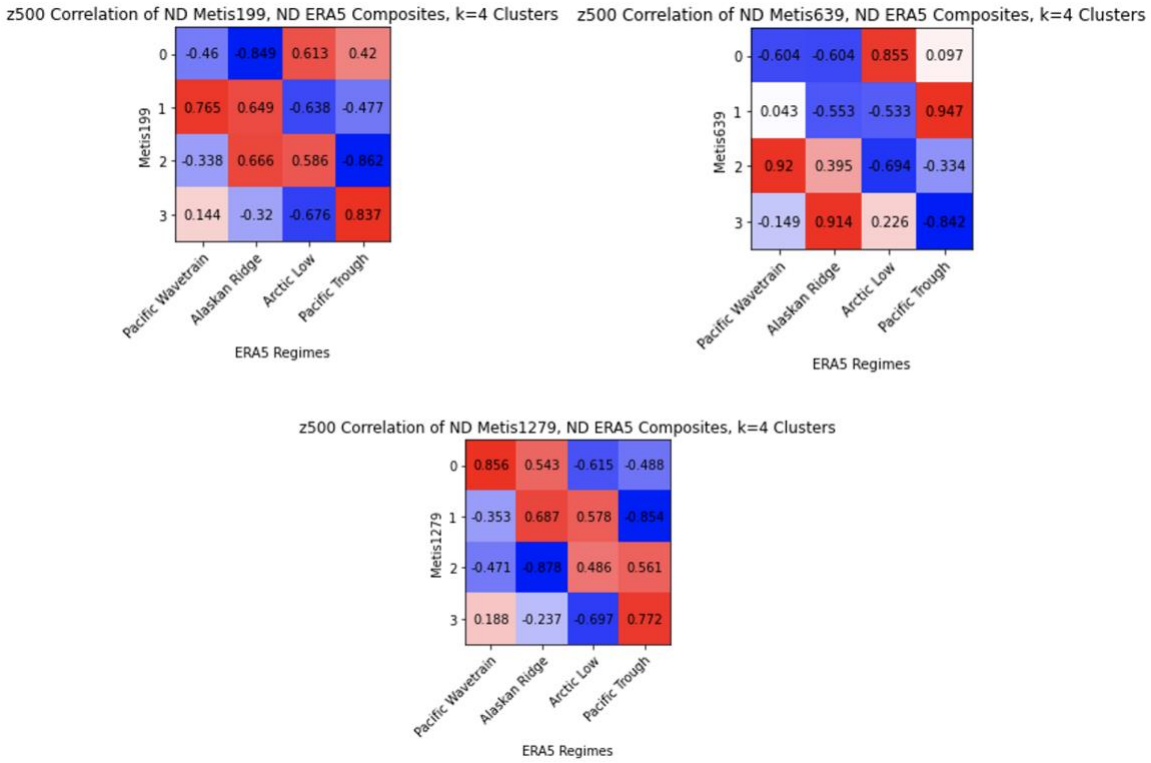

Figure 10 November to December, K=4 Metis Z500 Composite Correlations with ERA5 Regimes. Clockwise, starting in upper left: Metis199, Metis639, and Metis1279. ERA5 regimes on x-axes, Metis regimes (unnamed) on y-axes. Strong positive (negative) correlation is red (blue), weak correlation is white. Hybrids: Metis199 1, 2, Metis1279 0, 1.

We look at the correlation summaries for November to December to see how well Metis resolutions match ERA5 regimes for this period. The maximum correlations for Metis199 and Metis1279 are similar. Metis639 maximum correlation is improved over the other two resolutions. Examining the distinguishability, the difference between the maximum and 2nd highest maximum correlations, we see that Metis199 has good distinguishability for two regimes, but very poor distinguishability for the other two. We see some improvement in distinguishability in Metis1279, but Metis639 demonstrates the best distinguishability for all regimes.

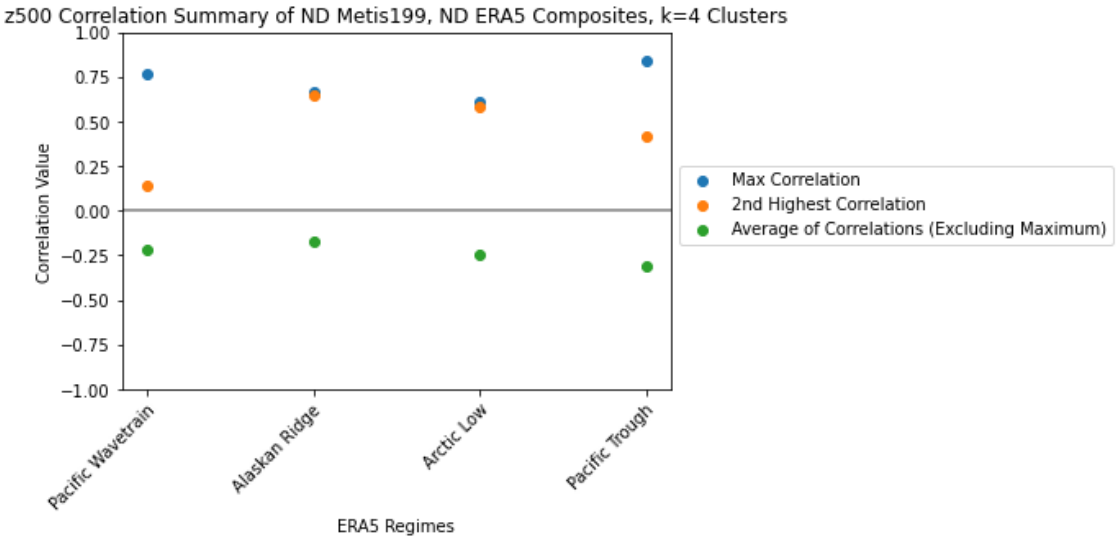

Figure 11 ND 199, ERA5 November to December k=4, 1st and 2nd Composite Correlation Summary

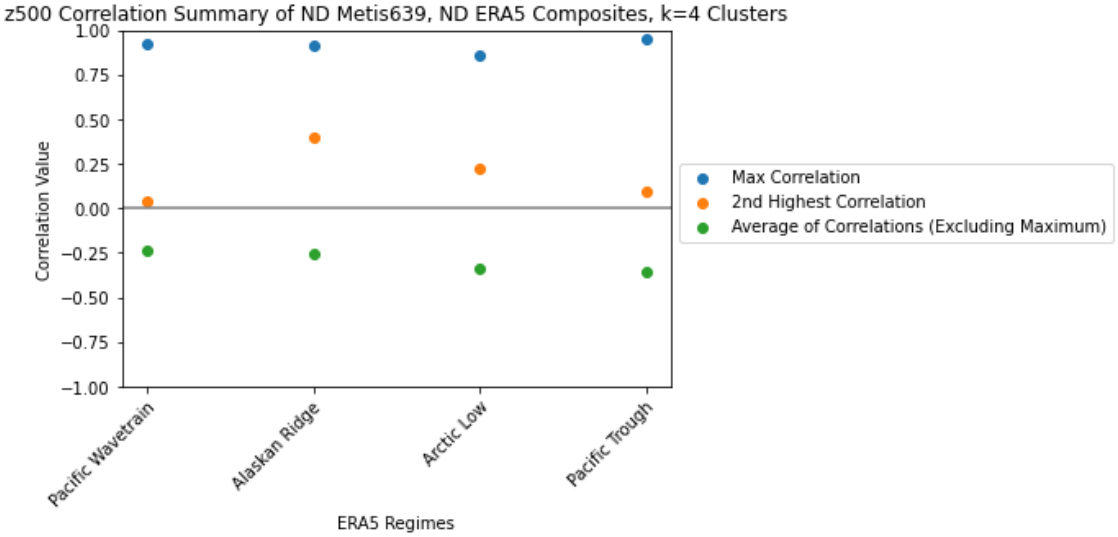

Figure 12 ND 639, ERA5 November to December k=4, 1st and 2nd Composite Correlation Summary

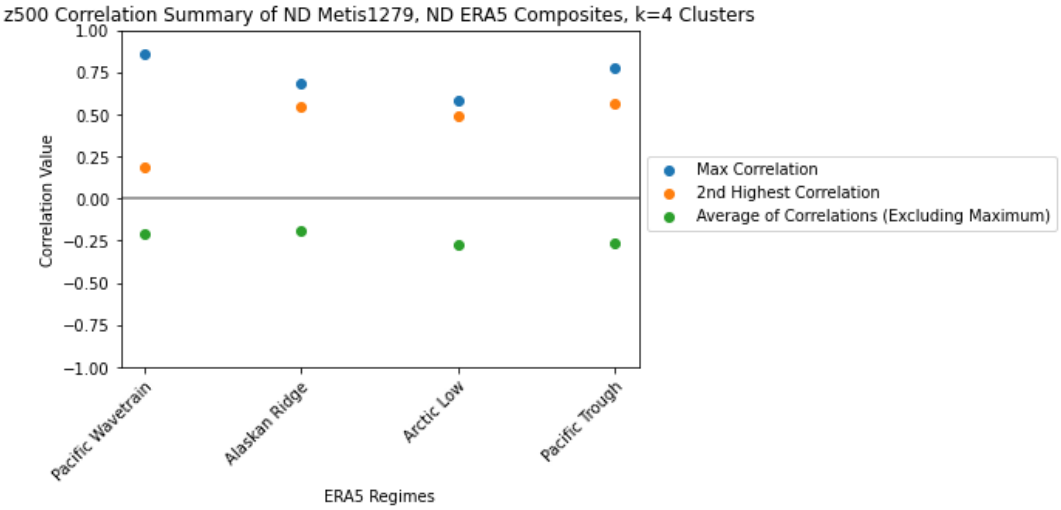

Figure 13 ND 1279, ERA5 November to December k=4, 1st and 2nd Composite Correlation Summary

Cluster Persistence

The atmosphere (or model) can reside in a given cluster over a consecutive number of times. Here, we call each such occurrence an episode. The length of an episode is a mark of its persistence. The more persistent a cluster is, the longer are its episodes. To identify episodes, we take the time series of cluster indices, and identify cluster runs. The length of an episode is the number of times within a run.

This section shows the pdf of episode length for each cluster in a series of histograms for the two time periods (November-March, November-December) for ERA5 (the Metis histograms are in the Appendix). The x-axis is the length of the episode in 12-h periods. The y-axis is the percentage of times that, when the cluster occurs, the episode has a given length.

The two time periods have different values on the axes. November to March has episode lengths of 0-200 (in units of 12 hours) on the x-axis, and 0-6.0% intra-cluster

occurrence percentage on the y-axis. November to December has episode lengths of 0-100 (again in units of 12 hours) on the x-axis, and 0-20.0% intra-cluster occurrence percentage on the y-axis. The Alaskan Ridge and the Arctic Low have a steadily decaying weighting, with the most weighting from 0-15 days (0-30 units), and trailing off after that point. The Pacific Trough and the Pacific Wavetrain have an almost bi-modal structure, with the heaviest weighting from 0-12.5 days (0-25 units), and a weak minimum followed by a weak secondary maximum after 12.5 days (25 units) at about 15 days (30 units).

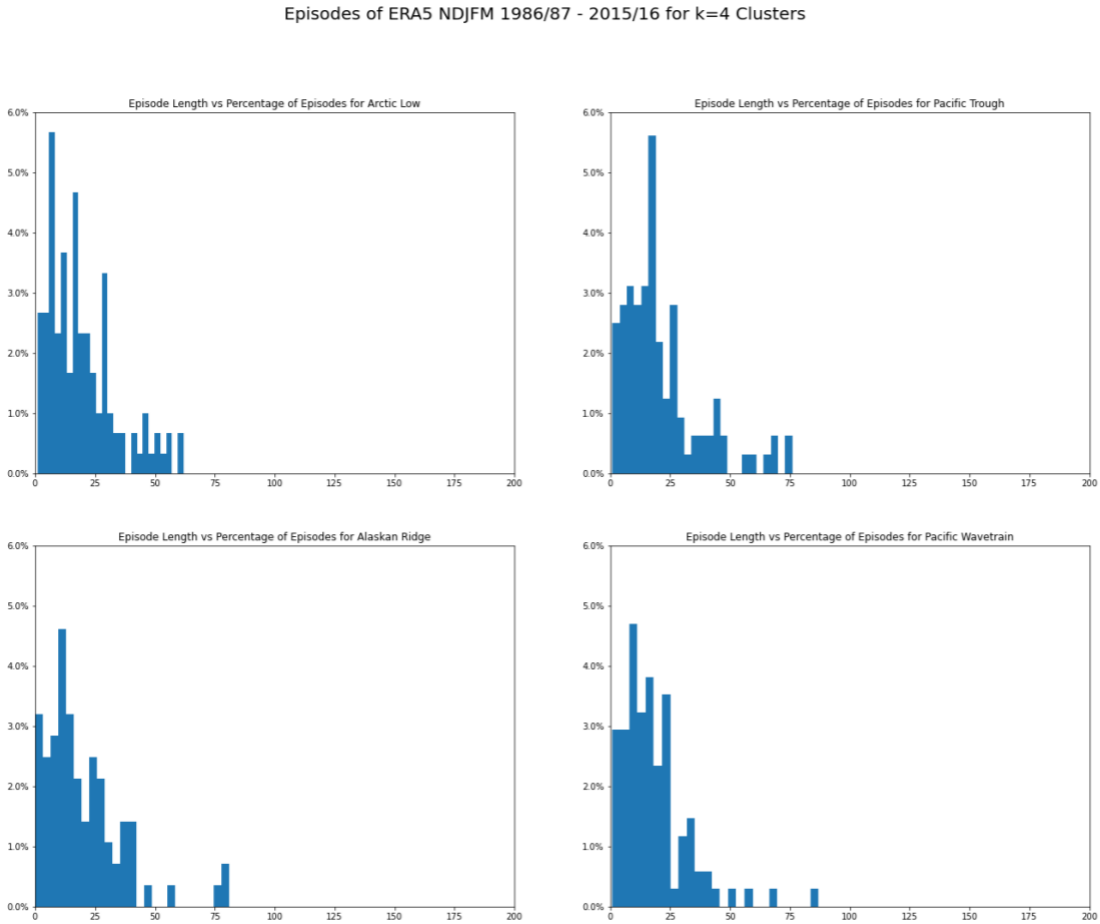

Figure 14 November to March K=4 ERA5 Cluster Persistence Histograms. Length of episode (12 hours) on x-axes, intracluster frequency of episode length occurrence on y-axes. Left to right, top to bottom: Arctic Low, Pacific Trough, Alaskan Ridge, Pacific Wavetrain

The Kolmogorov-Smirnov (K-S) test was used to test for significant differences between the persistence data for ERA5 and the Metis experiments. This is a useful test for pdfs, as it is sensitive to the location and shape of the sample's empirical distributions. The output is a statistic that quantifies the distance between the empirical distribution functions. We test with the null hypothesis that the two distributions are the same. We used the K-S test in the scipy.stats package in Python, which also outputs the p-value associated with the K-S statistic. If the $p <= \alpha$ (level of significance), then we

reject the null hypothesis that the two distributions are the same. Thus small values of p are associated with significant differences between the Metis and ERA5 persistence histograms. For November to March, the K-S p-values were calculated between the ERA5 clusters and the Metis regimes best correlated with them. The Metis PacWav/PacTrough regime is significantly different from the Pacific Trough and Pacific Wavetrain ERA5 regimes in this period. These two ERA5 regimes demonstrate a bi-modality that is not reflected by the model.

Table 4 November to March, K=4, Kolmogorov-Smirnov P-Values For Null Hypothesis of Same Distribution for ERA5 and Metis Cluster Persistence for Metis199 and Metis639. Null Rejected If P-Value <= Level of Significance.

ERA5 regimes	Tco199 NDJFM p-values	Tco639 NDJFM p-values
Arctic Low	AlRidge/ArcLow: .143 PacTrough/ArcLow: .973	ArcLow/PacTrough: .976
Pacific Trough	PacWav/PacTrough: 0.0 PacTrough/ArcLow: .832	ArcLow/PacTrough: .564 PacTrough/PacWav: .001
Alaskan Ridge	AlRidge/ArcLow: .462 AlRidge/PacWav: .629	AlRidge: .667 PacWav/AlRidge: .118
Pacific Wavetrain	PacWav/PacTrough: .066 AlRidge/PacWav: .835	PacTrough/PacWav: .086 PacWav/AlRidge: .48

The November to December period shows more even weighting distributions than the November to March period. The exception is the Pacific Wavetrain, which is most heavily weighted towards very small episode occurrences. The Pacific Trough shows the most regular decaying weighting. The Alaskan Ridge decreasing trend is less pronounced, and the Arctic Low is almost flat from 0-15 days (0-30 units). The Alaskan

Ridge is significantly different from the Metis PacWav/AlRidge regime in the Metis199, Metis1279 resolutions. This is due to the modelled regime overestimating the number of short episodes that occur in the regime.

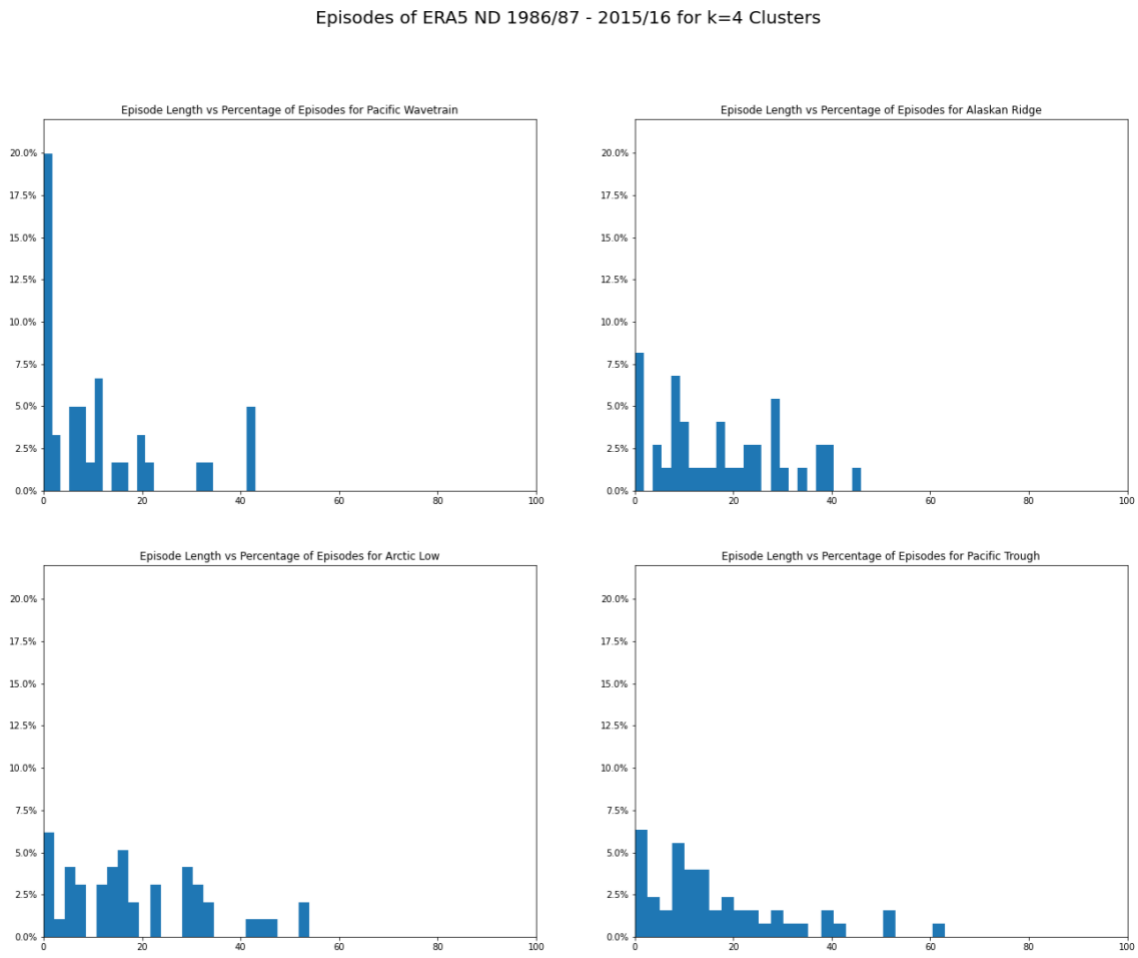

Figure 15 November to December K=4 ERA5 Cluster Persistence Histograms. Length of episode (12 hours) on x-axes, intracluster frequency of episode length occurrence on y-axes. Left to right, top to bottom: Pacific Wavetrain, Alaskan Ridge, Arctic Low, Pacific Trough

Table 5 November to December, K=4, Kolmogorov-Smirnov P-Values For Null Hypothesis of Same Distribution for ERA5 and Metis Cluster Persistence for Metis199, Metis639, and Metis1279. Null Rejected If P-Value <= Level of Significance.

ERA5 regimes	Tco199 ND p-values	Tco639 ND p-values	Tco1279 ND p-values
Pacific Wavetrain	PacWav/AlRidge: .857	PacWav: .992	PacWav/AlRidge: .81
Alaskan Ridge	PacWav/AlRidge: .024 AlRidge/ArcLow: .303	AlRidge: .31	PacWav/AlRidge: .028 AlRidge/ArcLow: .435
Arctic Low	ArcLow/PacTrough: .231 AlRidge/ArcLow: .136	ArcLow: .176	AlRidge/ArcLow: .257 PacTrough/ArcLow: .304
Pacific Trough	ArcLow/PacTrough: .981 PacTrough: .625	PacTrough: .831	PacTrough/ArcLow: .983 PacTrough: .214

Annual Cluster Persistence Maximums

This section shows the annual maximum persistence demonstrated by each cluster. The tables in Figure 16 and Figure 17 have the same color scheme, but different color scales. They are colored according to the other values found within the respective dataset, so that the largest and smallest maximum persistence of each dataset can be compared visually. The smallest maximum is a bright blue, the largest is a bright purple, and the values in the middle are darker shades on a gradient between blue and purple. The years (indicating the start of the winter time period) are on the x-axis, and the regimes are on the y-axis. The regime order changes between the datasets, but is consistent with the order identified in the composite correlation grids (Figure 5, Figure 10).

One interesting pattern is that the Pacific Trough tends to exhibit large maximum episode lengths during El Nino years (i.e. 1991, 1997, 2002, 2009, and 2015) for the extended winter period. In the results for the shortened winter period (November to December), we see that the model tends to have excessively long episodes.

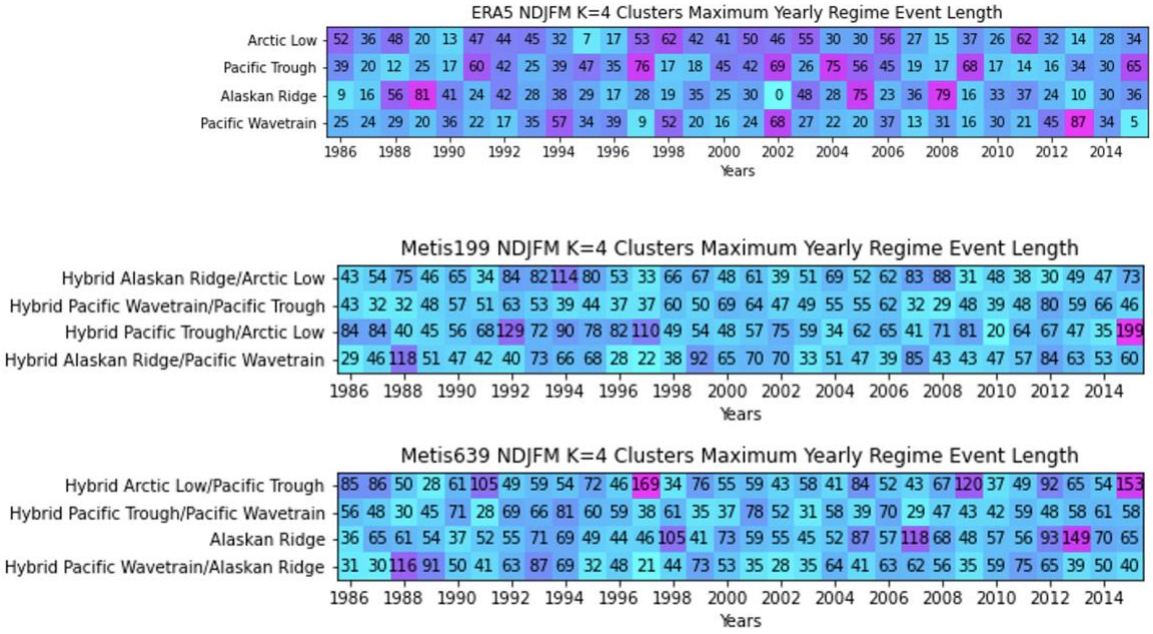

Figure 16 November to March K=4 Yearly Maximum Episode Length Per Regime. Top to bottom: ERA5, Metis199, Metis639. X-axes: years corresponding to November. Y-axes: ERA5 base regimes (for ERA5) or regimes based on correlation with ERA5 base regimes (for Metis). This figure displays the longest length of 12-h periods a regime exhibited for each year. Each dataset has its own color gradient from bright blue (lowest maximum value in the dataset) to bright purple (greatest maximum value in the dataset), with darker colors lying between, so that inter-dataset comparisons of the extremes can be made by visual inspection (e.g. 2002 Alaskan Ridge for ERA5 and Metis199 both demonstrate relatively low maximum persistence values).

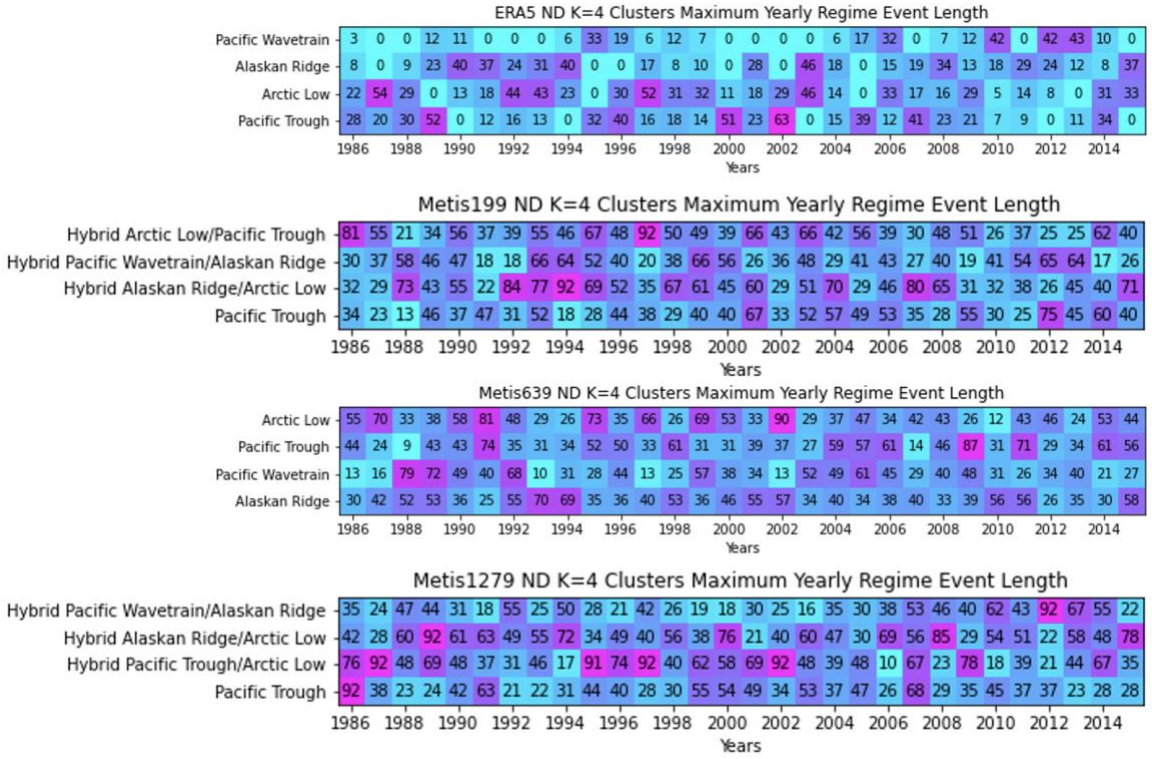

Figure 17 November to December K=4 Yearly Maximum Episode Length Per Regime. Top to bottom: ERA5, Metis199, Metis639, Metis1279. X-axes: years corresponding to November. Y-axes: ERA5 base regimes (for ERA5) or regimes based on correlation with ERA5 base regimes (for Metis). This figure displays the longest length of 12-h periods a regime exhibited for each year. Each dataset has its own color gradient from bright blue (lowest maximum value in the dataset) to bright purple (greatest maximum value in the dataset), with darker colors lying between, so that inter-dataset comparisons of the extremes can be made by visual inspection (e.g. 2002 Alaskan Ridge for ERA5 and Metis199 both demonstrate relatively low maximum persistence values).

Atmospheric Rivers

This section gives the results for two different representations of the atmospheric rivers. The first is the total river occurrence (independent of regime), where we show the composite for all atmospheric river occurrences over all times and ensembles, shown by shading. The second representation (shown for k=4 regimes only) has regime composites for the atmospheric river total occurrences in contours, and anomalies in occurrence from the climatology in shading.

Total River Occurrence

The atmospheric rivers were identified. Then, the number of times they occurred at each grid point were summed up to get the total number of river occurrences. The Metis results show the total (and ensemble average) of the number of occurrences over the whole period. The total number was divided by the number of ensembles used (25 for November to March, 15 for November to December) to scale by ensemble. The composites show the total (ERA5) or total ensemble-scaled (Metis) number of atmospheric river occurrences in shading, where dark blue indicates 0-20 occurrences, and bright yellow indicates more than 160 occurrences over all years.

There is a systematic undercounting of the atmospheric rivers in the model. The November to March rivers are underestimated by about a third, while the November to December model shows about half of the rivers counted in the reanalysis. This undercounting is consistent across all resolutions. While the rivers are undercounted, the spatial patterns of the maxima and minima of river occurrence is well reflected by the model. Specifically, the west Pacific, southeast US, and the Atlantic demonstrate local maxima in the reanalysis and in the model regardless of resolution.

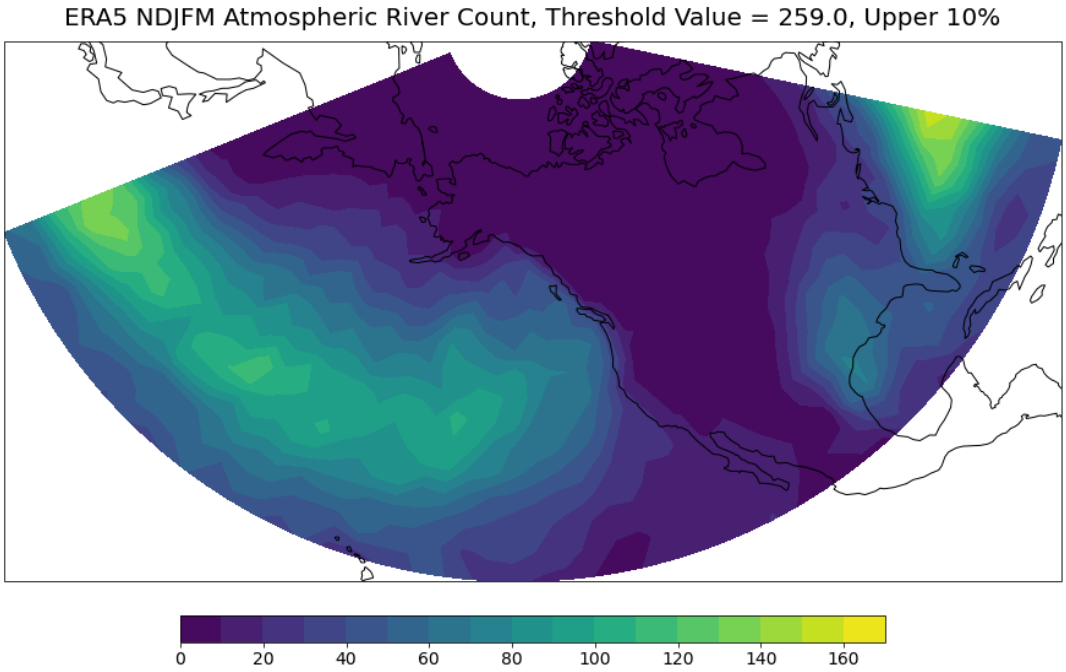

Figure 18 November to March ERA5 Total Atmospheric River Counts Over All Years for Moisture Flux Magnitude > 259.0kg/ms. The scale is 0-170 total occurrences.

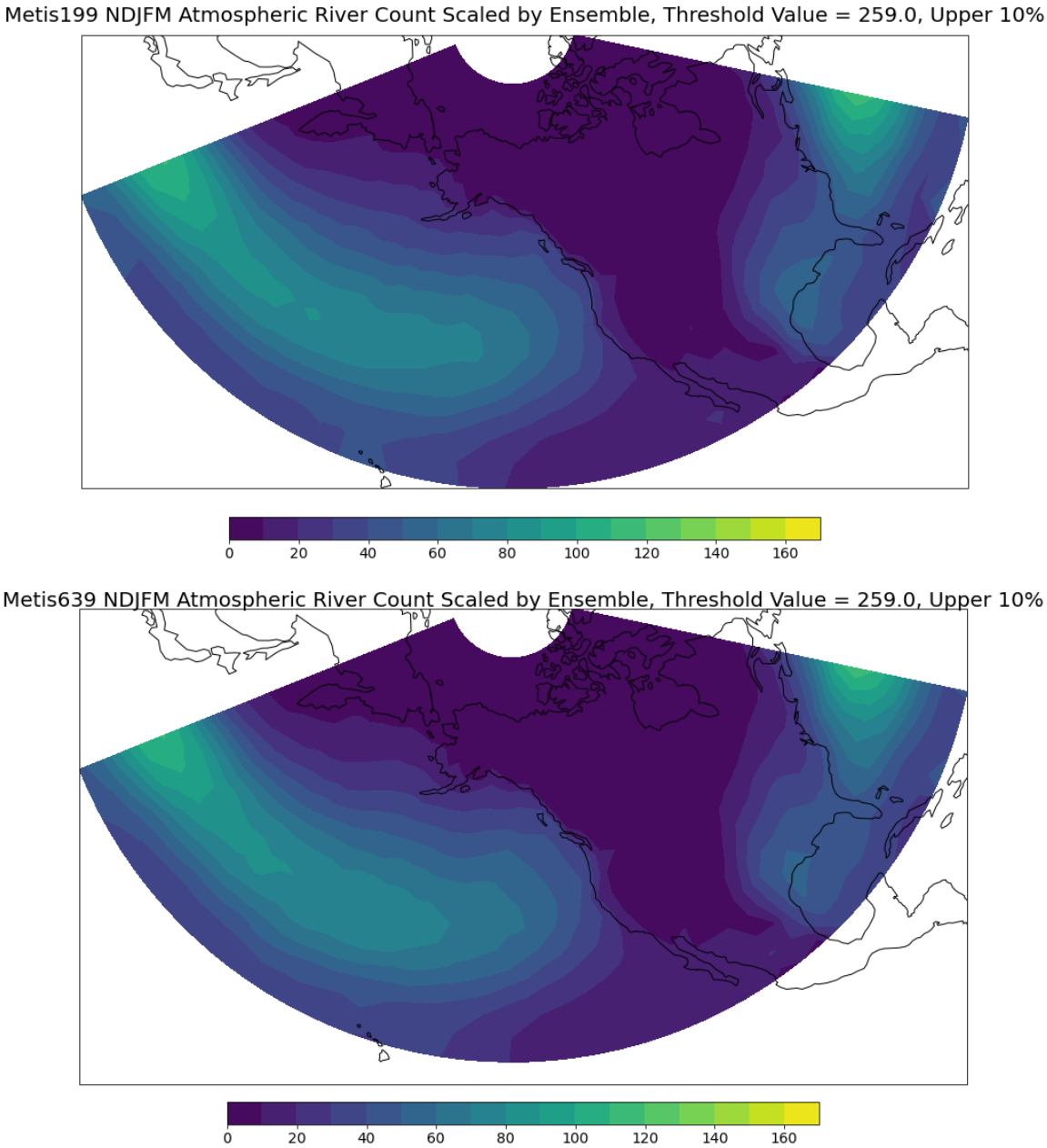

Figure 19 November to March Metis199 (top), Metis639 (bottom) Ensemble-Averaged Total Atmospheric River Counts Over All Years for Moisture Flux Magnitude > 259.0kg/ms. Note that the same scale (0-170 total occurrences) is used for the ERA5 total counts. While the locations of relative high/low atmospheric river frequency are consistent between ERA5 and Metis, Metis magnitude is off by a factor of about 2.

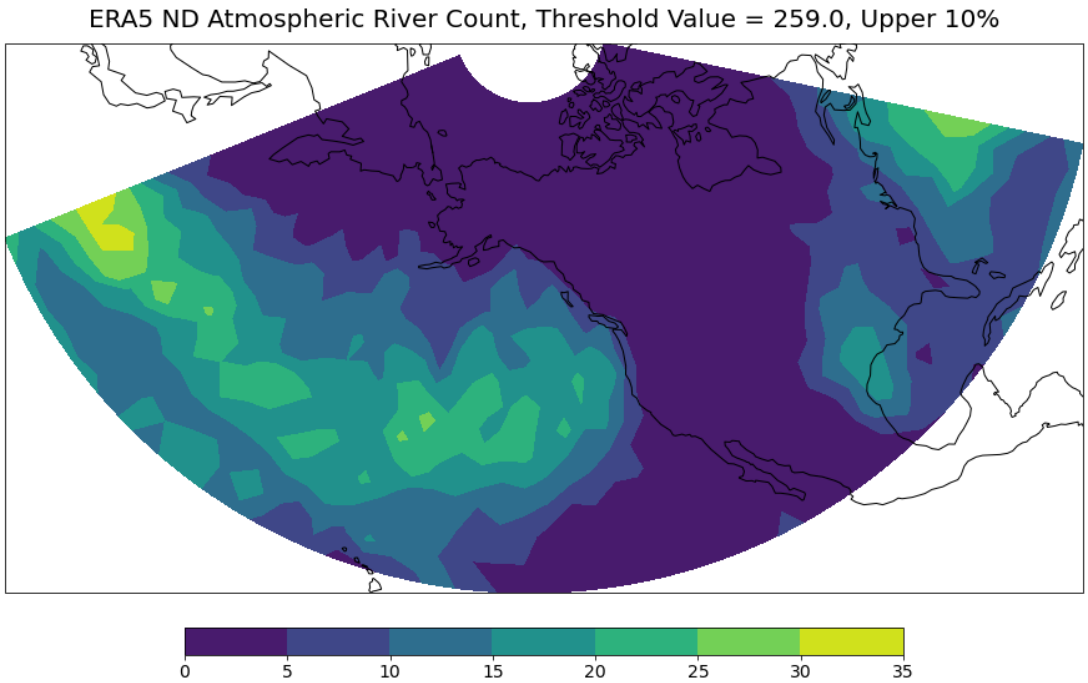

Figure 20 November to December ERA5 Total Atmospheric River Counts Over All Years for Moisture Flux Magnitude > 259.0kg/ms. The scale is 0-35 total occurrences.

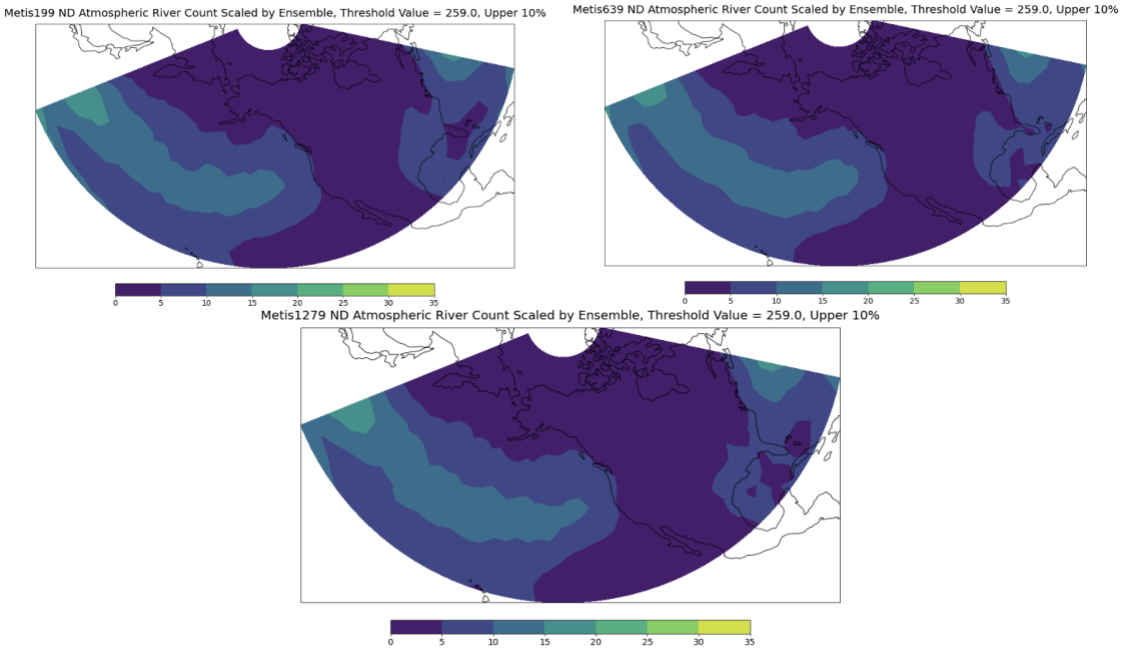

Figure 21 November to December Metis Ensemble-Averaged Total Atmospheric River Counts Over All Years for Moisture Flux Magnitude > 259.0kg/ms. Clockwise, starting in upper left: Metis199, Metis639, Metis1279. Note that the same scale (0-35 total occurrences) is used for the ERA5 total counts. While the locations of

relative high/low atmospheric river frequency are consistent between ERA5 and Metis, Metis magnitude is off by a factor of about 2.

Regime Composites for K=4

We calculated the climatology of the number of atmospheric rivers using the same parabolic method we used for the climatology of Z500 and U250. From this climatology, we calculated the anomalies of the number of atmospheric rivers at each time. Using the time series of cluster indices from calculating the regimes, we identified the atmospheric river maps associated with each cluster. This section shows the composites of those results (Figure 22, Figure 28). The contours (shading) display the total (anomalous) number of intra-cluster atmospheric river occurrences. Blue shading indicates a decrease in atmospheric rivers relative to climatology, while red shading indicates an increase. The November to March atmospheric river regime anomalies (Figure 22) are modulated by the Z500 and U250 regime patterns (Figure 4). One direct relation is that over the Pacific, the Arctic Low, Pacific Trough, and Alaskan Ridge atmospheric river anomaly patterns reflect the U250 anomalies directly: large westerly wind anomalies are associated with increased atmospheric rivers.

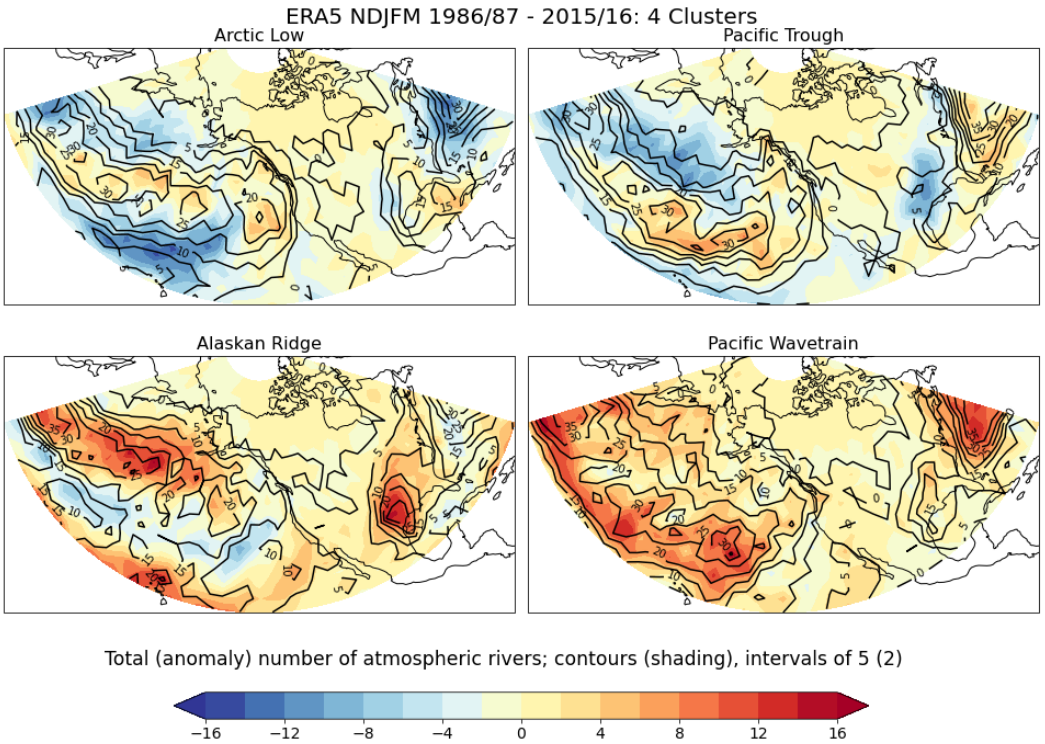

Figure 22 November to March K=4 ERA5 Atmospheric River Regime Composites. Total (anomalous) atmospheric river counts per regime given by contour (shading). Regimes named based on Z500/U250 composites. Positive (negative) anomalies shown in red (blue) shading.

The overall correlation is calculated between the atmospheric river anomaly patterns of the ERA5 and Metis regimes. As for the Z500 anomaly correlations, red (blue) indicates positive (negative) correlation, while intensity of the shade indicates strength of the correlation. The Metis atmospheric river regime composites are named using the best correlated ERA5 regimes from these calculations. The hybrid regimes' atmospheric river anomalies are largely correlated with the appropriate ERA5 regime, as seen in the Hybrid PacTrough/ArcLow of Metis199 and Metis639 in the November to March period (Figure 23), though the maximum correlations are weaker than for the Z500 correlations.

While the ERA5 Z500 regimes are largely consistent between the November to March period and the November to December period (as seen in Figure 26), only the Arctic Low and Pacific Wavetrain atmospheric river anomalies are correlated above 50%. However, the November to December ERA5 regime-dependent river anomalies display a similar distinctiveness as the Z500 regimes, seen in the strong diagonal correlation pattern comparing ND ERA5 regimes with themselves (Figure 27). The model correlations for the ND period (Figure 29) show correlations between hybrid regimes and base regimes, as for the NDJFM period. Again, atmospheric river correlations between the model and the reanalysis are less than the Z500 correlations.

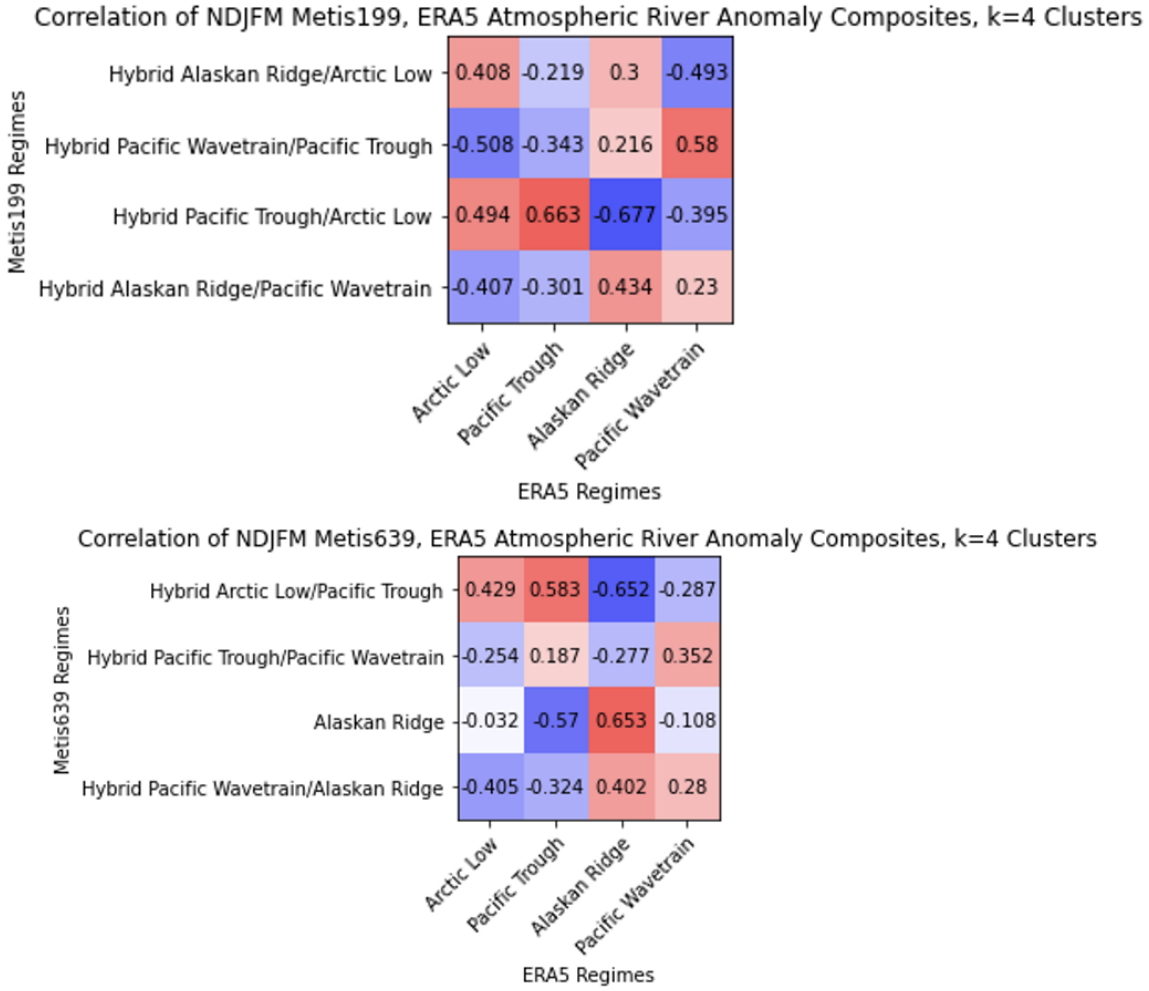

Figure 23 November to March, K=5 Metis Atmospheric River Anomaly Composite Correlations with ERA5 Regimes. Right to left: Metis199, Metis639. ERA5 regimes on x-axes, Metis regimes (named for z500 correlations with base regimes) on y-axes. Strong positive (negative) correlation is red (blue), weak correlation is white.

Again, we include a correlation summary between the atmospheric river anomaly regimes of the model and the reanalysis. Distinguishability is defined as the difference between the first and second maximum correlations. For November to March, the Metis199 results show good distinguishability for two regimes, while Metis639 shows good distinguishability for three. In the November to December period, Metis199 shows

poor distinguishability for one regime, Metis1279 shows poor distinguishability for two, but Metis639 shows a reasonable distinguishability.

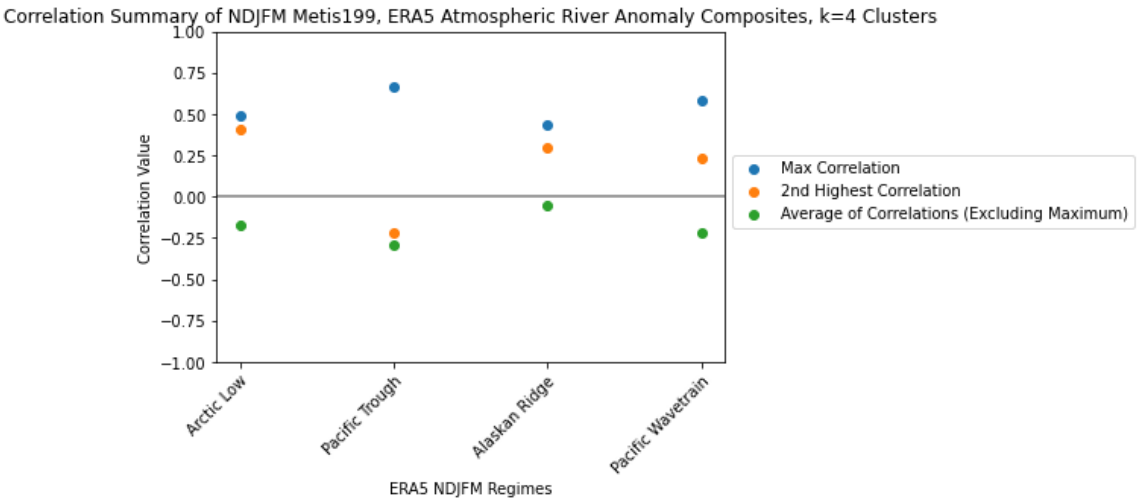

Figure 24 NDJFM 199, ERA5 November to March k=4, 1st and 2nd Atmospheric River Composite Correlation Summary

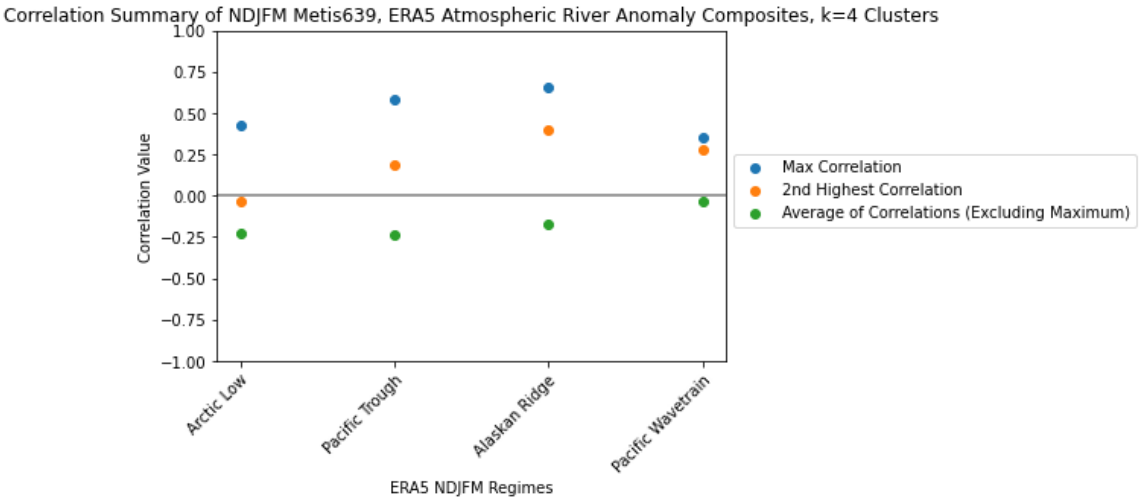

Figure 25 NDJFM 639, ERA5 November to March k=4, 1st and 2nd Atmospheric River Composite Correlation Summary

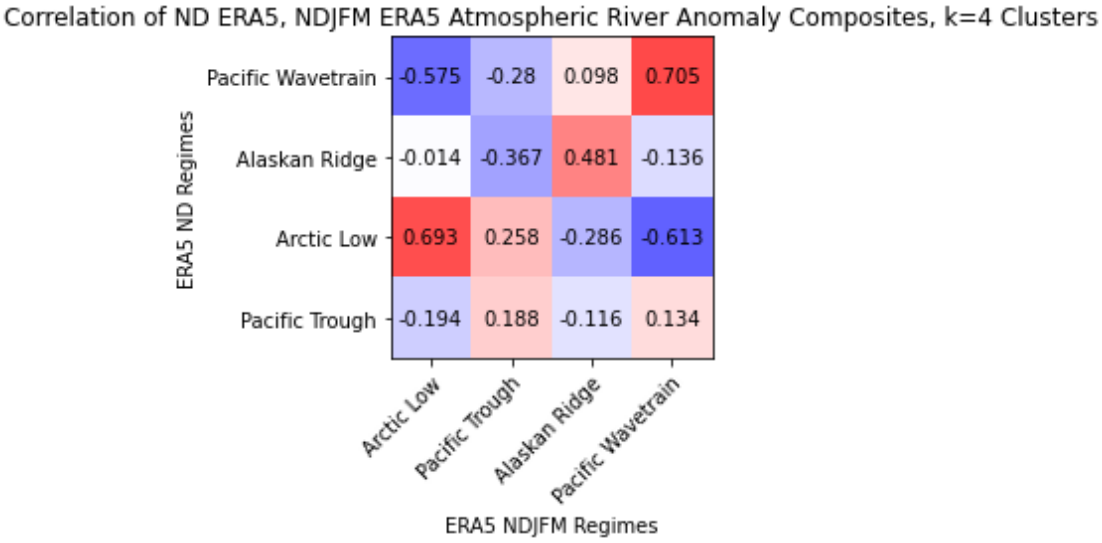

Figure 26 November to March k=4 November to March, November to December ERA5 Atmospheric River Anomaly Composite Correlation. ERA5 November to March regimes on x-axis. ERA5 November to December regimes on y-axis. Red (blue) indicates strong positive (negative) correlation. White is weak correlation.

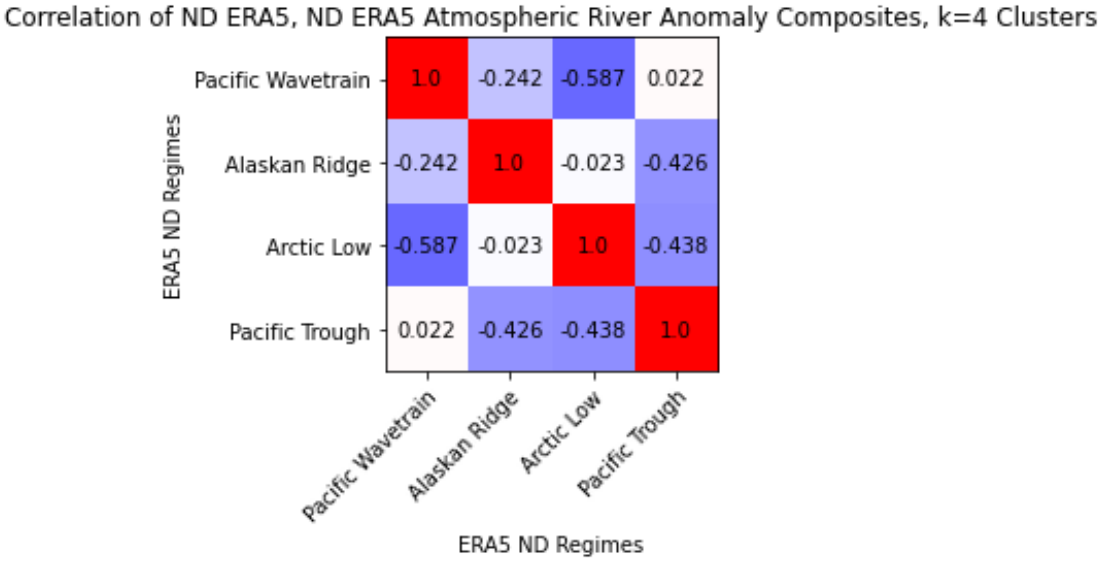

Figure 27 November to December k=5 ERA5 Atmospheric River Anomaly Composite Autocorrelation. ERA5 Regimes on x and y-axes. Red (blue) indicates strong positive (negative) correlation. White is weak correlation.

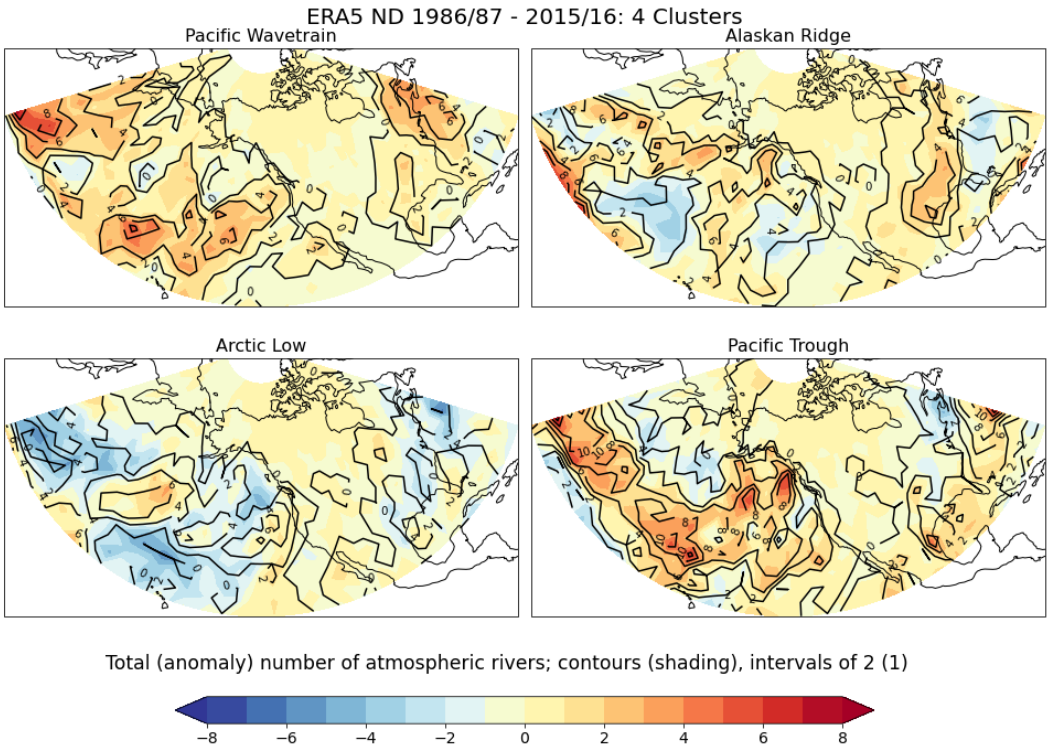

Figure 28 November to December K=4 ERA5 Atmospheric River Regime Composites. Total (anomalous) atmospheric river counts per regime given by contour (shading). Regimes named based on Z500/U250 composites. Positive (negative) anomalies shown in red (blue) shading.

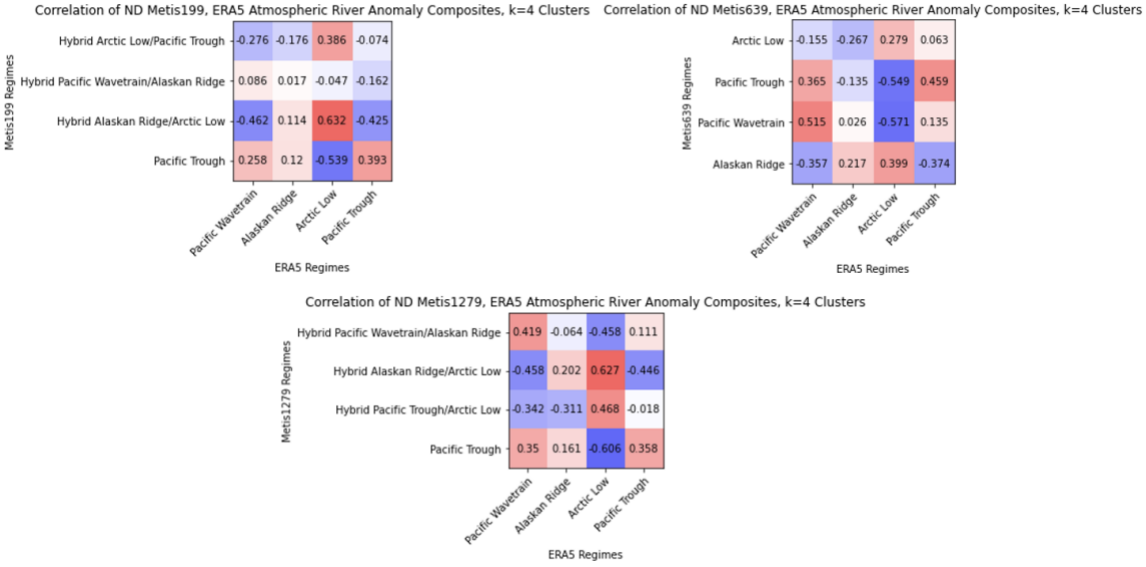

Figure 29 November to December, K=4 Metis Atmospheric River Anomaly Composite Correlations with ERA5 Regimes. Right to left: Metis199, Metis639. ERA5 regimes on x-axes, Metis regimes (named for z500

correlations with base regimes) on y-axes. Strong positive (negative) correlation is red (blue), weak correlation is white.

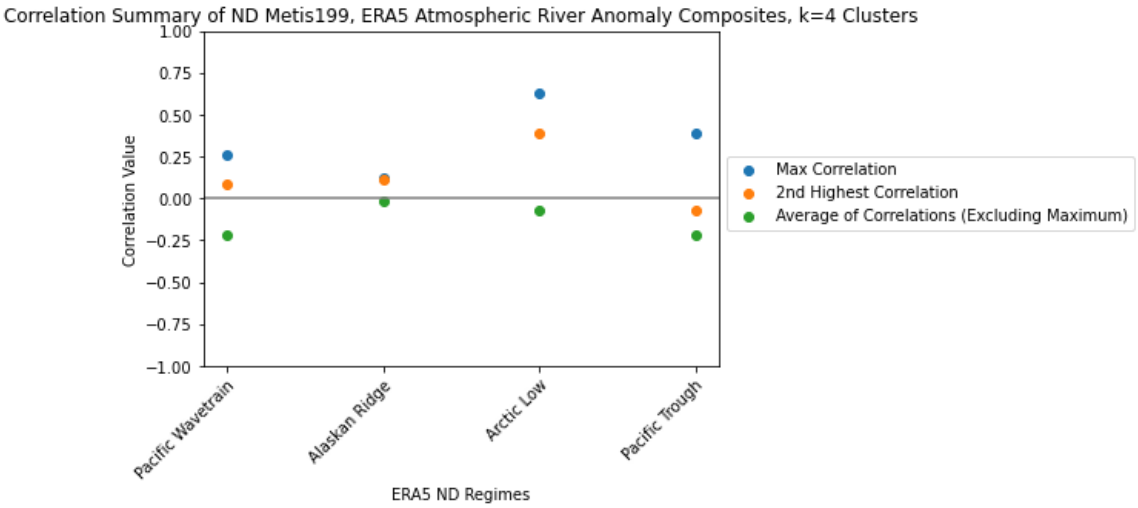

Figure 30 ND 199, ERA5 November to December k=4, 1st and 2nd Atmospheric River Composite Correlation Summary

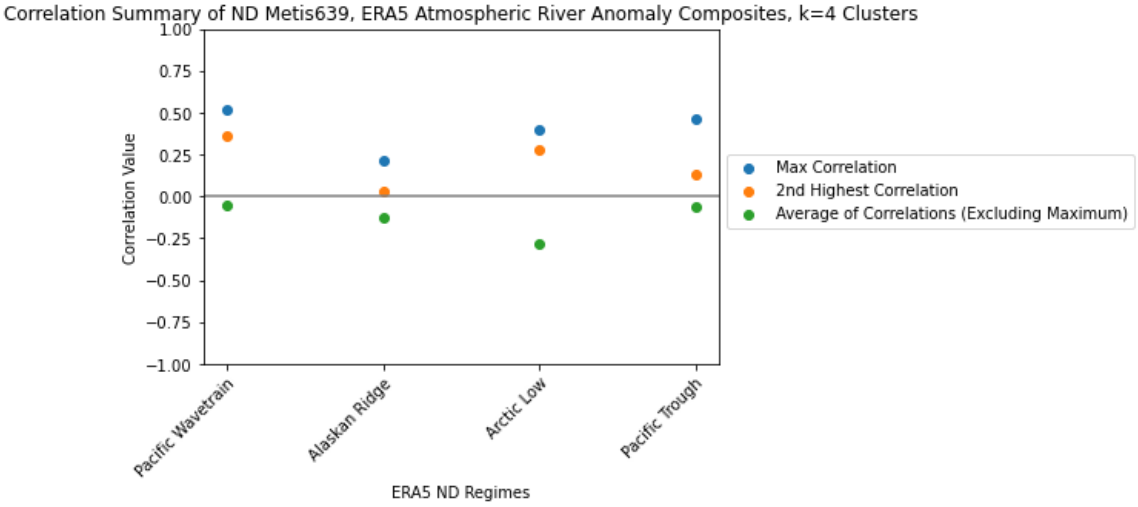

Figure 31 ND 639, ERA5 November to December k=4, 1st and 2nd Atmospheric River Composite Correlation Summary

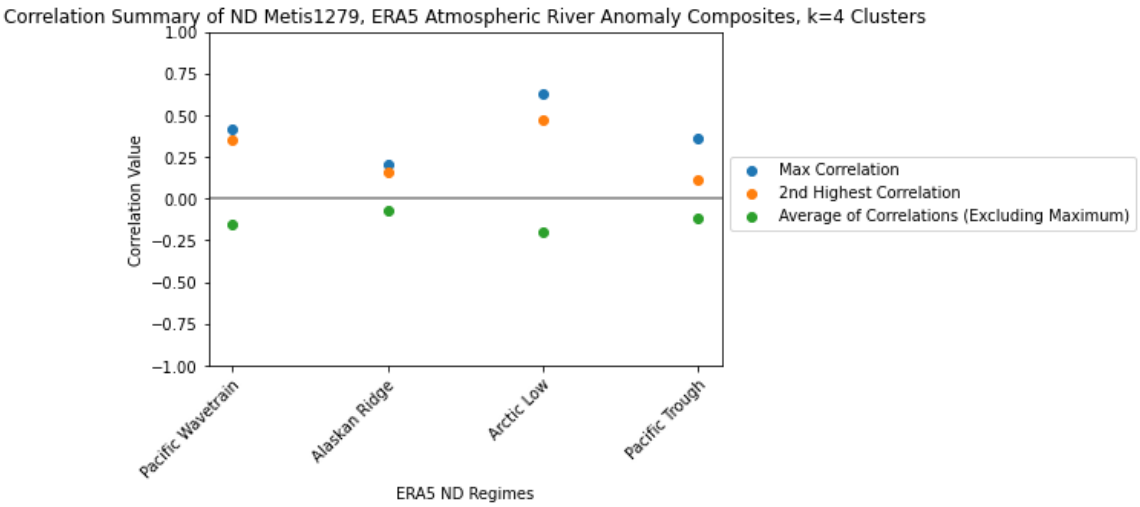

Figure 32 ND 1279, ERA5 November to December k=4, 1st and 2nd Atmospheric River Composite Correlation Summary

DISCUSSION

Circulation Regimes

This section discusses the Circulation Regimes subsections of the Results. The fidelity of circulation regimes is addressed in two manners: spatially and temporally. The spatial section examines the cluster composites and pattern correlations. The temporal section investigates cluster persistence, the significance of differences in the cluster persistence probability density function, and the annual maximum episode length for each cluster.

Spatial

The spatial patterns of the regimes are represented by the anomaly composites found in the Results section Regimes for 4 Clusters. The correlations between the ERA5 reanalysis regime patterns and each of the calculated model regimes are shown in the red and blue tables.

November through March

For k=4 clusters, ERA5 reanalysis demonstrates four distinct regimes: ArcLow, PacTrough, AlRidge, and PacWav. These base regime patterns are nearly identical to those identified for December through February 1980/81-2014/15 in Amini and Straus (2019). Both model resolutions have a decreased regime distinguishability compared to the overall correlations for five regimes (see Figures 50, 51 in the Appendix) and therefore show regime composites that are hybrids of the ERA5 base regimes. We define a hybrid model regime as one which is highly correlated (coefficient $\rho > 0.5$) with more than one base regime (see Figure 5). Hybrids that appear in both resolutions are

PacWav/PacTrough, ArcLow/PacTrough, and AlRidge/PacWave. Metis639, however, has a regime (2) highly correlated with the AlRidge (ρ =.88) with a low second highest correlation (ρ =.3) with the ArcLow, thus indicating that the AlRidge for Metis639 is distinguishable from the ArcLow. This is different from Metis199, which has a hybrid AlRidge/ArcLow regime.

While the two resolutions demonstrate similar hybrid regimes, the summaries (Figure 6, Figure 7) reveal more insight into how well correlated the base regimes are with the model regimes. Compared to Metis199, Metis639 shows an increased distinguishability between the two highest correlated model regimes for the ArcLow, PacWave, and especially the AlRidge, while there is a slight decrease in distinguishability for the Pacific Trough. Generally, the average of the low correlations is consistent between resolutions, indicating that the major differences in the resolutions is in the maximum correlation value.

Comparing ERA5 Base Regimes

ERA5 reanalysis k=4 regimes for November through December demonstrate mostly similar composite patterns as those for November through March *(*Figure 8*)*. Out of these patterns, Arctic Low, Pacific Trough, and Alaskan Ridge are largely consistent with November through March patterns. However, the Pacific Wavetrain demonstrates a relatively significant change, where the anomalies are enhanced on the western edge of the PacNA region for the November to December period. This pattern is similar to the November through March k=5 Arctic High. It is possible that the k=5 Arctic High pattern for November through March, which is a derivative of the k=4 Pacific Wavetrain pattern for November through March, is more dominant in the k=4 pattern for November through

December than the Pacific Wavetrain. Despite this, the high correlations between the two sets of composites indicate the regimes are distinguishable and robust to the various periods (ND vs. NDJFM) within winter.

November through December

For k=4 clusters, an inspection of the correlation summary plots show that Metis639 demonstrates the best distinguishability out of the three resolutions. For all regimes in Metis639, there is a large difference between the two highest correlation values, and the averages of the lowest correlations are more negative than in Metis199 and Metis1279. The best distinguished regimes for Metis639 are the Pacific Wavetrain and Pacific Trough, with the worst being the Alaskan Ridge. Metis199 and Metis1279 also demonstrate a high distinguishability for the Pacific Wavetrain, with the second greatest difference between the two highest values for the Pacific Trough. It's worth noting that the distinguishability for the Alaskan Ridge and the Arctic Low in Metis199 is extremely low, such that the two are nearly indistinguishable. Metis1279's distinguishability for these two regimes is only marginally improved. As such, the order of greatest to least fidelity is Metis639, Metis1279, and Metis199.

Generally, Metis639 demonstrates improved overall pattern correlation to reanalysis compared to Metis199 or Metis1279. This is especially apparent for the November through December period. This result is unexpected, as based on the literature the reasonable expectation is an improvement in the results with increased resolution. One possible reason for the degradation of results in the Metis1279 run relates to the stratospheric biases. The increase in horizontal resolution from the Metis639 to

Metis1279 model was not matched with an increased vertical resolution. The ECMWF model was run with 91 levels for all three horizontal resolutions, however the version of the Metis1279 used for operational forecasting, which was well tested, had 137 levels, as described in Polichtchouk et al., (2019). This reference concludes that discretization errors in the vertical advection, associated with inadequate representation of resolved gravity waves may be responsible for increased errors at the highest resolution. The model biases in the climatological mean zonally averaged zonal wind (u) and temperature (T) with respect to ERA-Interim are shown for all three resolutions in Figure 33 and Figure 34. There is a clear increase in the T bias in the mid-stratosphere as resolution is increased, which provides some tentative support for the hypothesis put forward above.

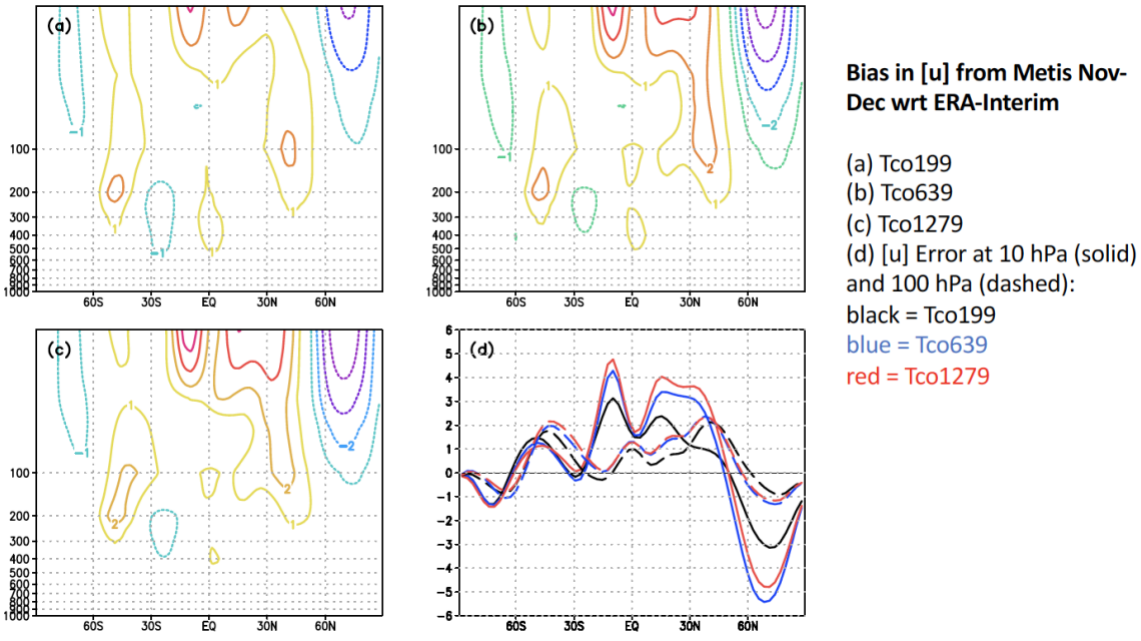

Figure 33 Metis Nov-Dec Zonal Wind Bias with Respect to ERAI

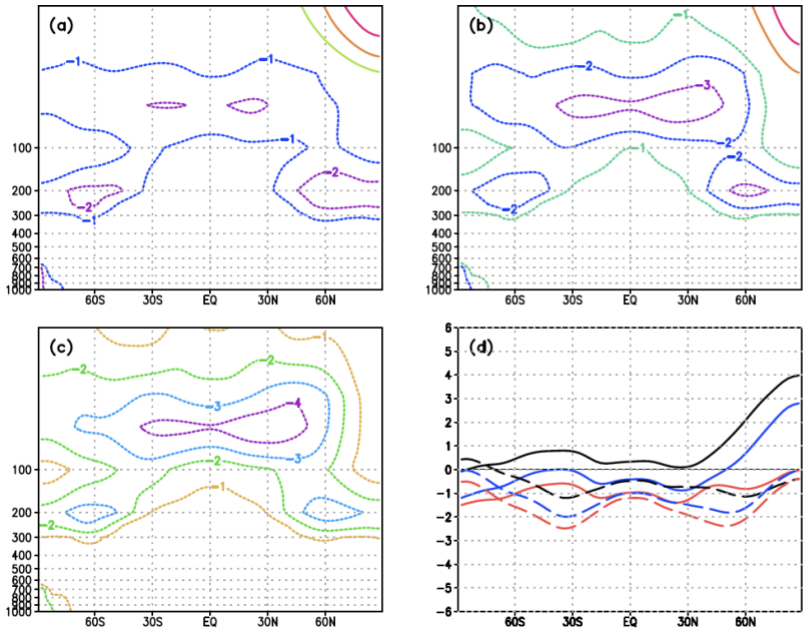

Figure 34 Metis Nov-Dec Temperature Bias with Respect to ERAI

Temporal

The temporal aspect of regime fidelity is addressed in Results (Cluster Persistence), where the distributions of episode length for each regime is plotted as a histogram of frequency of occurrence within the regime. Again, an episode is defined as a time series where the same regime occurs consecutively. A Kilmogorov-Smirnov test of the episode distributions for each regime gives a statistic that measures how well the model distributions differ from those from ERA5. The p-values for the null hypothesis that the distributions are the same are given for each pair of regimes in the results. A larger p-value indicates a higher confidence that the distributions are the same. Here we discuss the results for a 90% confidence interval, $\alpha = .1$, where we can say with 90%

confidence that if $p < \alpha$, the distributions are different, or if $p > \alpha$, that the distributions are the same.

Histograms

For November to March, k=4 clusters, we have hybrid regimes with which to make our comparisons. Because of the hybrid regimes, we find that we partially reject the null hypothesis for the Pacific Trough and Pacific Wavetrain for ERA5 vs Metis199 and Metis639 (Table 4). Specifically, the null hypothesis rejected is that the ERA5 Pacific Trough distribution, or the Pacific Wavetrain distribution, is the same as the Metis199 or Metis639 Hybrid Pacific Wavetrain/Pacific Trough, a hybrid that appears in both resolutions. In Figure 14, the ERA5 Pacific Trough and Pacific Wavetrain distributions demonstrate an almost bi-modal distribution, with a secondary peak at about 15 days (30 units), as in the k=5 November to March Pacific Wavetrain, Arctic High, and Alaskan Ridge distributions. This behavior is not demonstrated by either the Metis199 or Metis639 Hybrid Pacific Wavetrain/Pacific Trough, which are not weighted as strongly at the 15 day (30 unit) mark.

For November to December, k=4 clusters, we partially reject the null for ERA5 vs Metis199 and Metis1279 Alaskan Ridge (Table 5). Specifically, we reject the null hypothesis that the ERA5 Alaskan Ridge distribution is the same as Metis199 or Metis1279 Hybrid Pacific Wavetrain/Alaskan Ridge. It should be noted that the Alaskan Ridge is fully accepted for the Metis639 resolution, which does not have hybrid regimes for this time period.

Generally, the ERA5 distributions that are not well-represented by the Metis resolutions tend to be nearly bi-modal with a secondary maximum at around 15 days (30

units). This implies that when the model does not well represent the episodes, it does so by underestimating their length. The November-December Metis distributions better represent ERA5 distributions than their longer November-March counterparts. K=4 Metis distributions better represent more ERA5 regimes than k=5. This is partly due to the hybrids, which allow for some flexibility in identifying the temporal matches, but it's important to note that all of k=4 November-December Metis639 distributions are statistically equivalent to their ERA5 counterparts, which can't be said for any other resolution. K=5 ERA5 Pacific Wavetrain and Arctic High are statistically different from their Metis counterparts for both time periods. The November to March period seems to have some difficulty reproducing the Pacific Wavetrain distribution well.

Annual Maxima of Episode Length

We calculated the annual maxima of episode length for each regime. We examine the results to identify interesting phenomena. One such phenomena that is evident is for the ERA5 reanalysis. Examining the k=4 November to March ERA5 maximum annual persistences (Figure 16), we see that the Pacific Trough tends to exhibit large maximum episode lengths during El Nino years (i.e. 1991, 1997, 2002, 2009, and 2015). However, unlike in k=5, the Pacific Wavetrain isn't as predictable on the basis of ENSO. The Pacific Trough is also influenced by ENSO in the Metis199 and Metis639 forecasts (e.g. Hybrid PacTrough/ArcLow in 1997 and 2015). That these two years represent episodes of twice the maximum persistence in the ERA5 implies that the model conditions of strong El Nino dramatically enhance the persistence of this regime for k=4 clusters. The k=4 November to December period for ERA5 (Figure 17) has significantly fewer events of the Pacific Wavetrain than other regimes. This is similar to the Arctic High in k=5. For

these regimes there are some years where there are no events. This is not represented by the Metis results.

Atmospheric Rivers

Total Atmospheric Rivers

The number of atmospheric rivers calculated for ERA5 (Figure 18 and Figure 20) using the 90% of ERA5 moisture flux magnitudes (259.0kg/ms) is consistent with previous works (Lavers et al. 2012, Payne and Magnusdottir 2014). The total number of atmospheric rivers calculated for the different Metis forecasts (Figure 19 and Figure 21) however, is less than the number in ERA5 by a factor of 1/3 (1/2) for the November to March (November to December) period. It's possible that this discrepancy is due to the use of a single moisture flux threshold to identify the rivers, which would imply that the Metis models underestimate occurrences of large moisture flux. It should be pointed out that the location and general intensity of the majority of the rivers in ERA5 over the Pacific Ocean, Southeast US, and the Atlantic Ocean are well described at all Metis resolutions.

Determining the reason for the general model weakness in the number of atmospheric rivers is beyond the scope of this paper. The results still allow for creating spatial composites of the atmospheric river anomalies for the different regimes, so that we might compare the regime-specific patterns of the model with ERA5.

Composites and Correlations

For k=4 November to March, the hybrids again are largely correlated with the atmospheric rivers associated with their ERA5 base regimes. We examine the ERA5

atmospheric river anomalies to see how the regimes modulate them. The Arctic Low narrows the river occurrences over the Pacific to a central band in the midlatitudes, shifts the rivers southwest over the SE US, and decreases the number of rivers over the Atlantic. The Pacific Trough shifts the rivers southward in the Pacific and decreases the number of rivers over the SE US. The Alaskan Ridge shifts atmospheric rivers northward over the Pacific and increases the number of rivers over the SE US. Finally, the Pacific Wavetrain demonstrates a general increase in the number of atmospheric rivers over the PacNA region, especially over the oceans. While Metis199 well reproduces the ERA5 Pacific Trough atmospheric rivers for the Nov-Mar period, and there is some ambiguity in the improvement of maximum correlations between the two resolutions, there seems to be more distinguishability for Metis639.

The November to December regimes also influence the atmospheric rivers. The Arctic Low generally decreases the number of rivers over the PacNA region. The Pacific Trough enhances the rivers over the Pacific and decreases the rivers over the SE US (similar to November to March). The Alaskan Ridge shifts the rivers northwest over the Pacific (similar to November to March) and west over the SE US (similar to the enhancement over the SE US seen in November to March). The Pacific Wavetrain generally demonstrates an increase over the PacNA region, especially over the oceans and slightly over the SE US (as in November to March). The November to December regimes influence on atmospheric rivers is similar to that of the November to March regimes. For k=4 November to December, some of the hybrids appear to be decoupled from their base regimes, as happened for k=5 November to December, but some still

correlate well. For this period and cluster number, Metis639 is largely an improvement over both Metis199 and Metis1279.

CONCLUSIONS

To investigate how the modeling of circulation regimes is impacted by an increase in the forecast model's resolution, circulation regimes for an extended winter period (November to March) and a shorter period (November to December) were calculated for the Pacific North America region from 1986-2015 for ERA5 reanalysis and for Metis simulations run at three different horizontal resolutions (Metis199, Metis639, and Metis1279, which correspond to a grid size of 100km, 31km, and 16km, respectively). The calculations were done using a clustering method on the leading PC's of the 10-day low-pass filtered z500 and u250 anomaly data for k=4 and k=5 clusters. The accuracy of spatial patterns of the regimes as represented by the forecasts is measured by the pattern correlation between the k=5 and k=4 z500 regime anomaly composites of ERA5 and the different Metis resolutions.

A description of the regime anomaly patterns follows for the November to March period. For k=4, the identified regimes are the Arctic Low, Pacific Trough, Alaskan Ridge, and Pacific Wavetrain. The same regimes are identified for k=5, with the addition of the Arctic High. The Arctic Low has a z500 trough around Alaska, though the k=4 and k=5 placement of this trough isn't the same. The Pacific Trough has a large z500 trough over the central Pacific. The Alaskan Ridge has a strong z500 peak over central Pacific that extends across Alaska. The Pacific Wavetrain demonstrates a wave-like pattern of z500 peaks and troughs starting in the central Pacific and extending over North America.

Though the ridges and troughs are swapped between k=4 and k=5, the naming convention is based on the nature of the wave-like pattern.

We found that the modeled k=4 November to December regimes for Metis639 demonstrate unique associations with individual ERA5 regimes. However, the other resolutions and time period (November to March) reveal modeled hybrid regimes, which display significant (>50%) correlation with more than one ERA5 regime. In examining the difference between the first and second greatest correlations associated with the ERA5 regimes, we determine that the Metis639 resolution demonstrates higher spatial prediction skill of the observed regimes, with generally enhanced correlation values and distinguishability from other regimes. Particularly, Metis639 of k=4 November to December demonstrates the most skill when compared to Metis199 and Metis1279. This result is unexpected, as based on the literature, the reasonable expectation would be for an improvement in the results as resolution increased. One possible reason for this discrepancy is that the Metis simulations used 91 levels for all resolutions. Since the version of Metis1279 IFS used at ECMWF was operationally tested only for 137 levels, there is a possible source of error. This is tentatively supported by a clear increase in temperature bias in the mid-stratosphere as resolution is increased.

One of the aspects of circulation regimes is their persistence. We calculated the length of each occurrence, or episode, in units of 12 hours. The probability distribution of episode length, shown as a histogram, shows how persistent regimes are in a given period of time. We used the Kilmogorov-Smirnov test to identify when we are 90% confident that the episode length probability distribution of a modelled regime is different from an

observed regime. Generally, the ERA5 persistence distributions that are significantly different from the model distributions demonstrate an almost bi-modal shape, with a minimum and a secondary maximum at around or beyond 15 days (30 units). In these cases the model tends to underestimate the episode length of the observed regimes. The best representation of episode length distribution is Metis639 k=4, November to December. Generally, for k=4 the model tends to perform better than for k=5, and performs better for November to December than for November to March. The k=5 model results demonstrates that the Pacific Wavetrain and Arctic regime patterns are not well represented by the associated model regimes for either November to December or November to March. Additionally, the Pacific Wavetrain regime is not well represented for k=4 or k=5 November to March.

A measure of interest in the episode length is the annual maximum. We find that during El Niño years, the maximum episode lengths for the Pacific Trough are at their largest for November through March, k=4 and k=5. There is a similar El Niño influence on the Pacific Wavetrain for November through March, k=5, but not so for k=4. This influence is seen in the Metis199 and Metis639 results for November through March. However, November through December does not demonstrate such an influence, probably because the extra-tropical response to El Niño generally occurs later in the winter.

In ERA5 for k=4 (k=5) November to December, the Pacific Wavetrain (Arctic High) never occurs during certain winters. This is not represented by the Metis results, although the Metis sample size is much larger. Generally speaking, the Metis simulations

appear to overestimate the maximum regime episode length by a factor of 2. Thus while the model generally under-estimates the episode length, it occasionally produces a very long episode.

Since the circulation regimes are largely well-correlated in space, and decently similar in length of episode, we used the time series of cluster indices to identify atmospheric river composites for comparison between the reanalysis and the model at different resolutions. First, in calculating the atmospheric rivers, we examined the total number of rivers identified. We found that the model tends to undercount the atmospheric rivers by 1/3 (1/2) for the November to March (November to December) period. This could indicate that the threshold for ERA5 moisture flux values is too strict for the Metis data. Identifying a suitable threshold for the Metis models is future work. It was suggested by David Lavers of ECMWF (personal communication) that going forward we should identify the probability distribution of the Metis data at different lead times, and to test the possibility that the moisture flux decreases with lead time. While the total number of atmospheric rivers is undercounted, the models still well represent the geographical location of river occurrences, and so can be used for examining how well the spatial anomalies of atmospheric rivers are represented by the model.

Examining the ERA5 atmospheric river anomaly regime composites shows how the regimes identified modulates the atmospheric rivers. The largest influences are over the Pacific, the southeast US, and the Atlantic. For both time periods, the Pacific Wavetrain generally enhances the number of atmospheric river occurrences in the PacNA region, especially over the oceans, and secondarily over the southeast US. The Alaskan

Ridge shifts the rivers northward over the Pacific and enhances river occurrence over the southeast US. The Arctic Low generally decreases river occurrence over the Pacific, with the exception of a band in the mid-latitudes. The Pacific Trough enhances river occurrence over the more subtropical latitudes in the Pacific and decreases it over the southeast US.

The influence of resolution on the atmospheric rivers is less obvious than for the circulation regimes. The pattern correlations of the regime-specific anomalous atmospheric river counts tend to follow the z500 correlations identified, even for the Metis resolutions that demonstrate spatial hybrid regimes. As in the z500 correlation, the best representations occur for Metis639 k=4 November to December, with improvements over Metis199 and Metis1279. Examining the other periods and clusters, we see that generally Metis639 demonstrates enhanced distinguishability (clearest one-to-one mapping with the ERA5 reanalysis) when compared with the other resolutions, though it does not always show the greatest pattern correlation. This ambiguity is strongest for the November to March periods. Therefore, as opposed to the strong result seen for the November-December z500 correlations, the atmospheric river regime-specific patterns don't match the reanalysis as well.

Some overall conclusions follow. The circulation regimes are best spatially reproduced by the Metis639 resolution. The probability distribution of episode lengths is also best reproduced by the Metis639 resolution, although the Pacific Wavetrain persistence is consistently ill-represented in the November to March period. El Niño conditions favor an enhanced Pacific Trough maximum episode length in the November

to March period, an influence which is represented by Metis199 and Metis639 resolutions.

The identification of atmospheric rivers shows that with a fixed moisture flux threshold, the model systematically undercounts rivers, though the locations of rivers are consistent with the reanalysis. Future work will be needed to investigate the probability distribution of moisture flux with respect to lead time. The regimes modulate the river occurrences over the Pacific, Atlantic, and southeast US. The modeled atmospheric river regime anomalies are generally correlated with the same base ERA5 regimes as are the z500 regime anomalies. Generally, Metis639 demonstrates an enhanced distinguishability, especially for the November to December period, though the November to March results are more ambiguous.

The difference in skill between the different datasets is due to several factors. The medium resolution of Metis639 demonstrates the best results. The reason for this improvement with respect to the coarse Metis199 resolution is obvious: the resolution is increased. However, it is unclear why the highest resolution Metis1279 doesn't demonstrate similar results (at the very least!) as Metis639. The k=4 clustering shows better relations between ERA5 and the forecasts than the k=5 clustering, which is understandable as more patterns are resolved for the k=5 clustering. Finally, the November to December model results demonstrating significantly better skill than the November to March model results is reasonable, since the November to December period is closer to the model's initial conditions.

Some implications for improving forecasting can be drawn from these results. Assume that forecast regimes are used to infer forecasts of atmospheric rivers. Increasing the number of regimes decreases the skill of the forecast. Therefore, using as few regimes as possible improves the forecasting. Additionally, the forecast skill decreases as lead time increases, such that a shorter period of time demonstrates improvement over the longer period of time. Altogether, using fewer regimes for shorter periods of time (on the scale of two months) is suggested for using forecast regimes to infer atmospheric river statistics.

APPENDIX

K=4 Metis Results

U250 Correlation

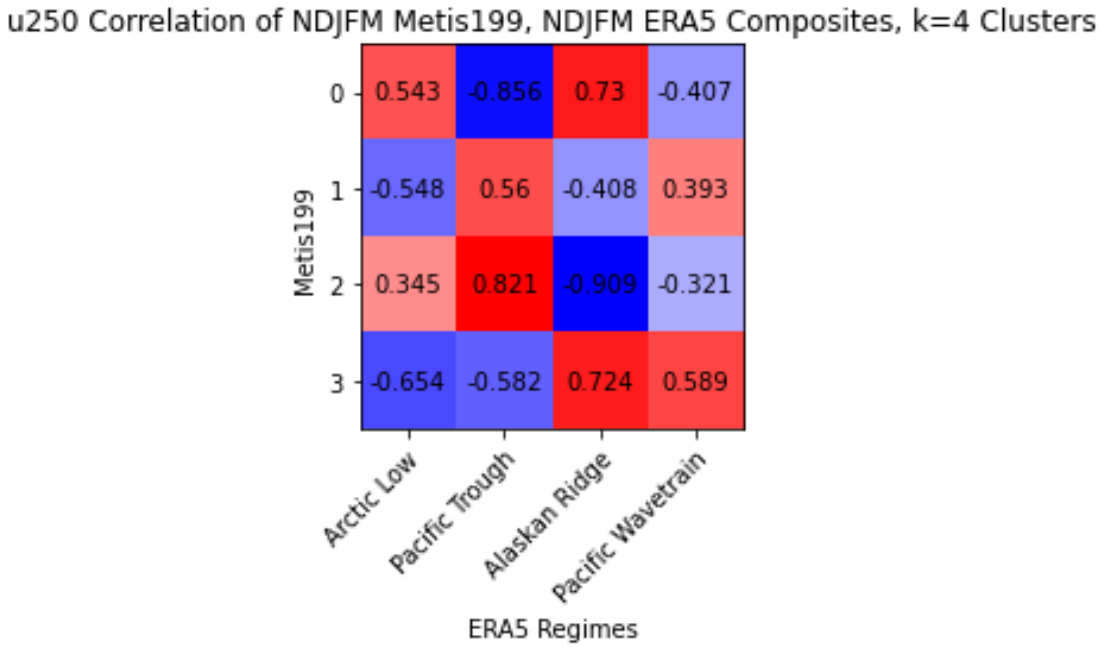

Figure 35 November to March k=4 Metis199, ERA5 U250 Regime Correlations. ERA5 November to March regimes on x-axis. Metis199 regimes on y-axis. Red (blue) indicates strong positive (negative) correlation. White is weak correlation. Note similarity between U250 correlations and Z500 correlations.

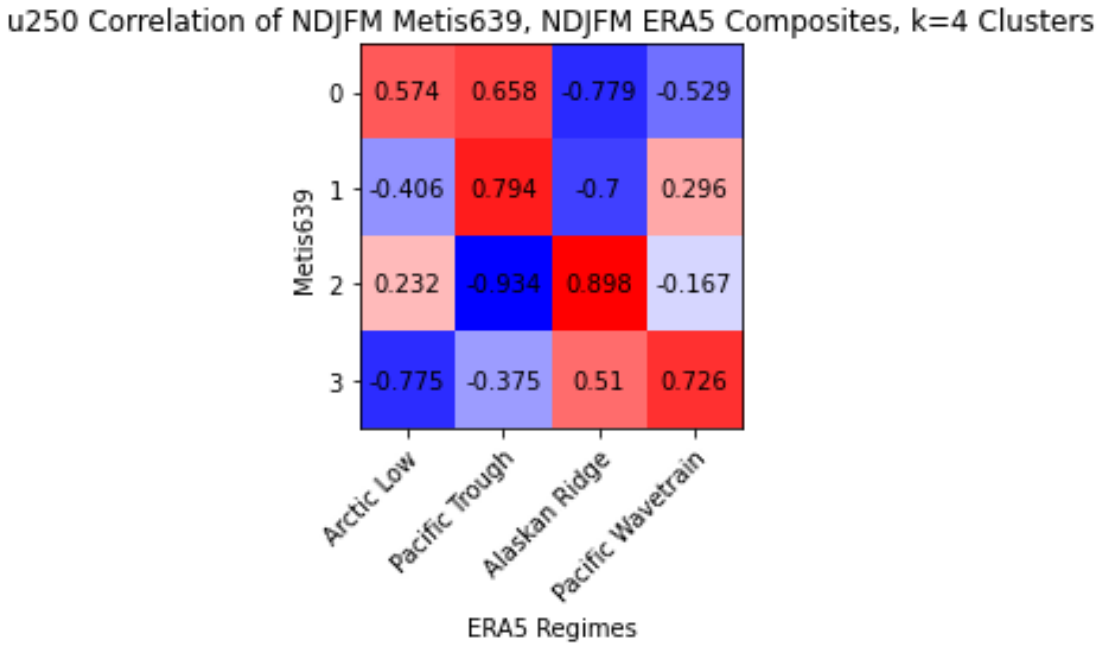

Figure 36 November to March k=4 Metis639, ERA5 U250 Regime Correlations. ERA5 November to March regimes on x-axis. Metis639 regimes on y-axis. Red (blue) indicates strong positive (negative) correlation. White is weak correlation. Note similarity between U250 correlations and Z500 correlations.

Z500 Composites

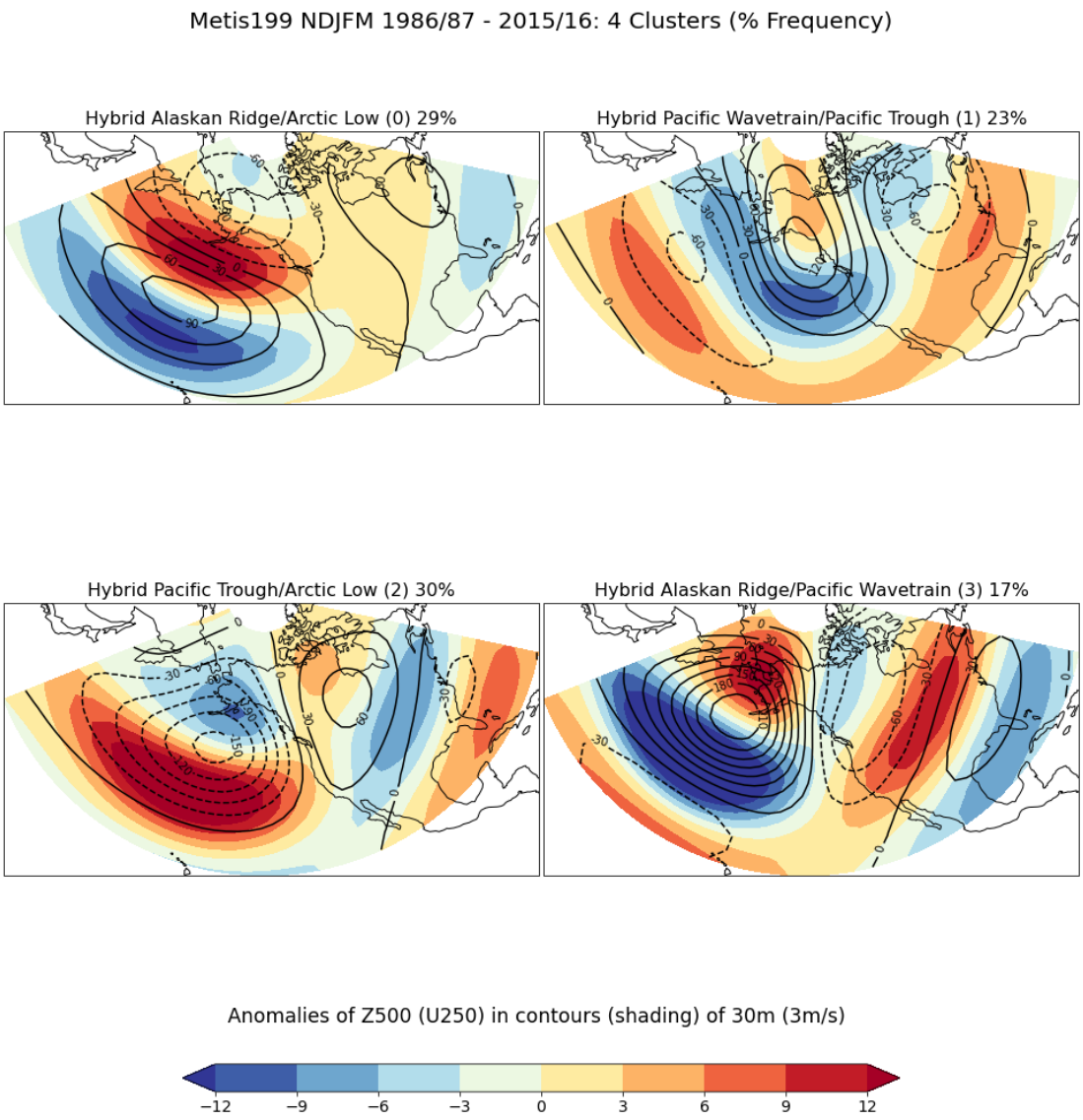

Figure 37 November to March k=4 Metis199 Z500(U250) Cluster Anomaly Composites. Z500 in contours, U250 in shading. Cluster frequency of occurrence given by the percentage. Regime names based on Z500 structures.

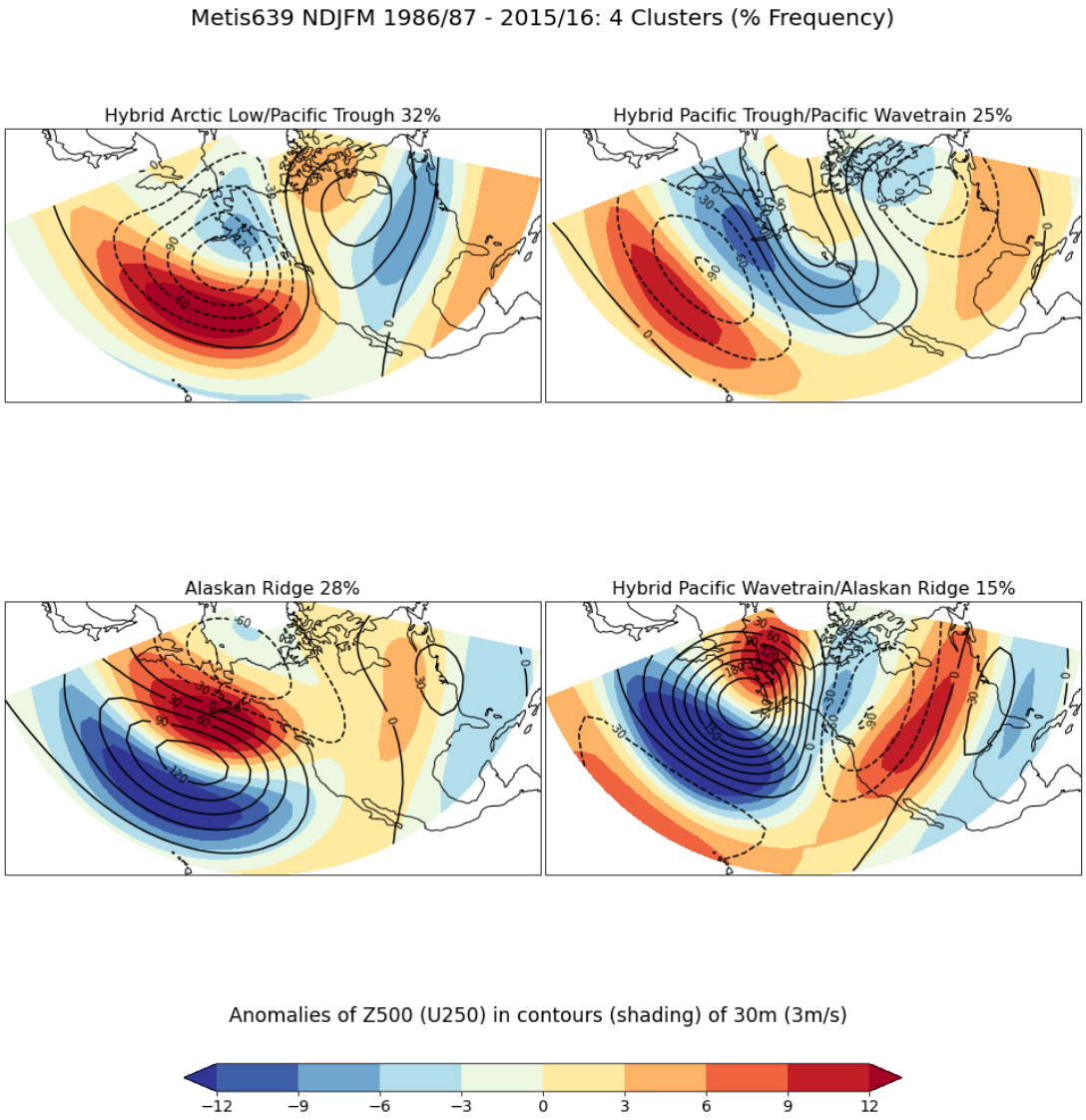

Figure 38 November to March k=4 Metis639 Z500(U250) Cluster Anomaly Composites. Z500 in contours, U250 in shading. Cluster frequency of occurrence given by the percentage. Regime names based on Z500 structures.

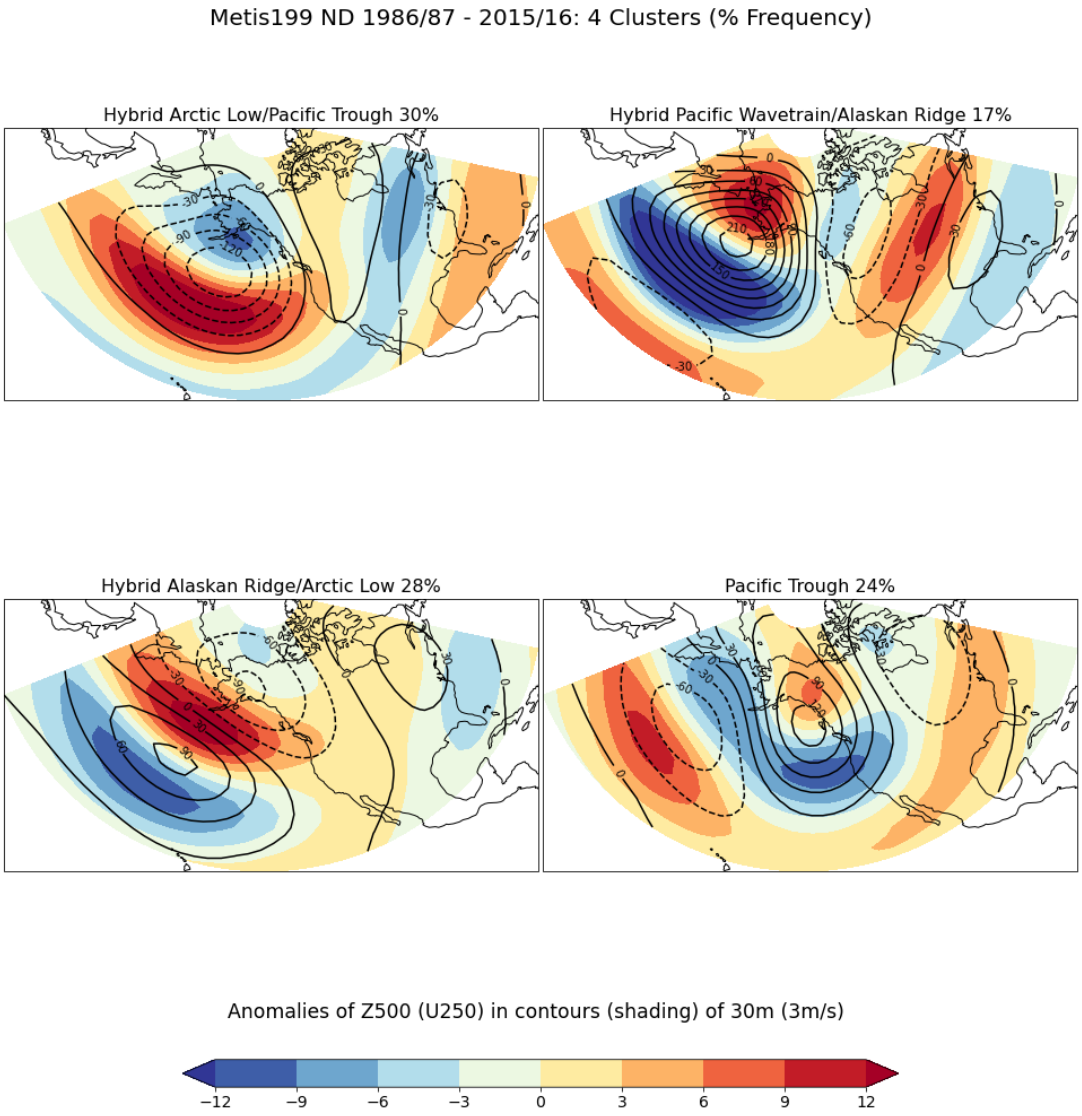

Figure 39 November to December k=4 Metis199 Z500(U250) Cluster Anomaly Composites. Z500 in contours, U250 in shading. Cluster frequency of occurrence given by the percentage. Regime names based on Z500 structures.

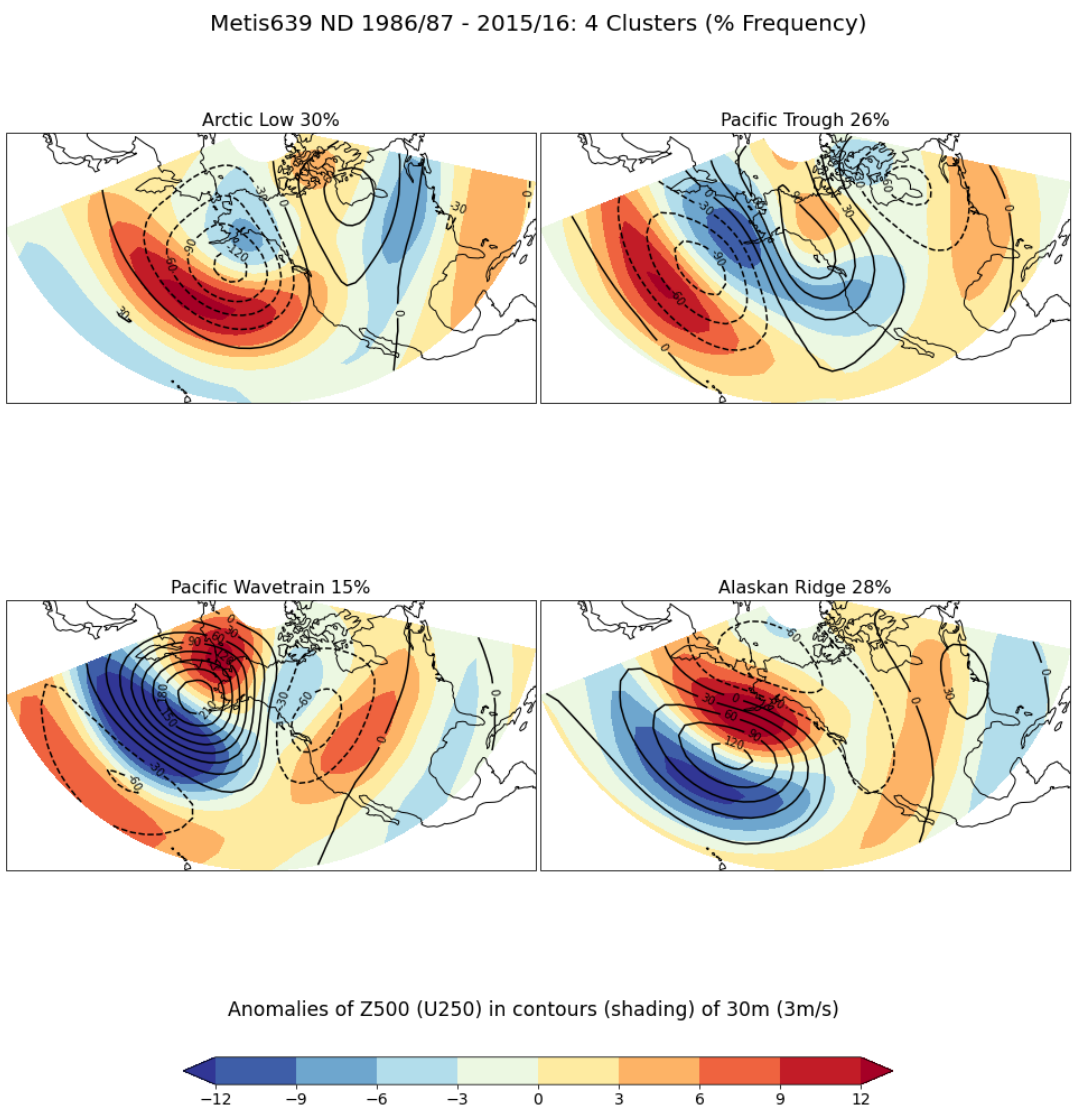

Figure 40 November to December k=4 Metis639 Z500(U250) Cluster Anomaly Composites. Z500 in contours, U250 in shading. Cluster frequency of occurrence given by the percentage. Regime names based on Z500 structures.

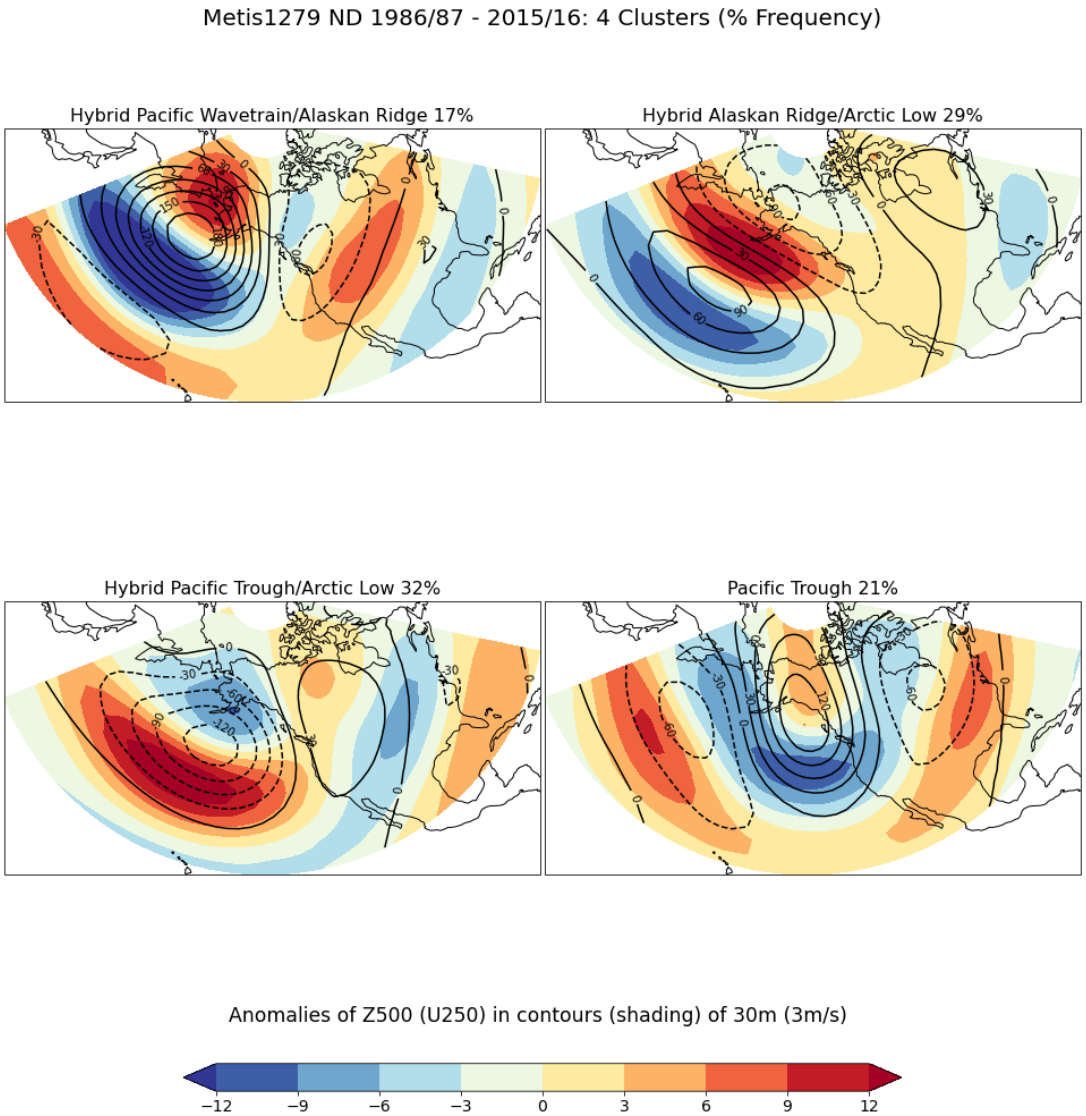

Figure 41 November to December k=4 Metis1279 Z500(U250) Cluster Anomaly Composites. Z500 in contours, U250 in shading. Cluster frequency of occurrence given by the percentage. Regime names based on Z500 structures.

Atmospheric River Composites

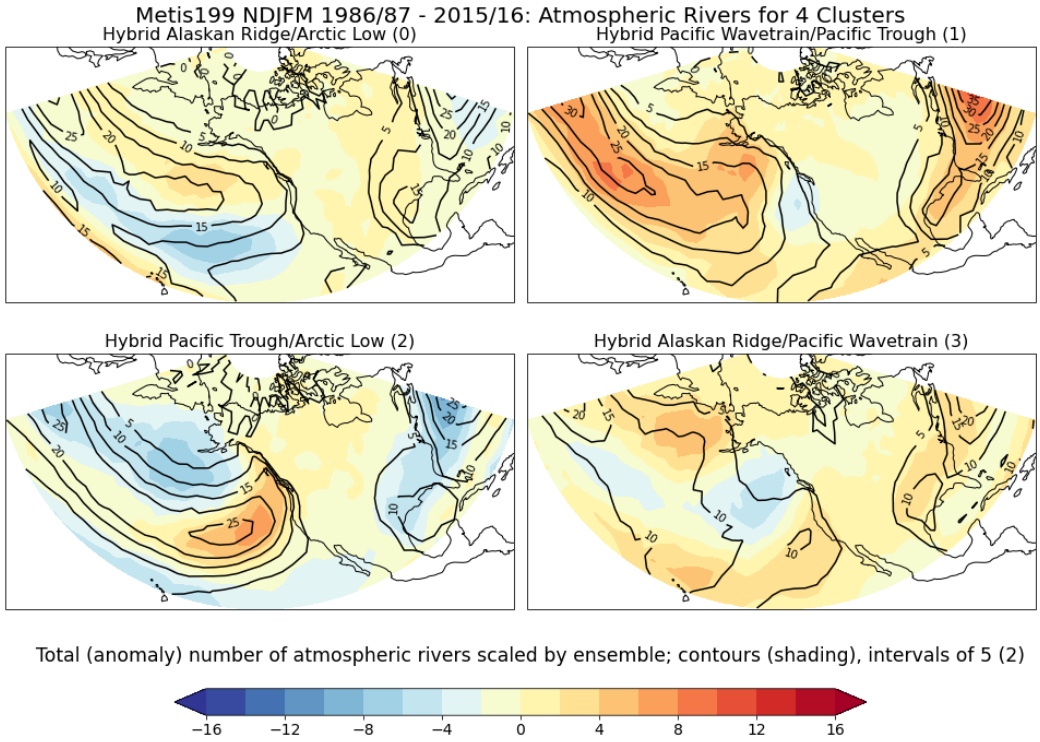

Figure 42 November to March K=4 Metis199 Atmospheric River Regime Composites. Total (anomalous) atmospheric river counts per regime given by contour (shading). Regimes named based on Z500/U250 composites. Positive (negative) anomalies shown in red (blue) shading.

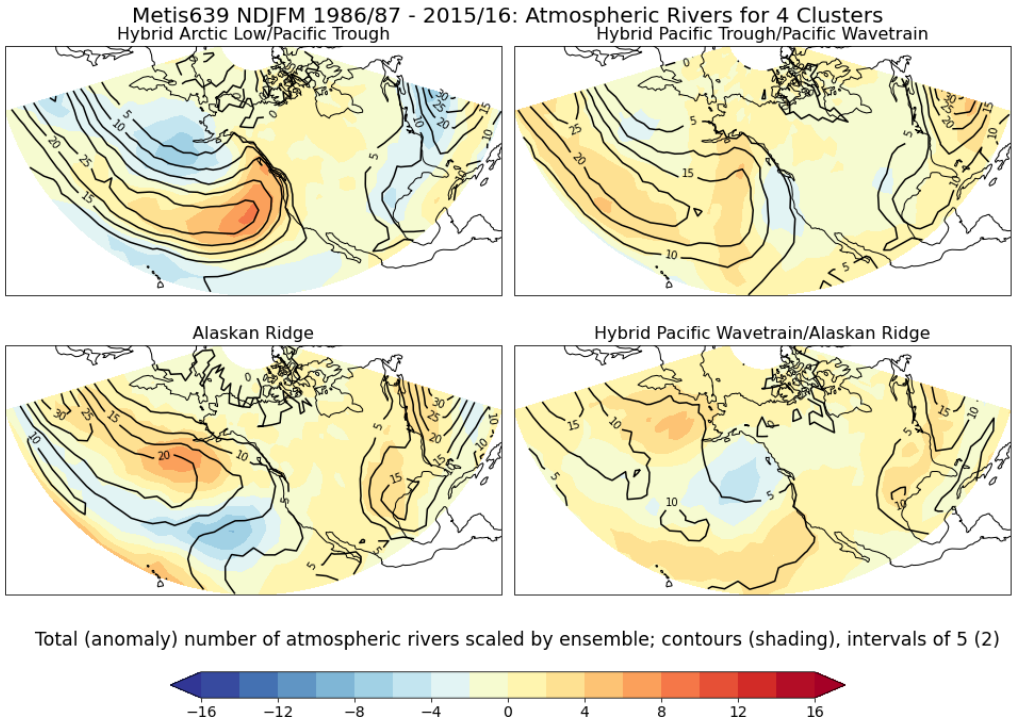

Figure 43 November to March K=4 Metis639 Atmospheric River Regime Composites. Total (anomalous) atmospheric river counts per regime given by contour (shading). Regimes named based on Z500/U250 composites. Positive (negative) anomalies shown in red (blue) shading.

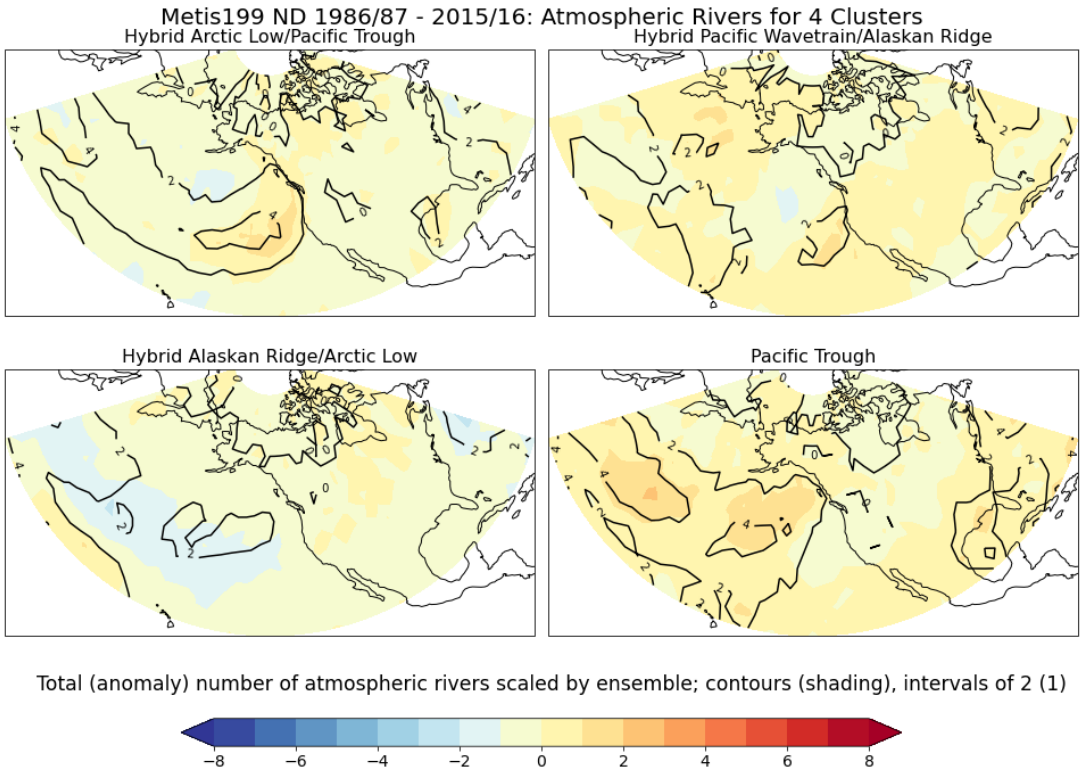

Figure 44 November to December K=4 Metis199 Atmospheric River Regime Composites. Total (anomalous) atmospheric river counts per regime given by contour (shading). Regimes named based on Z500/U250 composites. Positive (negative) anomalies shown in red (blue) shading.

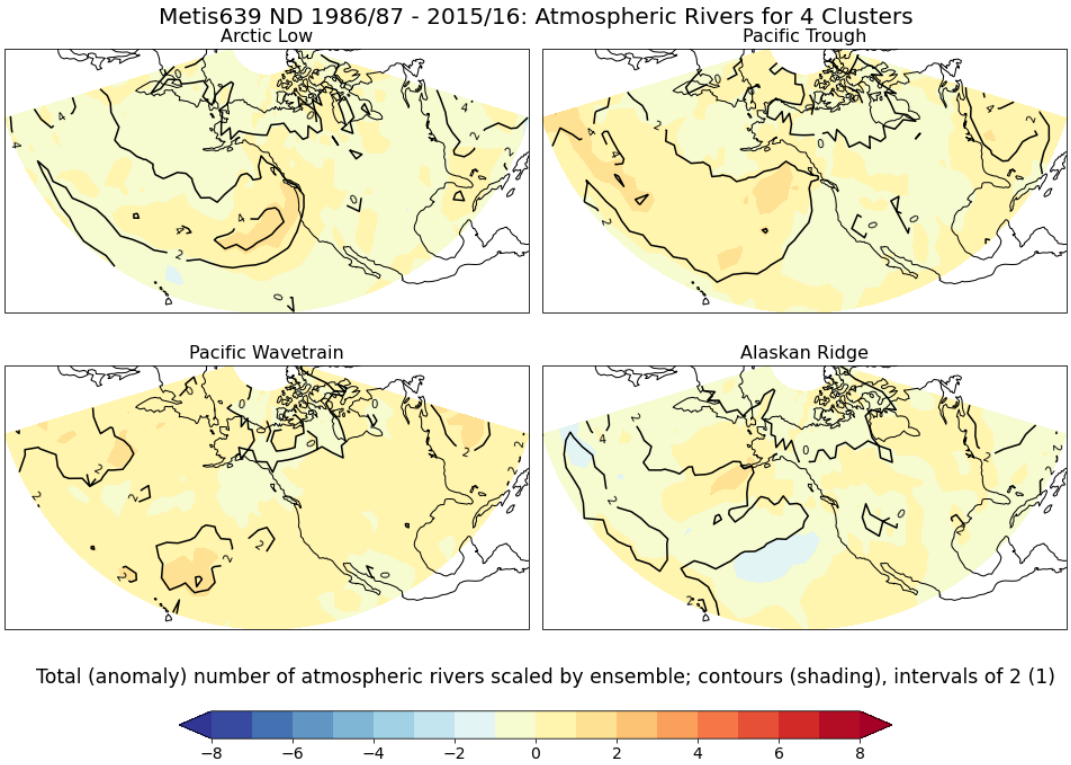

Figure 45 November to December K=4 Metis639 Atmospheric River Regime Composites. Total (anomalous) atmospheric river counts per regime given by contour (shading). Regimes named based on Z500/U250 composites. Positive (negative) anomalies shown in red (blue) shading.

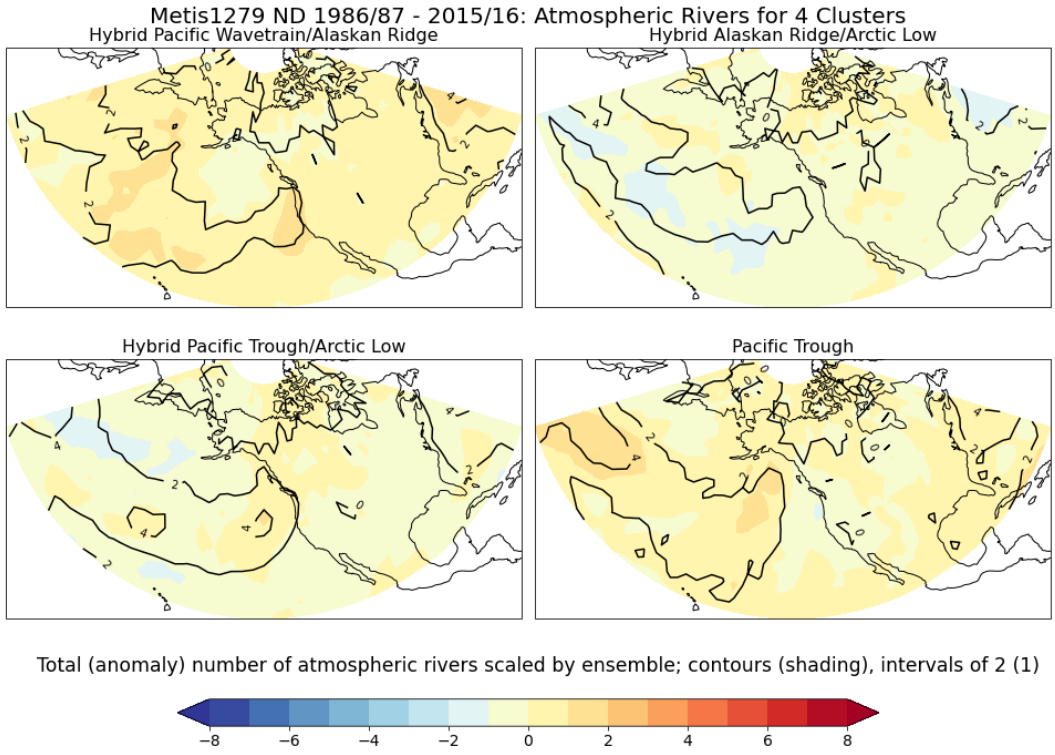

Figure 46 November to December K=4 Metis1279 Atmospheric River Regime Composites. Total (anomalous) atmospheric river counts per regime given by contour (shading). Regimes named based on Z500/U250 composites. Positive (negative) anomalies shown in red (blue) shading.

K=5 Results

Z500 Composites and Correlation

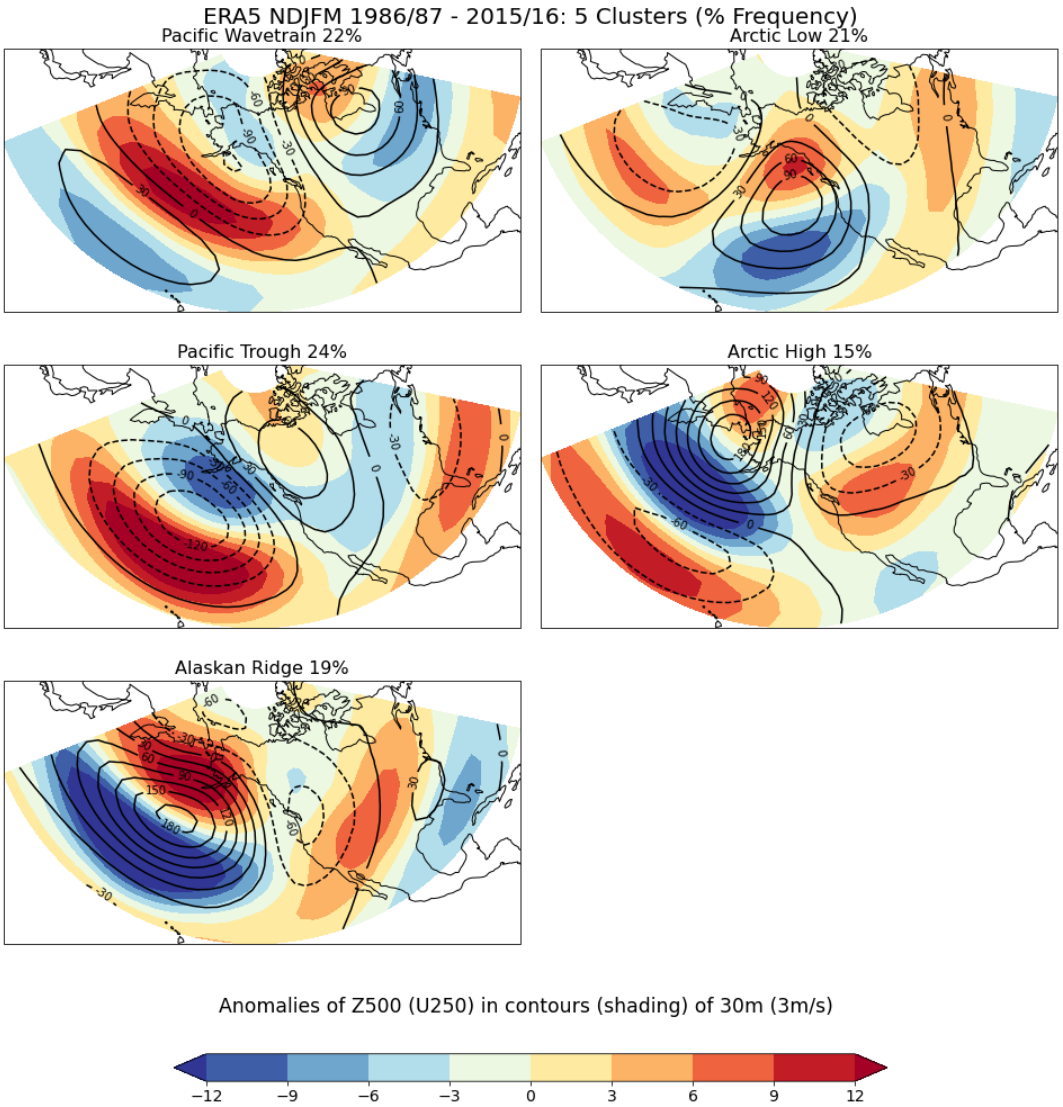

Figure 47 November to March K=5 ERA5 Z500(U250) Cluster Anomaly Composites. Z500 in contours, U250 in shading. Cluster frequency of occurrence given by the percentage.

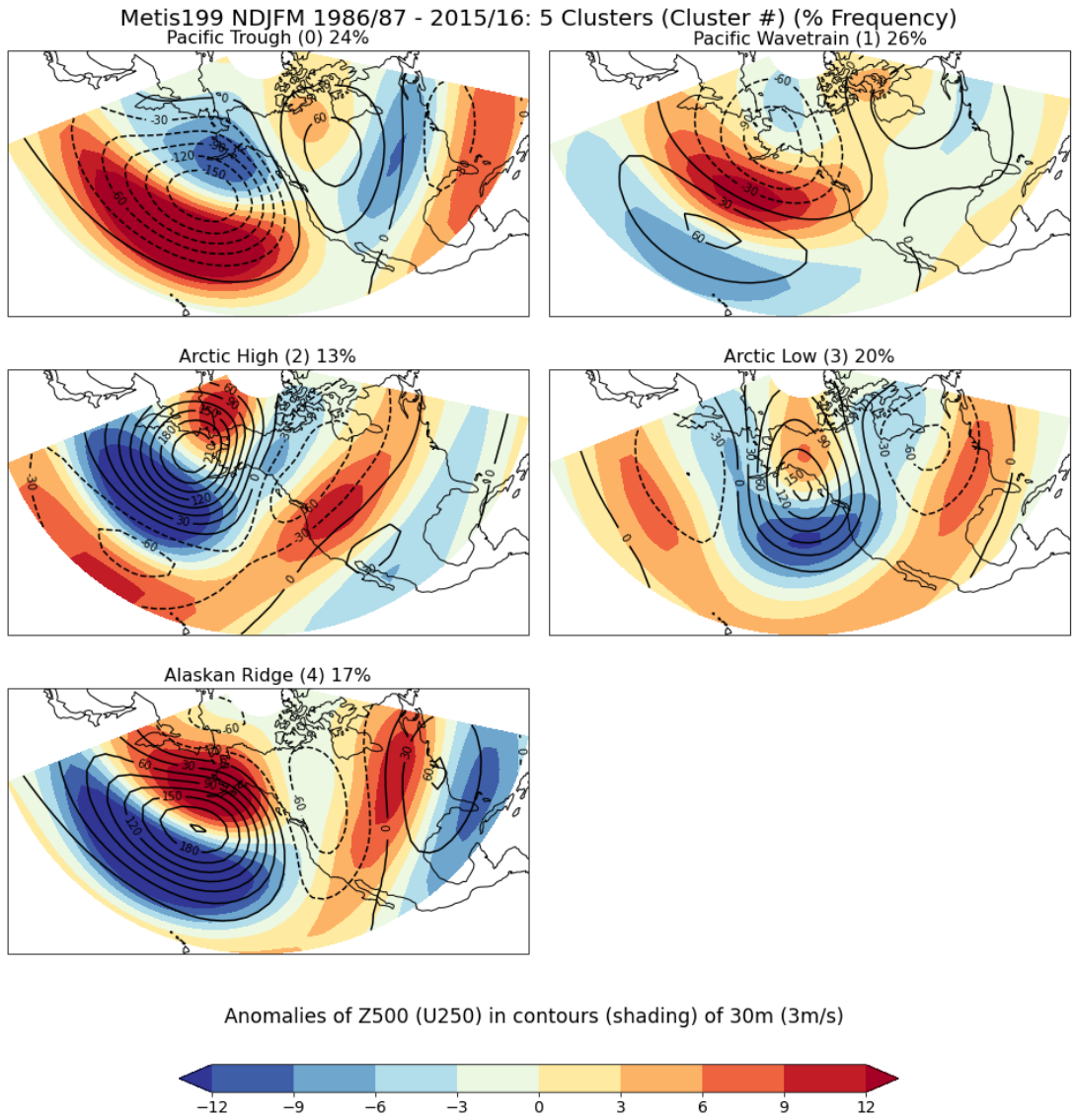

Figure 48 November to March K=5 Metis199 Z500(U250) Cluster Anomaly Composites. Z500 in contours, U250 in shading. Cluster frequency of occurrence given by the percentage. Regime names based on correlation in Z500 structures with NDJFM ERA5 structures.

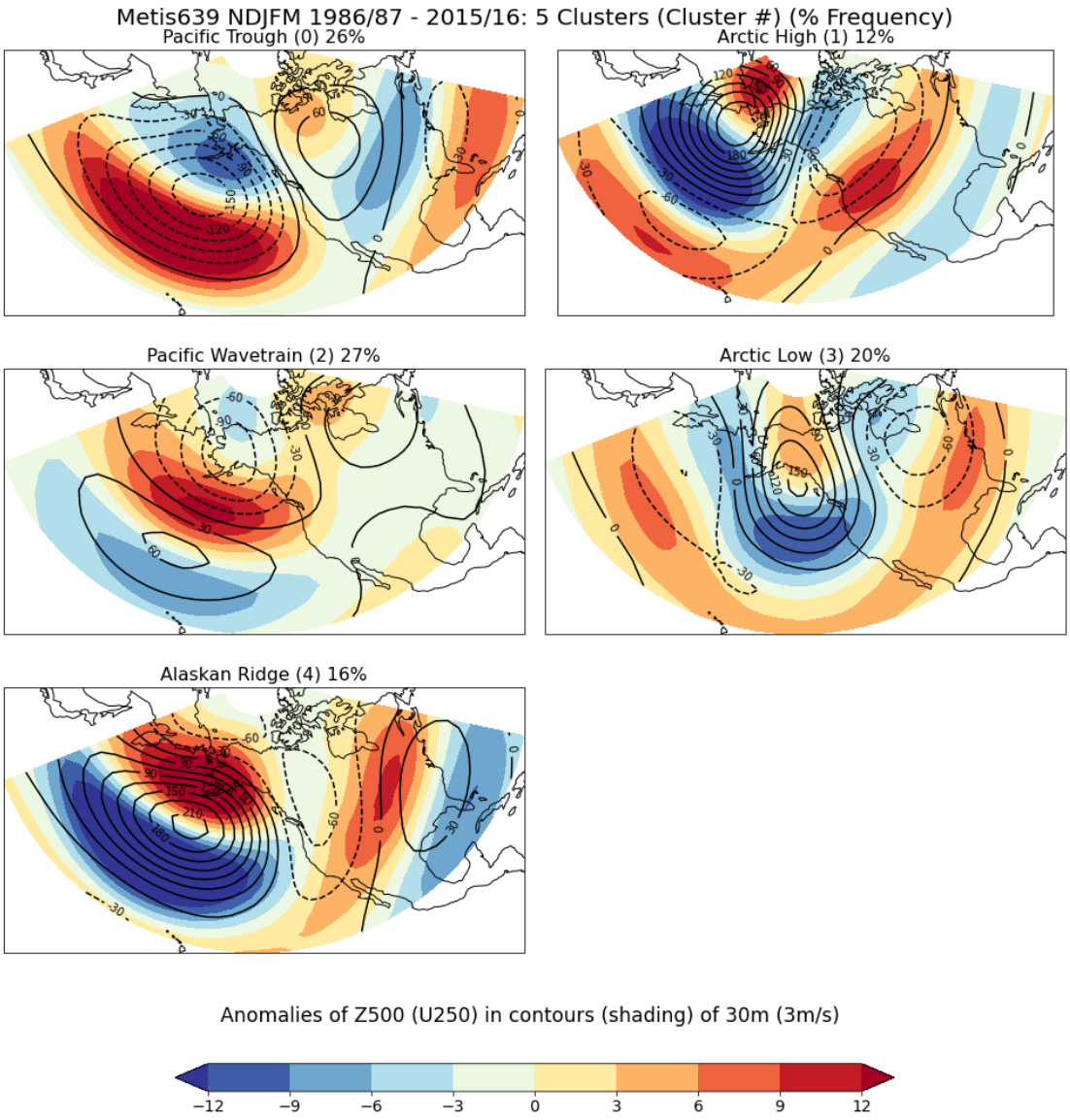

Figure 49 November to March K=5 Metis639 Z500(U250) Cluster Anomaly Composites. Z500 in contours, U250 in shading. Cluster frequency of occurrence given by the percentage. Regime names based on correlation in Z500 structures with NDJFM ERA5 structures.

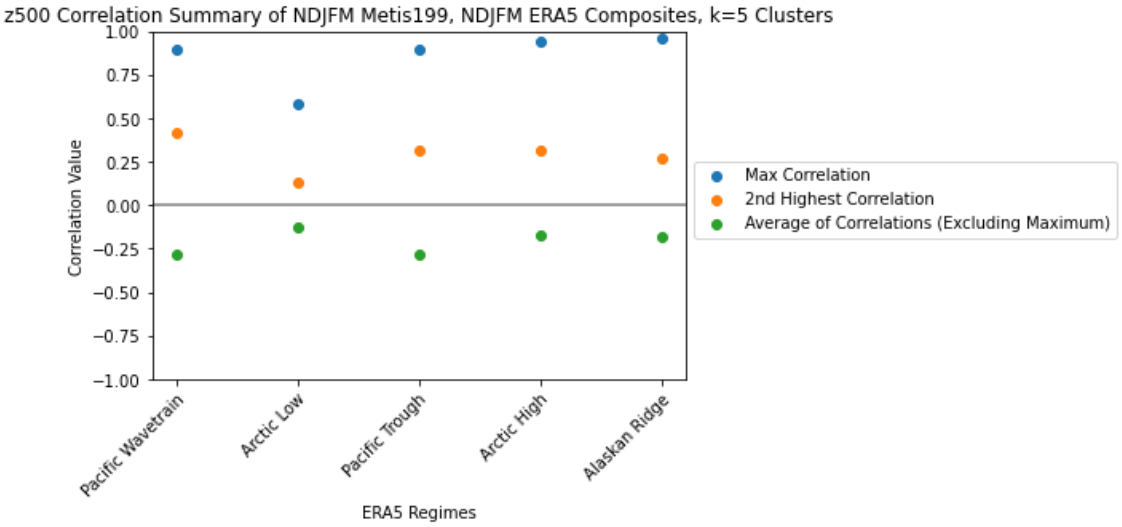

Figure 50 NDJFM Metis199, ERA5 k=5, 1st and 2nd Composite Correlation Summary

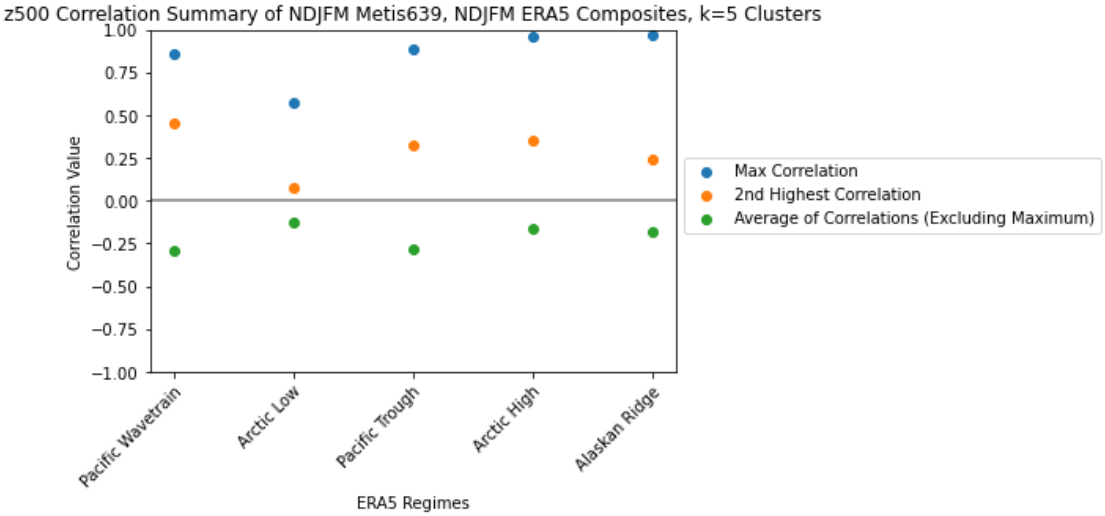

Figure 51 NDJFM Metis639, ERA5 k=5, 1st and 2nd Composite Correlation Summary

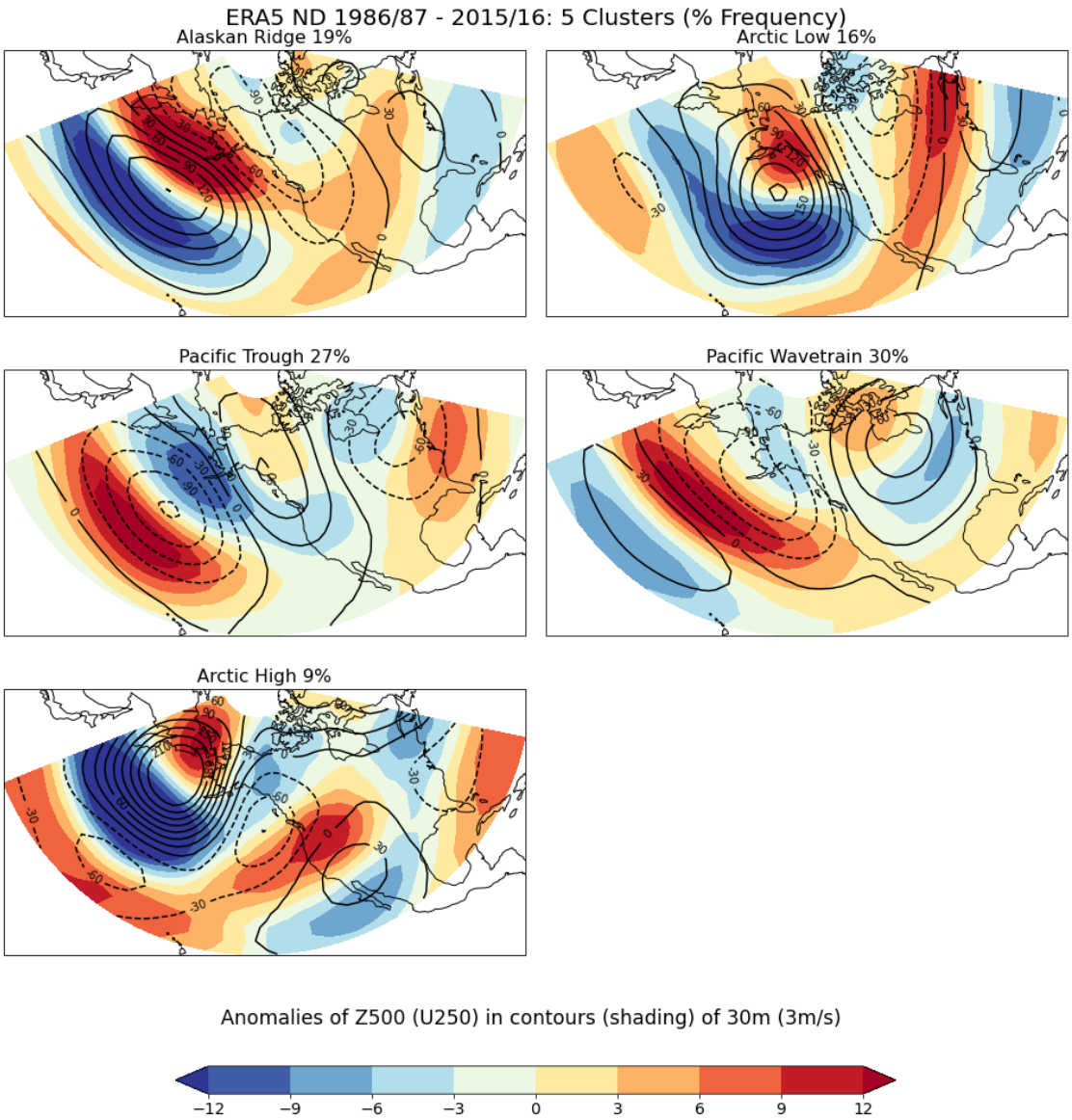

Figure 52 November to December K=5 ERA5 Z500(U250) Cluster Anomaly Composites. Z500 in contours, U250 in shading. Cluster frequency of occurrence given by the percentage. Regime names based on correlation in Z500 structures with NDJFM ERA5 structures.

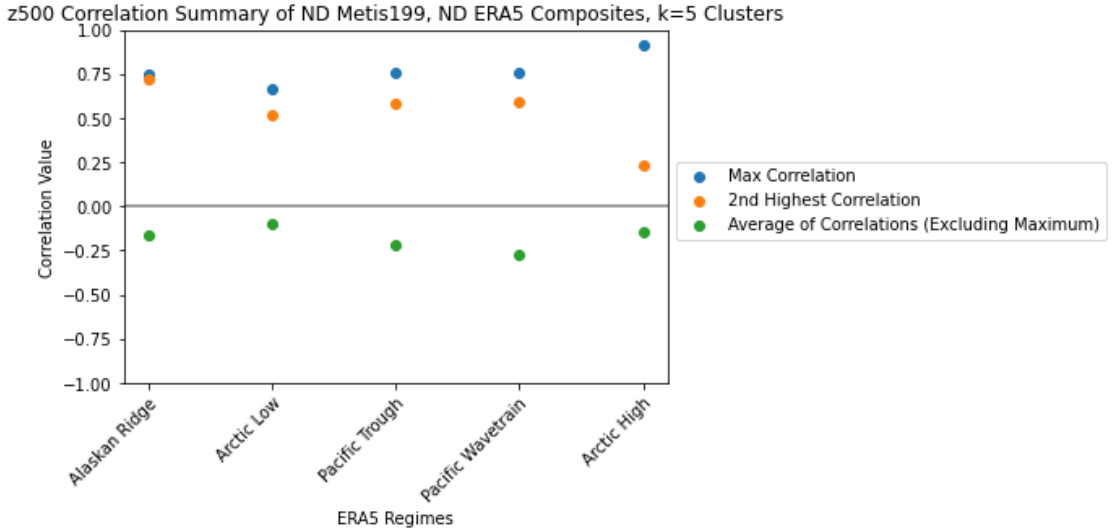

Figure 53 ND Metis199, ERA5 k=5, 1st and 2nd Composite Correlation Summary

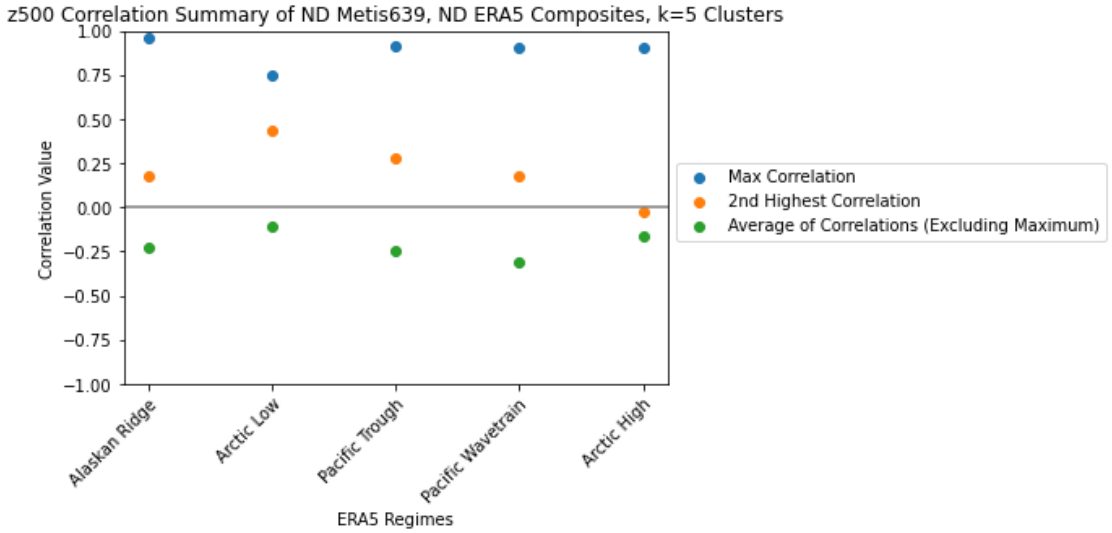

Figure 54 ND Metis639, ERA5 k=5, 1st and 2nd Composite Correlation Summary

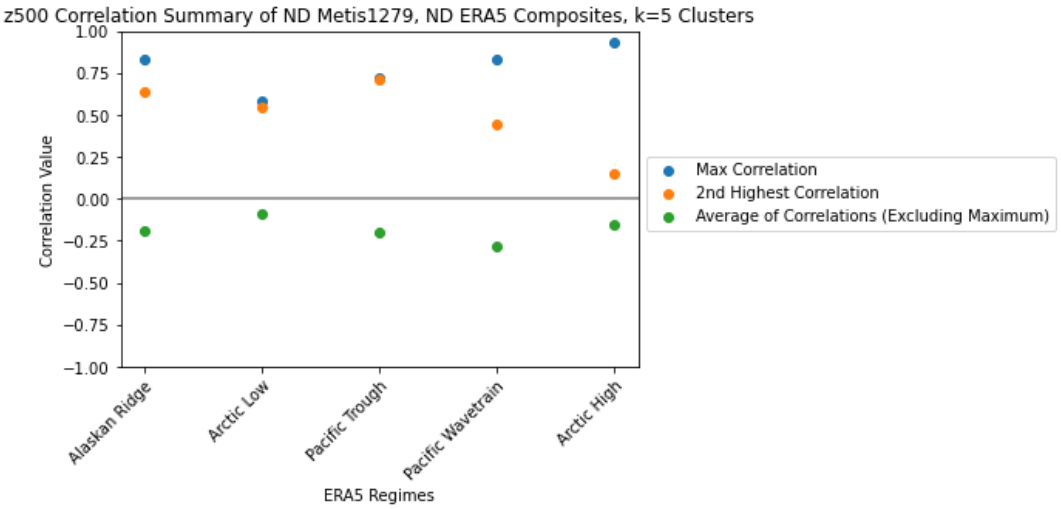

Figure 55 ND Metis639, ERA5 k=5, 1st and 2nd Composite Correlation Summary

Episode Persistence

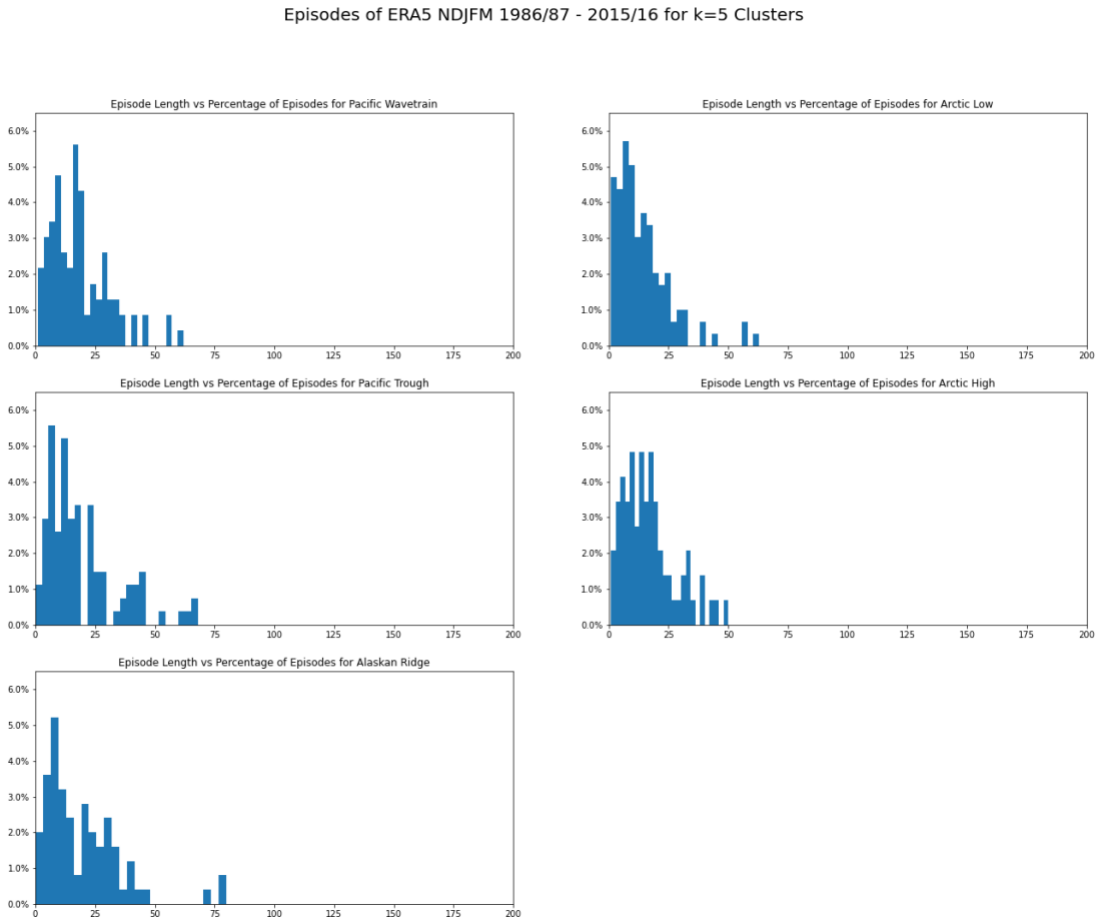

Figure 56 November to March K=5 ERA5 Cluster Persistence Histograms. Length of episode (12 hours) on x-axes, intracluster frequency of episode length occurrence on y-axes. Left to right, top to bottom: Pacific Wavetrain, Arctic Low, Pacific Trough, Arctic High, Alaskan Ridge.

Table 6 November to March, K=5 Kolmogorov-Smirnov P-Values For Null Hypothesis of Same Distribution for ERA5 and Metis Cluster Persistence for Metis199 and Metis639. Null Rejected If P-Value <= Level of Significance.

ERA5 clusters	tco199 NDJFM p-values	tco639 NDJFM p-values
Pacific Wavetrain	.015	.021
Arctic Low	.999	.619
Pacific Trough	.744	.488
Arctic High	.095	.063
Alaskan Ridge	.021	.00

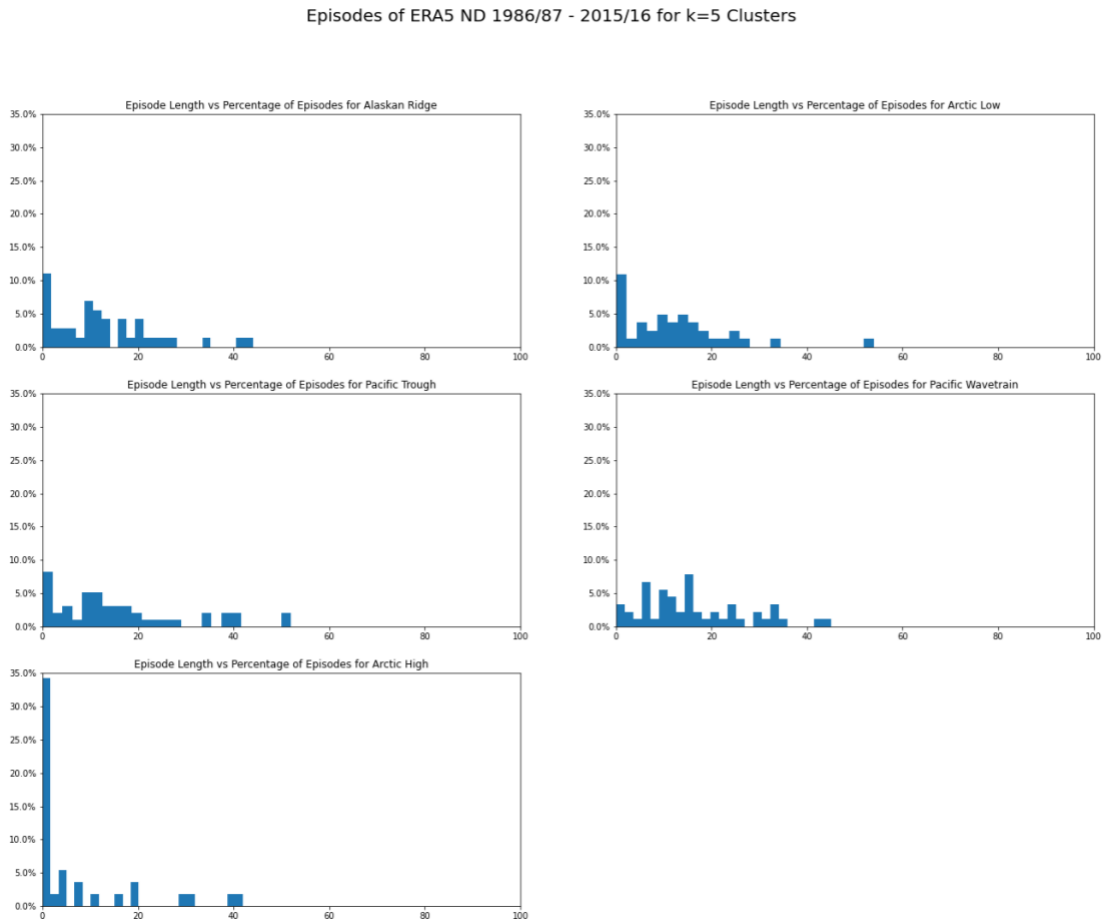

Figure 57 November to December K=5 ERA5 Cluster Persistence Histograms. Length of episode (12 hours) on x-axes, intracluster frequency of episode length occurrence on y-axes. Left to right, top to bottom: Alaskan Ridge, Arctic Low, Pacific Trough, Pacific Wavetrain, Arctic High

Table 7 November to December, K=5 Kolmogorov-Smirnov P-Values For Null Hypothesis of Same Distribution for ERA5 and Metis Cluster Persistence for Metis199 and Metis639. Null Rejected If P-Value <= Level of Significance.

ERA5 regimes	Tco199 ND p-values	Tco639 ND p-values	Tco1279 ND p-values
Alaskan Ridge	AlRidge/ArcLow: .386 PacWav/AlRidge: .628	AlRidge: .968	AlRidge/ArcLow: .466 PacWav/AlRidge: .728
Arctic Low	AlRidge/ArcLow: .71	ArcLow: .467	AlRidge/ArcLow: .796 PacTrough/ArcLow: .832
Pacific Trough	PacWav/PacTrough: .777 PacTrough: .313	PacTrough: .385	PacTrough: .596 PacTrough/ArcLow: .058
Pacific Wavetrain	PacWav/PacTrough: .073 PacWav/AlRidge: .067	PacWav: .06	PacWav/AlRidge: .073
Arctic High	ArcHigh: .006	ArcHigh: .084	ArcHigh: .048

Atmospheric River Composites and Correlations

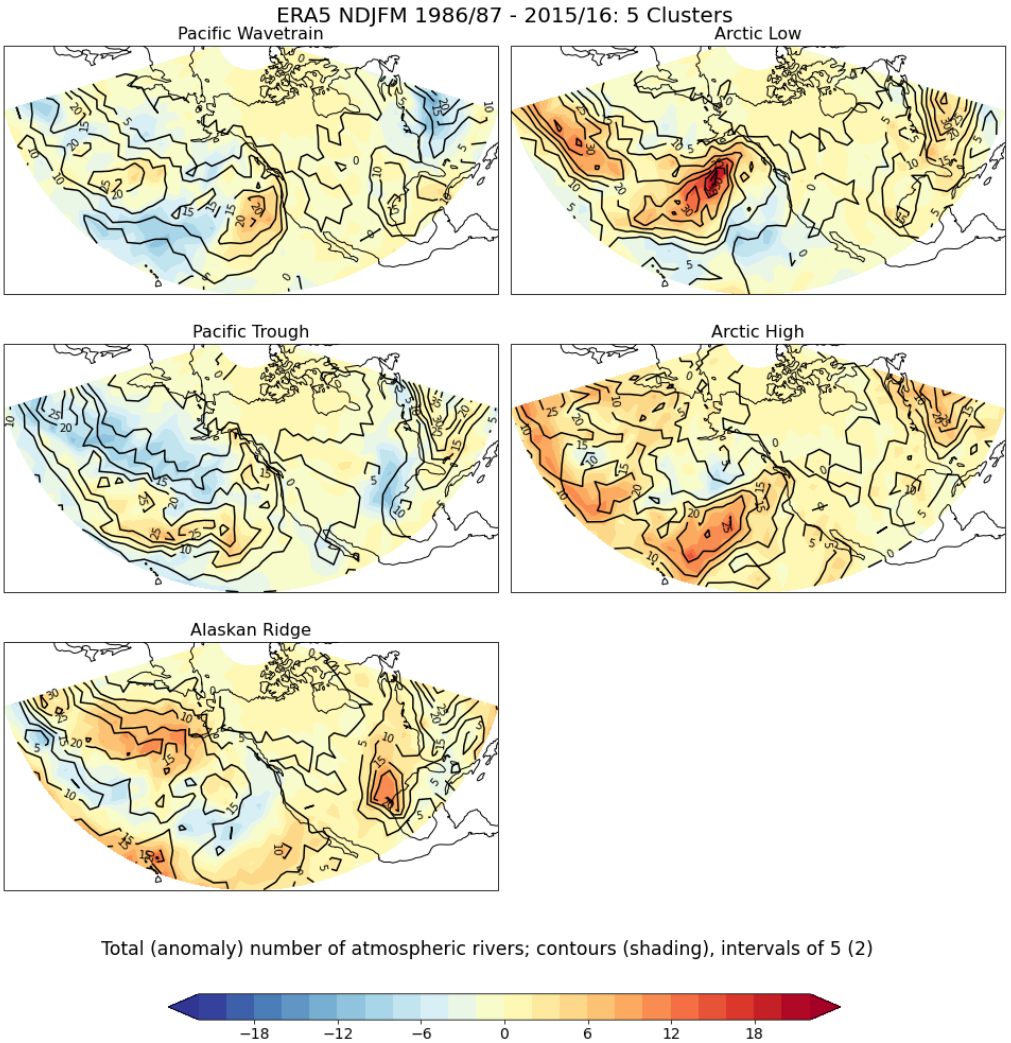

Figure 58 November to March K=5 ERA5 Atmospheric River Regime Composites. Total (anomalous) atmospheric river counts per regime given by contour (shading). Regimes named based on Z500/U250 composites. Positive (negative) anomalies shown in red (blue) shading.

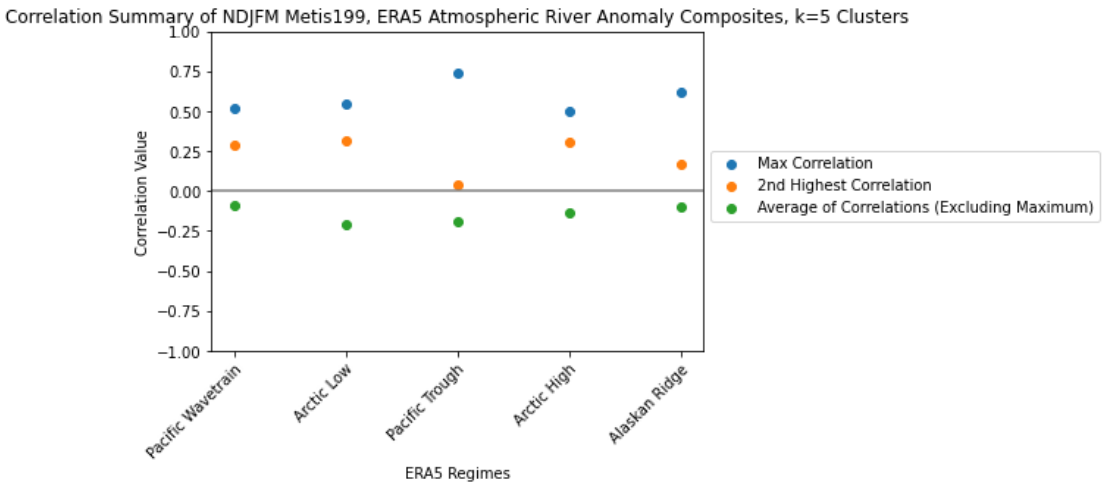

Figure 59 NDJFM 199, ERA5 November to March k=5, 1st and 2nd Atmospheric River Composite Correlation Summary

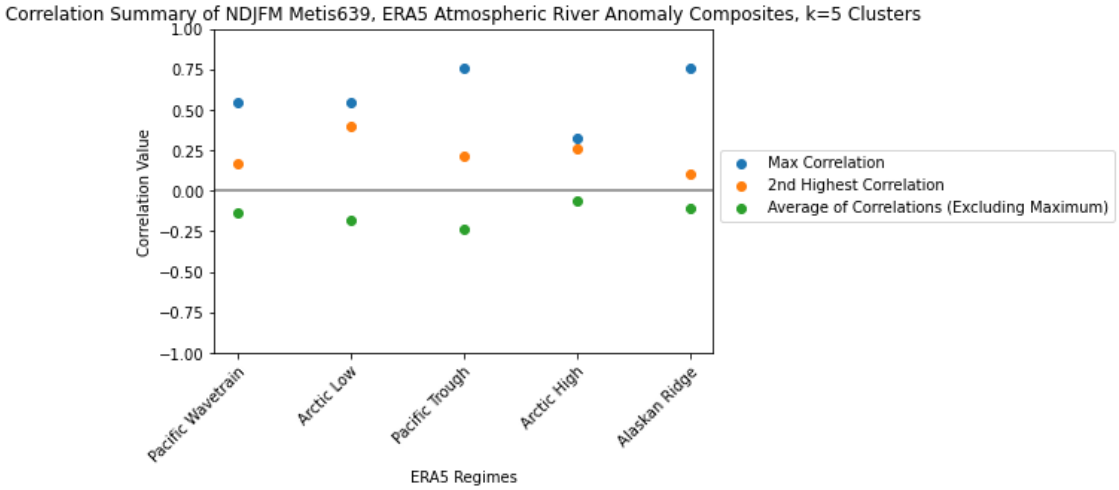

Figure 60 NDJFM 639, ERA5 November to March k=5, 1st and 2nd Atmospheric River Composite Correlation Summary

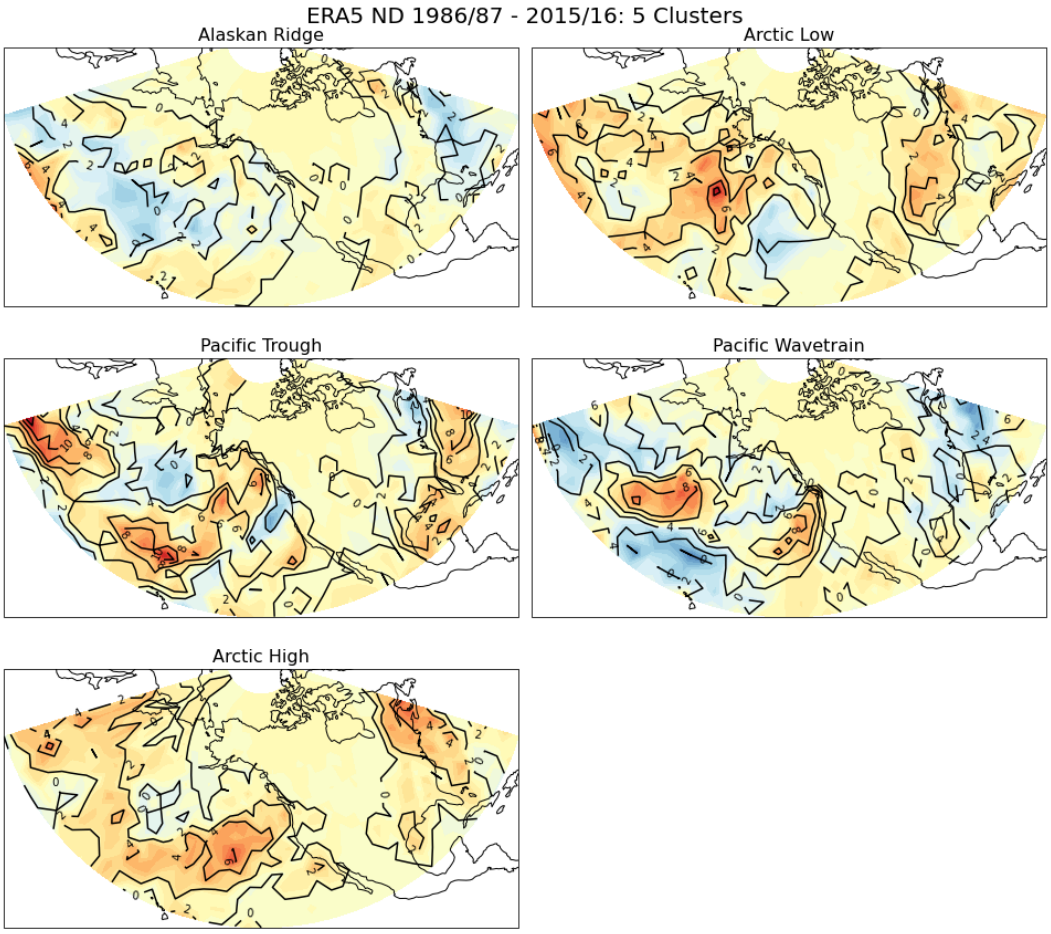

Figure 61 November to December K=5 ERA5 Atmospheric River Regime Composites. Total (anomalous) atmospheric river counts per regime given by contour (shading). Regimes named based on ERA5 NDJFM Z500/U250 composites. Positive (negative) anomalies shown in red (blue) shading.

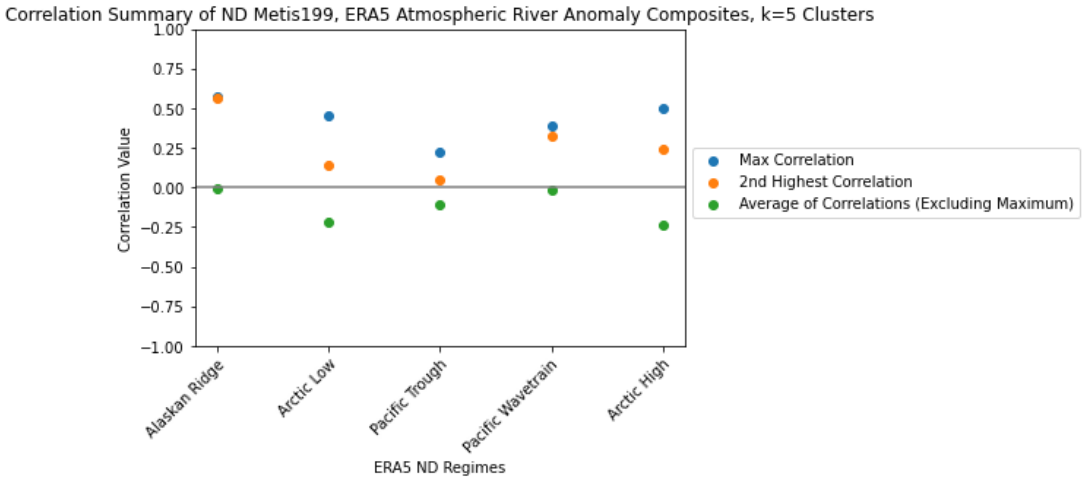

Figure 62 ND 199, ERA5 November to December k=5, 1st and 2nd Atmospheric River Composite Correlation Summary

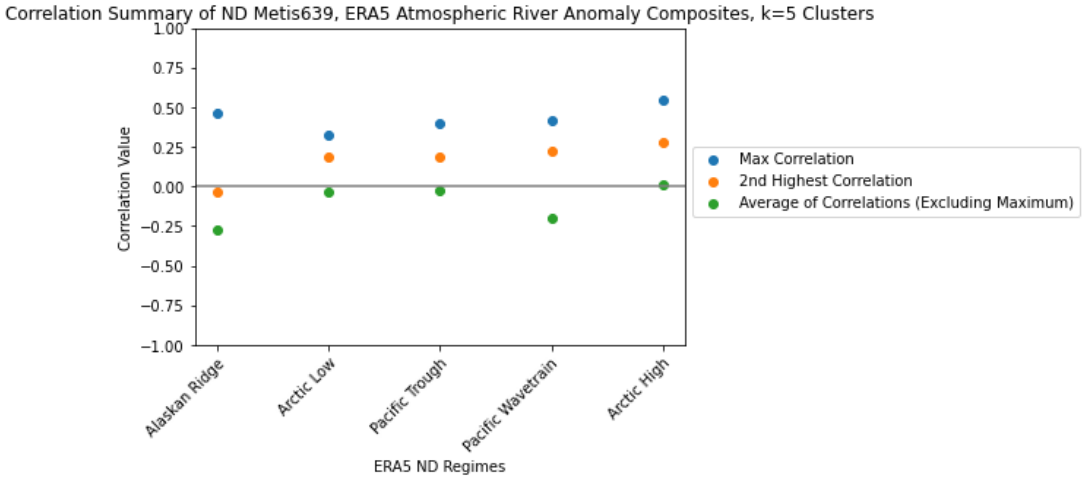

Figure 63 ND 639, ERA5 November to December k=5, 1st and 2nd Atmospheric River Composite Correlation Summary

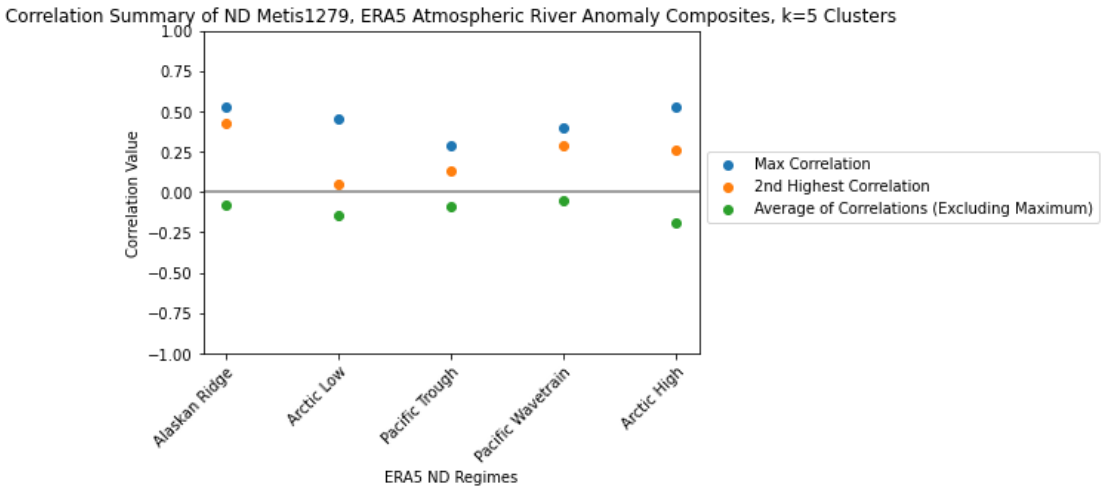

Figure 64 ND 1279, ERA5 November to December k=5, 1st and 2nd Atmospheric River Composite Correlation Summary

REFERENCES

Amini, S., and D.M. Straus, 2019: Control of Storminess over the Pacific and North America by Circulation Regimes. *Climate Dyn.*, **52**, 4749-4770, https://doi.org/10.1007/s00382-018-4409-7.

Dacre, H.F., P.A. Clark, O. Martinez-Alvarado, M.A. Stringer, and D.A. Lavers, 2015: How Do Atmospheric Rivers Form?. *Bull. Amer. Meteor. Soc.*, **96**, 1243-1255, https://doi.org/10.1175/BAMS-D-14-00031.1.

Davini, P., and Coauthors, 2017: Climate SPHINX: evaluating the impact of resolution and stochastic physics parameterisations in the EC-Earth global climate model. *Geosci. Model Dev.*, **10**, 1383-1402, https://doi.org/10.5194/gmd-10-1383-2017.

Dawson, A., T.N. Palmer, and S. Corti, 2012: Simulating regime structures in weather and climate prediction models. *Geophys. Res. Lett.*, **39**, https://doi.org/10.1029/2012GL053284.

Dawson, A. and T.N. Palmer, 2015: Simulating weather regimes: impact of model resolution and stochastic parameterization. *Clim. Dyn.*, **44**, 2177-2193, https://doi.org/10.1007/s00382-014-2238-x.

Dee, D.P.,and co-authors, 2011: The ERA-Interim reanalysis: configuration and performance of the data assimilation system. *Quart. J. Royal Meteor. Soc.*, **137**, 553-597.

DeFlorio, M.J., D.E. Waliser, B. Guan, D.A. Lavers, F.M. Ralph, and F. Vitart, 2018: Global Assessment of Atmospheric River Prediction Skill. *J. Hydrometeor.*, **19**, 409-426, https://doi.org/10.1175/JHM-D-17-0135.1.

Feng, X., B. Huang, G. Tintera, and B. Chen, 2018: An examination of the Northern Hemisphere mid-latitude storm track interannual variability simulated by climate models—sensitivity to model resolution and coupling. *Climate Dyn.*, **52**, 4247-4268, https://doi.org/10.1007/s00382-018-4378-x.

Feng, X., B. Huang, and D.M. Straus, 2019: Seasonal prediction skill and predictability of the Northern Hemisphere storm track variability in Project Minerva. *Climate Dyn.*, **52**, 6427-6440, https://doi.org/10.1007/s00382-018-4520-9.

Hagos, S., L.R. Leung, Q. Yang, C. Zhao, and J. Lu, 2015: Resolution and Dynamical Core Dependence of Atmospheric River Frequency in Global Model Simulations. *J. Climate*, **28**, 2764-2776, https://doi.org/10.1175/JCLI-D-14-00567.1.

Hersbach, H.,and co-authors, 2020: The ERA5 Global Reanalysis. *Quart. J. Royal Meteor. Soc.*, **146**, 1999-2049.

Kinter, J.L., and Coauthors, 2013: Revolutionizing Climate Modeling with Project Athena: A Multi-Institutional, International Collaboration. *Bull. Amer. Meteor. Soc.*, **94**, 231-245, https://doi.org/10.1175/BAMS-D-11-00043.1.

Lavers, D.A., G. Villarini, R.P. Allan, E.F. Wood, and A.J. Wade, 2012: The detection of atmospheric rivers in atmospheric reanalyses and their links to British winter floods and the large-scale climatic circulation. *J. Geophys. Res. Atmos.*, **177**, https://doi.org/10.1029/2012JD018027.

Madec, G., and NEMO-team, 2014: NEMO ocean engine. *Scientific Notes of Climate Modelling Center*, **27**, 357, https://doi.org/10.5281/zenodo.1464816.

Payne, A.E., and G. Magnusdottir, 2014: Dynamics of Landfalling Atmospheric Rivers over the North Pacific in 30 Years of MERRA Reanalysis. *J. Climate*, **27**, 7133-7150, https://doi.org/10.1175/JCLI-D-14-00034.1.

Polichtchouk and co-authors, 2019: Control on Stratospheric Temperature on IFS: Resolution and Vertical Advection. *ECMWF Technical Memorandum*, **847**.

Ralph, F.M., P.J. Neiman, and G.A. Wick, 2004: Satellite and CALJET Aircraft Observations of Atmospheric Rivers over the Eastern North Pacific Ocean during the Winter of 1997/98. *Mon. Wea. Rev.*, **132**, 25, https://doi.org/10.1175/1520-0493(2004)132<1721:SACAOO>2.0.CO;2.

Rutz, J.J., W.J. Steenburgh, and F.M. Ralph, 2014: Climatological Characteristics of Atmospheric Rivers and Their Inland Penetration over the Western United States. *Mon. Wea. Rev.*, **142**, 905-921, https://doi.org/10.1175/MWR-D-13-00168.1.

Straus, D.M., S. Corti, and F. Molteni, 2007: Circulation Regimes: Chaotic Variability versus SST-Forced Predictability. *J. Climate*, **20**, 2251-2272, https://doi.org/10.1175/JCLI4070.1.

Straus, D.M., S. Corti, and F. Molteni: The Link between Weather and the Large Scale Circulation, in *Nonlinear and Stochastic Climate Dynamics*, Cambridge University Press, 2017, ISBN 9781107118140. Ed. C. Franzke.

Strommen, K., I. Mavilia, S. Corti, M. Matsueda, P. Davini, J. von Hardenburg, P.-L. Vidale, and R. Mizuta, 2019: The Sensitivity of Euro-Atlantic Regimes to Model Horizontal Resolution. *Geophys. Res. Lett.*, **46**, 7810-7818, https://doi.org/10.1029/2019GL082843.

Swenson, E., J. Lu, and D.M. Straus, 2018: Resolution Dependence and Rossby Wave Modulation of Atmospheric Rivers in an Aquaplanet Model. *J. Geophy. Res. Atmos.*, **123**, 6297-6311, https://doi.org/10.1029/2017JD027899.

Swenson, E.T., and C. Stan, 2019: Sensitivity of Atmospheric Rivers to Damping of Midlatitude Subseasonal Variability. *J. Geophys. Res. Atmos.*, **124**, 9935-9947, https://doi.org/10.1029/2018JD029934.

Vitart, F., and co-authors, 2019. Extended-Range Prediction. European Centre for Medium-Range Weather Forecasts, Technical Memo 854.

Wise, E.K., M.L. Wrzesien, M.P. Dannenberg, and D.L. McGinnis, 2015: Cool-Season Precipitation Patterns Associated with Teleconnection Interactions in the United States. *J. Appl. Meteor. Climatol.*, **54**, 494-505, https://doi.org/10.1175/JAMC-D-14-0040.1.